Dynamically operated, solar-driven Reverse Osmosis for battery-free drinking water supply

Dynamisch betriebene, solarbasierte Umkehrosmose zur Batteriefreien Trinkwasserversorgung

Der Fakultät für Maschinenbau und Schiffstechnik
der Universität Rostock
Lehrstuhls für Technische Thermodynamik

zur

Erlangung des Doktorgrades

D O K T O R - I N G E N I E U R

vorgelegt von

Alireza Derakhshan

Aus Shahriar

Als Dissertation genehmigt

von der Fakultät für Maschinenbau und Schiffstechnik

der Universität Rostock

Tag der mündlichen Prüfung: 08.12.2023

Vorsitzender des Promotionsorgans: Prof. Dr.-Ing. Sascha Kosleck

Gutachter:

Prof. Dr.-Ing. habil. Karsten Müller - Lehrstuhl für Technische Thermodynamik

Prof. Dr.-Ing. habil. Jens Tränckner - Agrar- und Umweltwissenschaftliche Fakultät

Abstract

Batteries account for a significant share of the lifecycle cost of solar-based water desalination (PVRO) systems. Recently, battery-free PVRO has been developed and widely used, as it requires less investment (CAPEX) and running costs (OPEX). However, removing batteries leads to high fluctuations and uncontrolled shutdowns during the operation. Because the solar energy curve is inherently intermittent, and sharp energy reductions occur frequently.

A novel technology, Multifunctional driver (MFD), is developed in this thesis to address this drawback of the conventional battery-free solar reverse osmosis systems.

The entire system is simulated by MATLAB/Simulink®, and the outcomes are compared with conventional simulation software. To validate the software, an industrial-scale pilot project (250 lit/h) is developed and installed in Cape Coast, Ghana. Cloud-based remote monitoring is designed to monitor the pilot project between October 2020 and October 2022. Furthermore, an accelerating test bench is designed to investigate the long-term performance of this technology under dynamic operating conditions. The test bench is powered by a harsh and highly fluctuating solar curve. Surrogate water, based on the borehole water analysis of the pilot project, is used in a closed loop as the feed water of the test bench system.

The performance of both systems, i.e., the pilot project under real conditions and the test bench with the simulated condition, is monitored. In addition, a complete midpoint Life Cycle Analysis (LCA) has been done using GaBi software. The results are compared with a conventional PVRO system.

Particularly, as the main challenge of PVRO systems, the effect of the developed technology on fouling and scaling is studied. A combination of SEM and EDX of the membrane's surface, cross-section, and permeate side are investigated to map the scaling formation.

Zusammenfassung

Batterien verzeichnen einen erheblichen Teil der Lebenszykluskosten von solarbasierten Wasserentsalzungsanlagen (PVRO). Kürzlich wurden batterielose PVRO entwickelt und weitläufig eingesetzt, da sie niedrigere Investitions- (CAPEX) und Betriebskosten (OPEX) haben. Das Entfernen der Batterien führt jedoch zu starken Schwankungen und unkontrollierten Abschaltungen während des Betriebs. Denn die Einstrahlungsstärke ist häufig intermittierend, und es kommt zu starken Leistungsabfällen.

In dieser Arbeit wird eine neuartige Technologie, der Multifunctional Driver (MFD), entwickelt, um diesen Nachteil der herkömmlichen batterielosen solaren Umkehrosmosesysteme zu beheben.

Das gesamte System wird mit MATLAB/Simulink® simuliert, und die Ergebnisse werden mit konventioneller Simulationssoftware verglichen. Zur Validierung der Software wird ein Pilotprojekt im industriellen Maßstab (250 l/h) entwickelt und in Cape Coast, Ghana, installiert. Eine cloudbasierte Fernüberwachung soll das Pilotprojekt zwischen Oktober 2020 und Oktober 2022 überwachen. Darüber hinaus ist ein weiterer Labortest mit beschleunigten Betriebsbedingungen vorgesehen, um die langfristige Leistung dieser Technologie unter dynamischen Betriebsbedingungen zu untersuchen. Der Versuchsstand wird durch eine harsche und stark schwankende Solarkurve betrieben. Das Eingangswasser, das auf der Brunnenwasseranalyse des Pilotprojekts eingestellt wird, wird in einem geschlossenen Kreislauf für das Prüfstandssystem verwendet.

Die Leistung beider Systeme, d. h. des Pilotprojekts unter realen Bedingungen und des Versuchsstands unter simulierten Konditionen, wird überwacht. Darüber hinaus wurde mit der GaBi-Software eine vollständige mittlere Lebenszyklusanalyse (LCA) durchgeführt. Die Ergebnisse werden mit denen eines herkömmlichen PVRO-Systems verglichen.

Insbesondere werden die Auswirkungen der entwickelten Technologie auf Fouling und Scaling untersucht, da dies die größte Herausforderung bei PVRO-Systemen darstellt. Eine Kombination aus REM und EDX der Membranoberfläche, des Querschnitts und der Permeatseite wird untersucht, um die Scaling-Bildung nachzuvollziehen.

Curriculum Vitae

PERSONAL DATA

Nationality: German
Date of birth: 06.04.1983
Marital status: Married

WORK EXPERIENCE:

06.2019– Present **Grino Water Solutions GmbH – Co-founder and CEO**
Off-grid battery-free solar water purification system (https://grinowater.com)

- Developing a commercial product from an R&D project – entire product lifecycle
- Manging solar-based projects in several African countries
- Maintain project trackers e.g Project plan, Risk tracker, budget tracker etc.
- Liaising with both current and potential clients to develop existing and new products/business models
- Preparing documents for RFQs and RFPs
- Project documentation and presenting the results
- Brand Building, Market entrance strategy and Business development
- Cultivate relationships with key players, clients, and strategic partners
- Hired, trained, leading, and motivating the team and employee engagement

06.2017-02.2020 **Institute of Separation Science and Technology (FAU Erlangen)**
Scientific Staff (solar-based control system)

- Designing, prototyping, testing, and validating the product and submitting patent
- Commercialization of the R&D project and founding a university spin-off
- Simulation (and validation) of a novel water purification (MATLAB/Simulink)
- Life cycle assessment (LCA) based on ISO 14040
- Vendor Selection, Resource Planning and Procurement management
- Coaching & Mentoring master and bachelor students
- Analysis and presentation of achievements

10.2013 – 05.2017 **Bavarian Centre for Applied Energy Research (ZAE Bayern)**
Project Engineer – Solar Building

- planning, simulation and installation of a solar building (MATLAB, GAMS)
- Validation of the project results
- Vendor Selection and Process Mapping for Demonstration system
- Resource Planning, Management reports, Budgetary Control
- Analysis and presentation of achievements

02.2014 – 10.2014 **Friedrich Alexander University,** Erlangen | chair of Electrical Energy Systems | *Simulation Engineer – Part time*

- Simulation of wind turbine, Generator, converter, and control system
- Analysis and presentation of achievements

v

EDUCATION:

08.2006 – 06.2009   **M.Sc. Energy Engineering** | Azad University - (Science & Research Branch)
Tehran, Iran – Energy engineering.

Thesis: Role of power plants (wind farms) on grid frequency controlling and logic analysis of energy management (granted by: IFCO (Iran Fuel Conservation Organization))

08.2001 – 08.2005   **B.Sc. Mechanical engineering** Azad University
Tabriz, Iran - Mechanical Engineering.

PERSONAL SKILLS:

Computer   Matlab/Simulink
Basic, C++
AutoCAD
Microsoft Office
Windows

Language   German (B2)
English (C1)
Persian (Native)

Publications and Presentations:

2019 EU Patent Application: Alireza Derakhshan, Sebastian Hörlin - DPMA application ID: 102019129348 - **Anlage zur Aufbereitung von Wasser und Verfahren dazu**

2021 **OFF-GRID Expo + Conference** – Oral Presentation and Panellist: Integrating solar water purification into existing Mini-Grids to increase the energy efficiency and profitability

2021 **WACEE (West African Clean Energy & Environment Trade Fair & Conference)** – Oral Presentation and Panellist: Novel battery-free water desalination system for remote areas

2021 **European Technology Chamber** – Speaker and Panellist: Energy Council Webinar ´Innovations for Energy and Efficient Cooling (SDG 7 & 9)

2016 **Direct use of photovoltaic energy to supply the solar cooling system of a research building.**

1st conference: Integration of Sustainable Energy Conference iSEneC 2016 – Nuremberg, Germany

2011 **Optimization of position of engine room's air inlet vents in high-speed crafts based on simulation.**

2nd conference: National Industrial ventilation and Hygiene - Sharif University of technology, Iran

2010 **Analysis of high-speed craft ventilation system based on standard relations and numerical solution.**

1st conference: National Industrial ventilation and Hygiene - Sharif University of technology, Iran

2009 Predictive Control of Wind Energy Conversion.
International Conference: Electrical Energy and Industrial Electronic Systems EEIES 2009, 7-8 December 2009, Penang, Malaysia

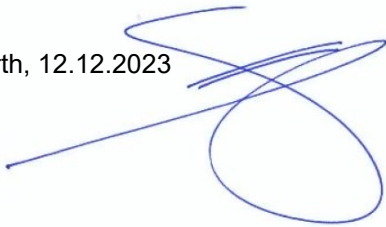**2009 Optimal Distance Protection with a Modified Particle Swarm Optimization**.
International Conference: Electrical Energy and Industrial Electronic Systems EEIES 2009, 7-8 December 2009, Penang, Malaysia

2009 New PSS for Improving Dynamic Performance of Pump-Storage Power Plants
International Conference: Electrical Energy and Industrial Electronic Systems EEIES 2009, 7-8 December 2009, Penang, Malaysia

2009 Study of Asynchronous Wind Turbine Effects on Weak Grid by Using Small Signal Modeling
International Conference: Electrical Energy and Industrial Electronic Systems EEIES 2009, 7-8 December 2009, Penang, Malaysia

Fürth, 12.12.2023

Acknowledgments:

I would like to express my appreciation to my wife, Bahareh, and my parents for their endless patience, unwavering love, and for being with me all my life, especially during this challenging PhD time.

I also enjoyed spending time in Ghana, installing and testing the system in real condition. It has always impressed me as very amazing how motivated, hospitable and supportive the people in Africa are.

Table of Contents

Chapter 1

Fundamentals and characterization technique

1. Theoretical background

1.1. Introduction

Energy and water are the most pressing issues in the world, which directly influence the health and life quality of the community[1]. Although 70 percent of the earth is covered by water, 1.2 billion people worldwide, almost one-sixth of the world's population, do not have access to adequate clean water[2]. Furthermore, almost 2.7 billion people live in water-stressed areas, where at least one month per year, no access to safe and clean water resources is available. Because surface and even underground water resources can be contaminated with harmful suspended and dissolved particles or dangerous pollutants from anthropogenic and agricultural activities. Therefore, natural waters might also need to be treated[3]. Today, waterborne diseases, such as cholera and typhoid fever[4], cause 6% of the deaths in remote and low-income areas[5]. Collecting water from an improved water source requires 207 million people to travel more than 30 minutes roundtrip. This lost time can be used to generate income, enhance education, and spend time with the family.

Even in developed countries, supplying water is problematic. The exponential economic growth of various developed and developing countries such as the U.S., China, India, and UAE has driven concerns regarding water depletion and scarcity, threatening agriculture, industry, and human lives. Even in some areas, water scarcity leads to multidisciplinary political conflicts, especially when few countries share a common water resource, like a river or a lake. Water reuse and desalination are widely used in arid countries to provide drinking water[6]. Seawater is freely available and exists close to coastal lands. Hence, desalination of seawater can be an appealing and reasonable option as an alternative potable water supply[7]. Fig. 1 shows how desalination and water reuse can be applied to provide water in a sustainable approach for households, industry, and agriculture. However, this technology has two main drawbacks; desalination is a high-priced and energy-intensive process. Continuous efforts have been performed during the last decade to enhance desalination technologies' economic and environmental impact[8]. The main goal is to reduce the produced water cost by increasing energy efficiency and reducing the system complexity.
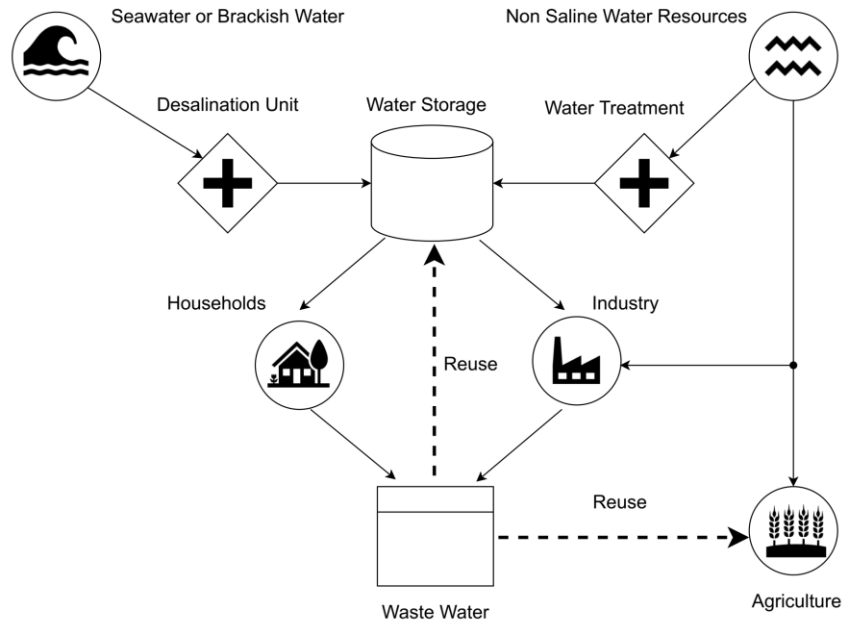
Figure 1 combination of desalination plants and water reuse to increase water purification efficiency[9]

Fig. 2 shows a typical seawater desalination system's investment cost (CAPEX) and operating costs (OPEX). Energy expenditure contributes to more than 25% of the lifecycle cost. Therefore, powering desalination plants with renewable energy resources (RE) can remarkably reduce OPEX. In addition, integrating RE into the desalination system improves environmental impact and makes it suitable for remote areas with poor infrastructures[10]. Currently, RE-powered desalination plants (RED) have a meager market share, i.e., about 1% of the exciting plants[11]. The main reason is the high investment cost of RE systems, which is continuously decreasing[12] and will lead to more future RED applications[13].
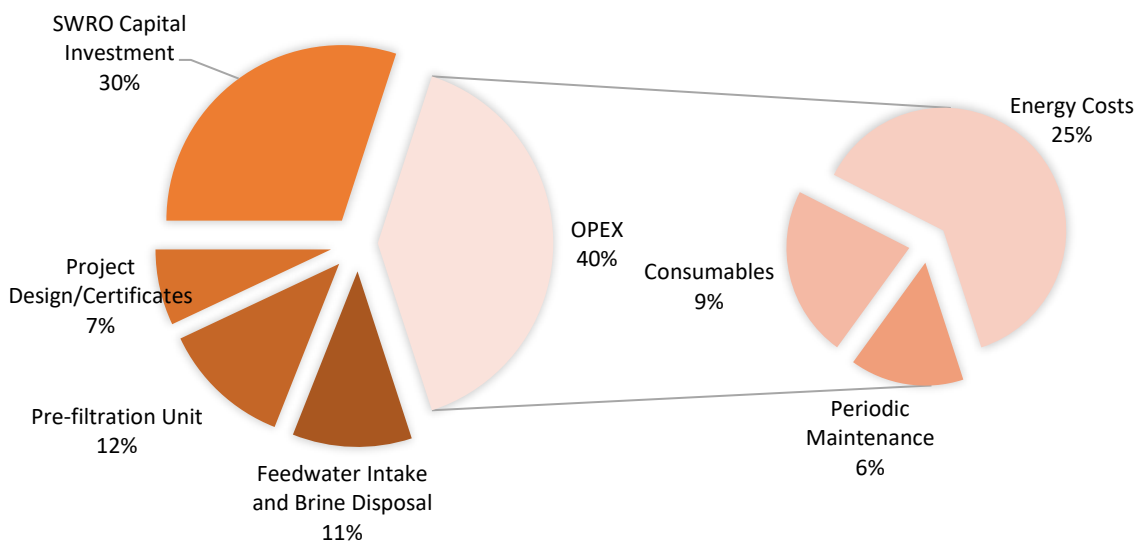
Figure 2 CAPEX and OPEX of a conventional seawater desalination system based on reverse osmosis technology[14]

The demand for unconventional water resources has increased in recent years, propelled by increasingly limited access to conventional freshwater resources. Furthermore, in recent years, desalination material has been remarkably enhanced to make the system more affordable and increase its performance, which had a notable role in increasing desalination applications[15,16]. In 2019, more than 15000 desalination plants were operating worldwide, producing about 95 million m^3/day. Desalination of seawater and brackish water will still play a significant role in the future. Although the period between 2008 and 2014 has been turbulent, with the financial crisis and the crash in oil prices affecting budgets in the Arab world, the market has since been on the road to recovery. The continuing industrialisation and urbanisation in India and China and the expansion of desalination applications in the United States to secure water supplies will continue to propel the market in the world. However, the Middle East still contributes as the most significant market player, and more than 47% of the existing desalination plants are installed in this region[17]. Desalination systems can be divided into two categories based on technology.

1.2. Membrane-based water purification technologies

The semipermeable membrane is the core part, which can separate and remove specific ions. Based on the driving force, there are different membrane-based water purification technologies; hydraulic pressure, electrical potential difference, and osmotic pressure, i.e., reverse osmosis (RO), electrodialysis (ED), and forward osmosis (FO) use each of the mentioned driving forces respectively. RO is the most common technology and has the most outstanding share in the water purification market, with about 70%. Electrodialysis is limited to brackish water application (feed water salinity below 5000 ppm). Using ED for seawater is not economically viable. Direct osmosis has become more attractive lately, especially in high desalination capacities. However, commercial applications are still limited[18]. The most important methods and the market contributions are shown in Fig. 3. Till 1980, thermal desalination technology was the most common water purification method due to the low energy price. However, membrane-based methods, particularly reverse osmosis technology, are the most dominant option currently.

4
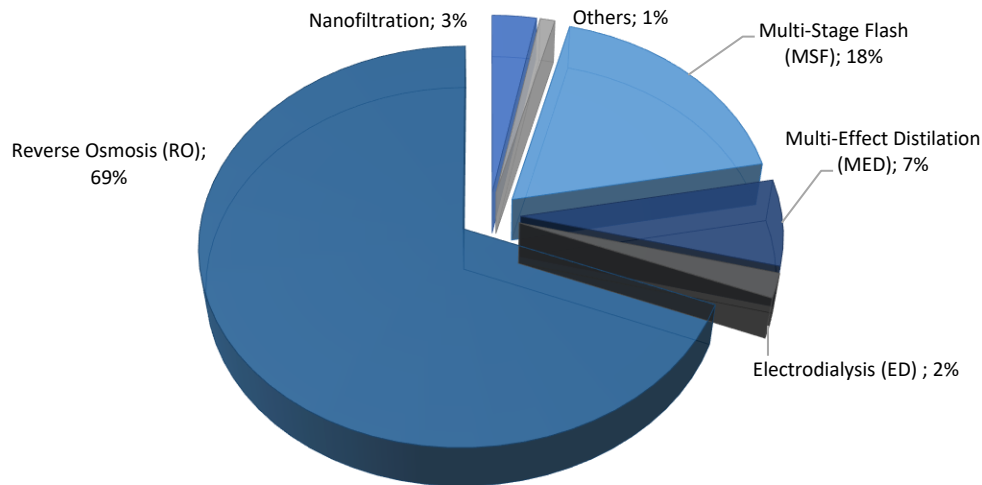
Figure 3 contributions of different desalination methods in water purification market [19]

1.2.1. Reverse Osmosis (RO)

RO is a well-established desalination technology that utilises pumping pressure and a semipermeable membrane to separate saline feedwater into a high-quality permeate stream and a concentrated "brine" stream[20]. Following the development of the RO membrane in 1959, it was later commercialised in the 1970s[21] and has achieved remarkable success in becoming the dominant global desalination technology due mainly to its lower capital costs, lower energy demand, robust operation, wide range of input water, and reduced footprint[22]. RO can remove dissolved salts like NaCl, biological components, and other harmful particles like nitrates, mercury, arsenic, lead, pesticides, and fluorides. In addition, RO technology is used in wastewater treatment plants as well.

In RO systems, high-pressure water passes through the membranes to overcome the osmotic pressure. Osmotic pressure occurs between two solutions with different concentrations. Therefore, the osmotic pressure depends on the feedwater's Total Dissolved Solids (TDS). Osmosis is a natural phenomenon in which the water from the solution with a lower concentration will flow to the solution with a higher concentration until both solutions reach a balanced status. In the RO technology, an external driving force will be applied to reverse this phenomenon, i.e., feedwater with higher TDS will flow to the lower concentration side of the membrane. The driving force should be higher than the osmotic pressure plus all other pressure losses in the system to overcome the osmotic phenomenon. Fig. 4 demonstrates these two processes.

Initial State

Semi-Permeable membrane

Flow Direction   Flow Direction
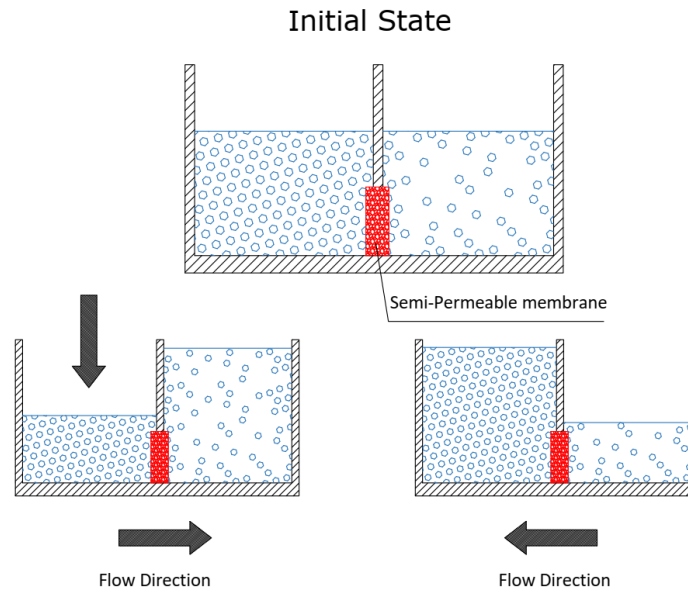
Figure 4 Schematics of osmosis and reverse osmosis process, right: natural water flow direction (osmosis phenomena), left: reverse osmosis direction, which needs an external driving force [23].

RO removes, on average, 99.7% of total dissolved solids (TDS), giving it a wide range of applications for brackish water, seawater, and ultrapure industrial applications. The high-quality RO permeate has a wide range of industrial uses, such as feedwater treatment for boilers or pre-treatment for ultrapure water production in hydrogen plants. Reclaimed municipal wastewater is also treated with RO to various standards for potable and non-potable applications.

RO membranes have the finest membrane pores compared to the other technologies. Therefore, RO can remove any particles even in the ionic range, i.e., RO can filter suspended solids, protozoa, bacteria, viruses, and harmful substances from the feedwater. Hence, each range of membrane layers prevents a specific kind of particles. Fig. 5 provides a detailed comparison between the membrane technologies based on the pore sizes and filtration possibilities.

Electrical energy consumption is the most considerable expense in a RO plant. Research and developments have focused heavily on increasing the energy efficiency of this process since it began to dominate the global market in the 1990s. Ultimately, energy savings translate into monetary savings that lower the price of desalinated water and make it a more lucrative solution to water scarcity and industrialisation, particularly in regions where desalination is one of many competing solutions or where electricity is expensive to produce.

	Ionic Range	Molecular Range	Macro Molecular Range	Micro Patride Range	Micro Patride Range
Water Treatment Process	Reverse Osmosi	Ultrafiltration		Patride Filtration	
	Nanofiltration	Microfiltration			
	Ino Exchange				
Size of the Particles to be trated	Metal Ions	Viruses		Human Hair	
	Endotoxins/Pyrogens	Algae			
	Dissolved Salts	Colloids			
	Insecticides				
	Milk Protiens				
	Antibitics	Bacteria			
Microns (Log Scales)	0.0001 0.001 0.01	0.1	1	10	100
Angstrom Units (Log Scales)	1 10 100	1000	1E+04	1E+05	1E+06
Approx. Molecular Weight (Daltons)	100 1000 20000 / 200 1000	500000 / 100000	5000000 / 1000000		

Figure 5 filtration size and application of different membrane-based technologies (Aqua Clear, 2009)

Other stages also contribute to energy use, including pumping for intakes and outfalls, brine management, pre-filtration unit, and permeate distribution. However, RO process generally accounts for 60% of the whole power consumption[24]. A typical breakdown is shown in fig. 6. Several breakthroughs have allowed for a drastic improvement in the specific power consumption (SEC) of the RO process, from enhancements in membrane permeability, anti-fouling, scaling, and the large-scale adoption of efficient energy recovery devices, among others. These resulted in a drop in power consumption of about half from 7 kWh/m³ in the early 1990s to 3.2 (3.3) in 2015–2016. For seawater plants, the values are slightly higher, with averages (medians) dropping from 4.8 (4.2) kWh/m³ to 4.3 (3.8) over the same timeframe, with the largest and most advanced SWROs currently reaching levels of around 3 kWh/m³.
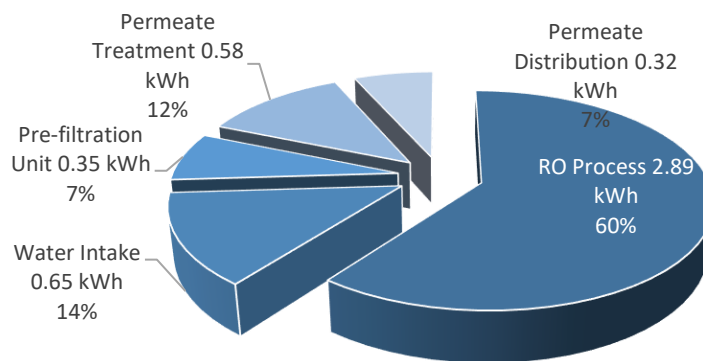
Figure 6. Energy consumption breakdown in a typical seawater RO system. The total energy consumption is, on average, about 4.3 kWh/m³.

Regarding membrane technology, there are mainly two common types of membranes for RO applications: Polymeric Membranes and Ceramic Membranes. The latter is a new technology and is still in the development phase. Therefore, the market is dominated by polymeric membranes, especially Cellulose Acetate-based (CA) membranes and Thin-Film Composite (TFC) Membranes, which were developed in the 1955 and 1970s, respectively[25,26]. Regardless of the membrane technology, an exact pre-filtration system is necessary for RO systems, mainly to increase the membrane's lifespan and improve water production efficiency[27]. Fouling and biofilm formation are the two main problems in RO technology, especially for seawater systems, as the feedwater contains different foulants. Pre-treatment can reduce the scaling potential by aggregating organic matter, adjusting the pH, and reducing the charged colloids[28,29]. As shown in fig. 7, the pre-treatment process typically involves several chemical and physical steps depending on the feedwater chemistry.
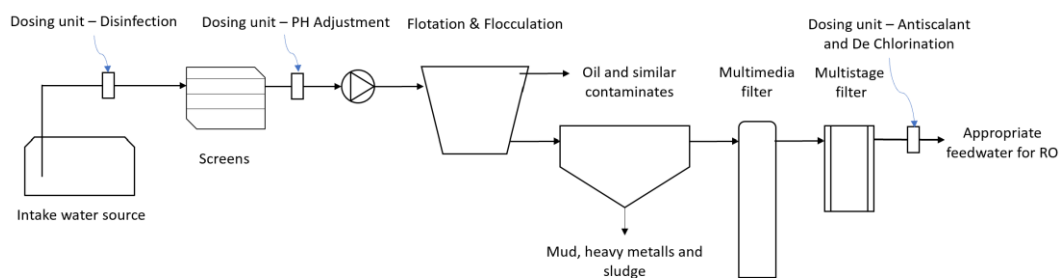
Figure 7. a complete pre-treatment is schematically depicted in this figure[30].

1.2.2. Nanofiltration

Nanofiltration is limited to non-salty water purification applications like water softening or removing by-products created during water decontamination. Besides, non-soluble organic matter, hazardous pollutants (for instance nitrate, fluoride, and arsenic)[31], and some substances that are effective in odour and water hardness formation can be eliminated (see fig. 5). The other difference between nanofiltration and RO is the feed stream on the membranes. As illustrated in fig. 8, dead-end membranes are used for nanofiltration, while crossflow membranes should be applied in RO. The main advantage is that the whole feedwater will pass through the membrane and be used as treated water, while in RO, at least 30% of the feedwater will leave the pressure vessel as brine.
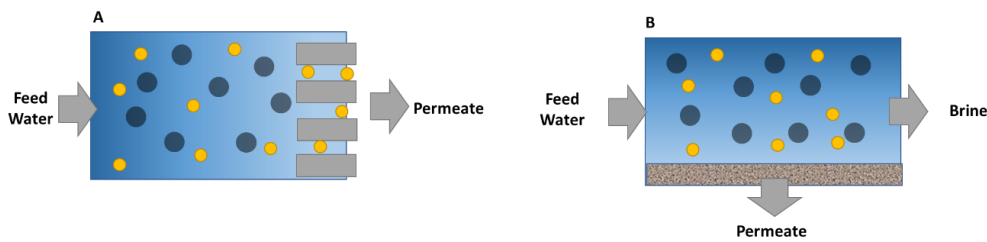
Figure 8 schematic view of (A) dead-end membrane feed stream (B) cross-flow mode membrane[32].

1.2.3. Electrodialysis/reverse electrodialysis

Electrodialysis (ED) is another membrane-based electro-driven technology invented before RO in the 1950s. This technology is based on the ion-selective membrane, which can separate and remove charged particles. ED is based on an electrochemical phenomenon that uses ion exchange membranes (IEMs) to separate specific cations and anions. Specific DC voltage will be applied to the electrodes, and the raw water passes through the cell and forms an electrical flow between the negative and positive electrodes. Reverse electrodialysis (EDR) is similar to ED, with the exception that the polarity of the electrodes is frequently reversed, allowing for flushing of the concentrated brine. This method decreases the frequency of membrane replacements and cleanings and protects membranes from scaling and fouling. EDR processes are applied mainly to brackish water, tertiary wastewater production and specific industrial applications such as the mining, pharmaceuticals, and food & beverage industries.

Technically, ED can be used for seawater desalination, but it is not an economical method due to the high energy demand. Nonetheless, ED is a reliable alternative for brackish water desalination as it does not need high pressure. Seawater is a complex solution including different salts, foulants, and particles, which can significantly change the performance of the IEMs. Pre-treatment can be helpful in reducing these drawbacks. However, a pre-filtration system, which can remove multivalent ions from seawater to prepare it for ED, also has high OPEX. The other solution is to use different IEMs, with different specifications, current densities, and applied voltages to remove multivalent ions[33].

1.3. Thermal-driven methods

Primarily for the desalination of seawater or evaporative concentration and crystallisation of brine, thermal technologies have a long history in the desalination market in North Africa, the Caribbean, and particularly the Middle East[34]. However, advances in RO have severely

undercut the market for new thermal capacity. Leading thermal-driven technologies involves multi-stage flash (MSF), multi-effect distillation (MED), and vapor compression distillation (VC)[35]. Regarding energy source, thermal technologies use both electrical and thermal energy. MSF and MED use electricity for pumping and circulation and thermal energy, i.e., low-pressure steam, for heating the feedwater and creating the distilled permeate. While vapour compression processes only utilise electrical power. In general, the lifetime of a thermal desalination plant is between 10 and 15 years[36].

RO's lower total energy demand has been the most instigating driver in its adoption over MSF and MED processes[37]. Table 1 summarises and compares the technical specifications of MSF, MED, and seawater RO (SWRO).

1.3.1. Multi-stage flash (MSF)

MSF is the most common thermal desalination, with about 80% of the market share. In MSF, thermal energy is used to increase the feedwater temperature in different stages, usually 18 to 25[38,39]. The more stages are applied, the more energy efficiency will be reached. Recently a novel MSF system with 45 stages has been developed, which is comparable with SWRO in terms of energy efficiency. The water recovery ratio of conventional MSF systems is about 10-30%, which leads to a high amount of brine at the end of the process. Part of the brine will be recirculated to reduce the brine and the feedwater[40]. However, the produced water has a high quality. The salinity of the produced water is reported to be less than 10 mg/L in some publications.[41].

Although MSF has been developed after MED, it has had significant success since the middle of the 20th century, particularly in the Middle East and North Africa. Its general ease of operation, minimal to no pre-treatment requirements, quality distillate, and ability to desalinate a large volume of water in one plant made it a popular choice, specifically when integrated with a co-generation power plant[42]. However, one of the benefits of MED is the ability to be directly coupled with renewable energy sources. Several projects have been conducted to investigate the feasibility of solar-powered MED units, especially the combination of concentrated solar power (CSP/MED).

Table 1 Comparison of MSF and MED as thermal-based technologies with SWRO as a membrane-based water purification method.

Parameter	MSF	MED	SWRO
Pre-treatment requirements	Minimum	Minimum	Highest
Chemical consumption	Medium	Medium	Low-Medium
Sludge production	None	None	Pre-treat
Scaling propensity	Low	Low	Lowest
Fouling propensity	Low	Low	Higher
Operational simplicity	Lowest	Medium	Higher
Reliability / Robustness	Highest	High	Moderate
Capital cost	Highest	High	Lowest
Electrical consumption (kWh/m³)	4	1.2	4
Steam consumption (GOR)	10:1	7:1	n/a
Concentration factor (Brine/feed)	1.7	1.7	1.7
Top brine temperature (°C)	110	70	n/a
Feedwater pressure (bar)	2	2	60
Feed: Product flow	> 7:1	>7:1	2.2:1
Product TDS (mg/L)	< 25	< 25	450

The performance of thermal-based desalination systems can be measured using a so-called gained output ratio (GOR) or performance ratio (PR), defined as the ratio of the produced drinking water to the consumed steam. PR significantly depends on feedwater temperature (pre-heat system) and temperature of the generated vapor:

$$PR = \frac{freshwater\ produced\ [kg/h]}{required\ steam\ [kg/h]}$$

Equation 1

PR of the commercial MSF units is about eight, and the more advanced systems can reach a PR of nine[43]. The low-pressure output of the Combined Heat and Power (CHP) plant can be connected to MSF to re-use the steam temperature, mainly to pre-heat the feed water[44].

1.3.2. Multi-effect distillation (MED)

An older technology, submerged-tube MED, suffered from significant scaling and a low level of heat transfer. The horizontal tube spray-film evaporators began to appear in the 1970s, which led to a renaissance in MED technology, resulting in lower operating temperatures and reduced recirculation rates, requiring less pumping and lowering energy demand. Furthermore, while the capacity of the early designs was limited to less than 500 m^3/day, the recent systems can provide up to 36,000 m^3/d[45]. Similar to MSF, in MED technology, water production occurs in several steps, typically, 8-16 stages[46]. In general, the energy efficiency of MED technology is higher than the MSF[47, 48]. In seawater applications, it is often possible to use the kinetic energy of the steam to enhance MED performance by employing a steam jet ejector.

The water recovery ratio of conventional MSF units is between 20 and 30%[49]. Nonetheless, the biggest challenge in this method is the sediment. Reducing the boiling temperature to around 55° can mitigate this effect and the corrosion issues, which has been successfully applied and reported in some recent systems. In addition, inexpensive materials like aluminium alloys can be used for low-temperature MED systems, which leads to less CAPEX.

1.3.3. Vapor compression (VC)

Mechanical compressed vapour systems are used in VC techniques to increase the pressure and temperature of the evaporated vapour from the feedwater. As vapour is compressed twice during this process, this technology is known as mechanical vapour recompression (MVR) or mechanical vapour compression (MVC) unit[50]. The first MVC system was developed in the 1980s to change the energy source of the thermal-based desalination system to compete with RO technology. However, still, the power consumption of RO is far less than VC systems. As mentioned in table 2, the typical energy demand of VC technology is between 8 and 12 kWh/m^3, and the water recovery ratio is about 40-50%.

1.4. Using renewable energy (RE) systems for water desalination

Fossil fuels or grid power are commonly used to power desalination systems. Although the capital cost of such systems is comparatively low, the resources, i.e., electricity and fuel, are barely available in remote areas. According to a report by UNDP/WHO, in the least developing countries (LDCs), only 21 % of and in Sub-Saharan Africa, 26 % of the people have access to electricity. This problem is even more severe in rural areas of LDCs and sub-Saharan Africa, where the electricity access percentage is 13 % and 11 % respectively. In addition, in LDCs and sub-Saharan Africa, only 9% and 17% have access to modern fuels (electricity, liquid, and gaseous fuels). Consequently, using REs to power desalination systems is a promising solution for such circumstances they need less infrastructure, i.e., a reliable grid or roads.

Table 2 Typical electrical and thermal power consumption for thermal technologies

Process	Thermal consumption (MJ/m³)	Electrical equivalent of thermal consumption (kWh/m³)	Electrical consumption (kWh/m³)	Total consumption (kWh/m³)	Product water quality (mg/l)	Product water cost ($/ m³)
MSF	190–282	15.83–23.5	2.5–5	19.58–27.25	~10	0.56–1.75
MED	145–230	12.2–19.1	2–2.5	14.45–21.35	~10	0.52–1.5
MVC	none	none	8–12	7–12	~10	2.0–2.6
TVC	227	14.5	1.6–1.8	16.26	~10	0.87–0.95

The major challenge associated with small-scale renewable-powered desalination systems is the intermittent and variable energy availability, requiring the system to adjust to changing parameters. The conventional solution for dealing with variations in RE is applying a storage system to stabilize the energy. Batteries are used in systems where the primary energy source is electricity, like RO, and hot water tanks can be used for thermal-driven systems. Despite all challenges in using Renewable Energy-based desalination (RED) systems, more than 130 projects have been commissioned recently[51]. As shown in table 3, almost all kinds of Renewable Energy (RE) resources can be used to power desalination technologies[52]. Nevertheless, solar power is the most suitable energy source for RED projects. Solar energy can be used in both heat and electricity forms, and more than 60% of RED systems are coupled with solar energy[53]. Regarding solar thermal energy, various panel technologies have been

applied and tested in the last few years, including unglazed solar collectors, linear Fresnel, flat-plate solar collectors, and evacuated tube solar collectors. However, concentrating solar power (CSP) is the most fitting technology, which can easily be integrated into different thermal-driven technologies[54].

Table 3 different renewable energy resources can be coupled with desalination systems. However, other resources, such as biomass and hydropower, are rarely used for REDs as these energies intrinsically need water[55].

Desalination plant name	Location	Desalination technology	technology Capacity (m3)	Renewable energy source
Kimolos	Greece	MED	200	Geothermal
Keio University	Japan	MED	100	Solar collectors
PSA	Spain	MED	72	Concentrating solar power (CSP)
Ydriada	Greece	RO	80	Wind turbine
Morocco	Morocco	RO	12-24	Photovoltaics (PV)
Oyster	Scotland	RO	n.a	Wave energy

In coastal regions, where seawater and wind energy are widely available, wave, tidal energy, and wind turbines can be used to power the RED plants. Nevertheless, this application is limited to desalination technologies with high electrical energy demand, namely RO and ED[56]. The first commercial RED plant using wave energy was recently designed and installed in Australia as a hybrid system. In contrast, offshore and onshore wind turbines are used in several projects[57, 58, 59]. However, still produced water cost significantly depends on the price of the wind turbine, which, compared to other RE sources, is relatively high[60].

Geothermal energy also gained noteworthy attraction during the last few years as a reliable RE source because it is more stabilized and has fewer fluctuations. Geothermal plants can provide at least 180 °C, which perfectly matches desalination applications[61]. The first feasibility studies show that geothermal-based REDs can provide 95% of the energy demand, saving about 60% of OPEX[62]. Recently, different groups worked on this type of RED[63], and even some progressive ideas like integrating geothermal into RO[64] or a hybrid thermal- and membrane-based desalination unit[65] are being investigated. Fig. 9 summarises the integration possibility and market share of different RE resources in desalination technologies.

1.5. Solar-based reverse osmosis systems (PVRO)

As explained in section 1.2.1, RO is the most successful technology in the water desalination market. On the other hand, fig. 9 shows that this method perfectly matches RE resources. Therefore, solar-powered RO (PVRO) is the most promising solution to provide water in remote areas. As shown in fig. 10, a conventional PVRO system typically includes photovoltaic (PV) panels as the energy source, a battery unit including a charge/discharge controller as the energy stabilizer, DC/AC inverter to provide AC power for the pumps and the RO unit.
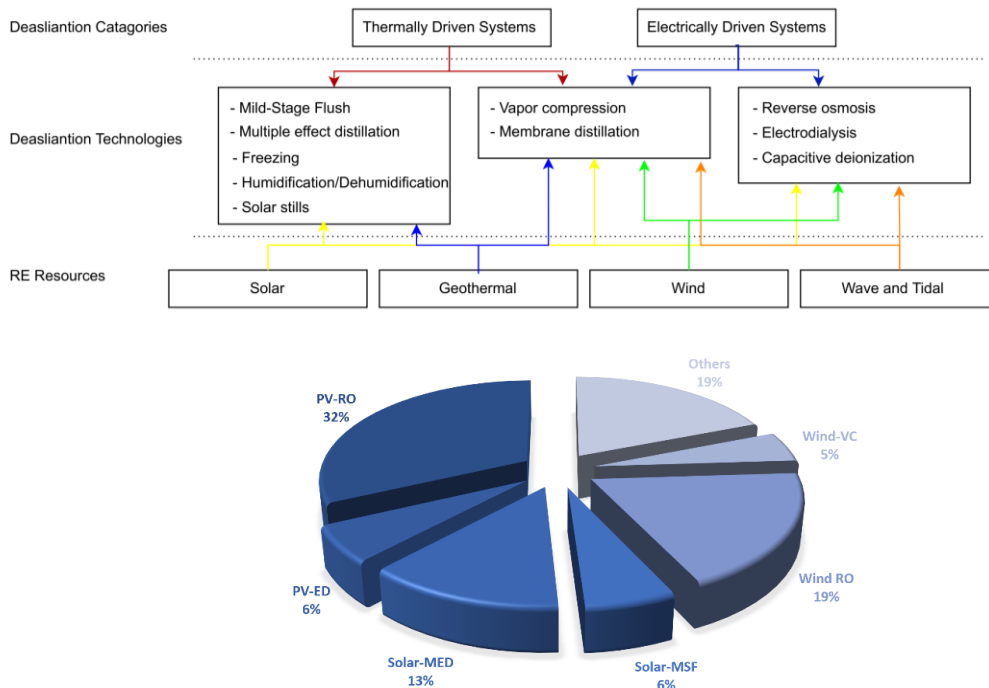
Figure 9 top: RE resources can be matched with different desalination technology based on the primer energy need, bottom: solar energy is the most relevant RE source for desalination, and almost 60% of the REDs are powered by solar energy [66].

Batteries are expensive and have a limited lifetime. Although the charge-in/charge-out efficiency of a typical deep-cycle lithium-ion battery is high, i.e., 90-95 %, the Depth of Discharge (DoD), even for recent batteries, is about 75 – 80 %. In addition, batteries perform worse and degrade faster at higher temperatures. Specifically, with increasing operating temperature, the following issues occur a) the battery capacity decreases, b) the charge efficiency decreases, and c) the self-discharge rate increases. This approach results in a high cost of water production, reduced energy efficiency, and increased system complexity[67]. In recent years, PVRO systems have been the subject of some research projects; Gocht et al. performed preliminary experiments to determine the technical feasibility of a transiently

operated RO system. To investigate the effect of fluctuations on the RO performance, the transmembrane pressure (TMP) was changed linearly at different speeds but up to 18 bar min^{-1}, while the water production ratio and permeate salinity were observed frequently. Although no detailed results were presented, it was concluded that nothing was observed that ruled out the transient operation of a RO membrane system[68]. Pestana et al. also agree with this conclusion, stating that RO membranes can function in a variable manner without deteriorating[69].
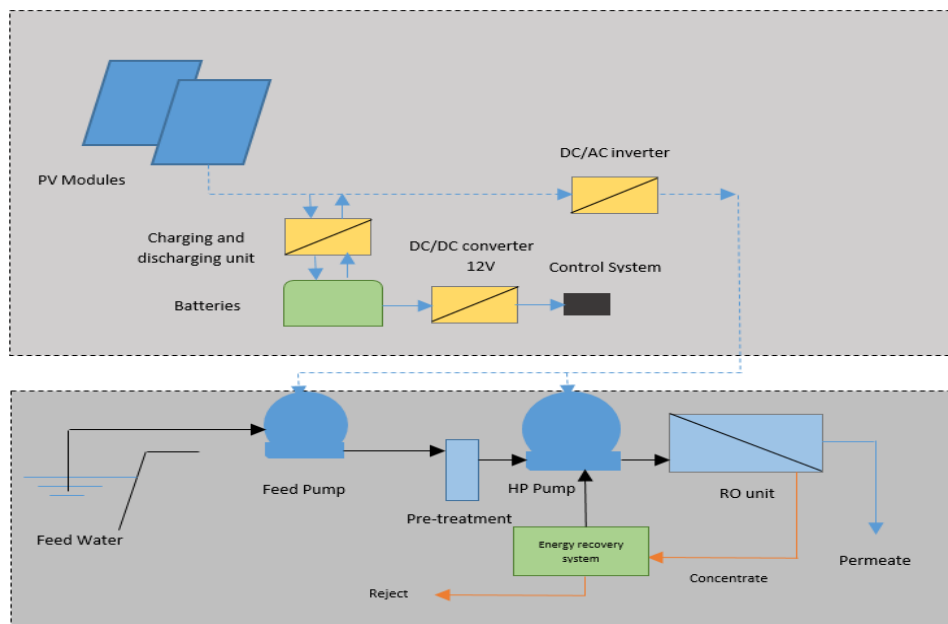
Figure 10 simplified process and connection diagram of a conventional PVRO consisting of a battery unit to provide fixed current and voltage for RO pumps.

Battery-based PVRO systems are known as the first generation of this technology. During the last few years, several attempts have been made to remove the batteries from PVROs. Thomson and Infield [70, 71] proposed a PVRO plant, which could operate without batteries. They designed and tested a laboratory-scale system with a 3 m^3/d capacity powered by a 2.4 kWp PV array. Bilton has designed a battery-less small-scale photovoltaic-powered reverse osmosis desalination plant with a capacity of 300 L/day by using DC pump and custom control electronics. A PIC24 microcontroller has been used to control a DC/DC step-down converter that receives power from the solar panels and converts it to the voltage desired by the two DC boost pumps[72].

Finally, in 2017 a French company, MASCARA[1], developed, patented, and commercialized a battery-less PVRO system as the second generation of this technology[73]. Currently, most of the systems in the market are based on this method. The third generation of PVRO systems is designed and tested in this work. Section 2 describes the technical details of the second and third generations.

---

[1] https://www.osmosun.com/en/

Chapter 2

Dynamic Solar-Powered Reverse Osmosis (PVRO)

---

2. PVRO development path

As explained in section 1 (See fig. 10), RO systems integrated with photovoltaic power (PVRO) are the most successful type of RED[74]. Especially for small-scale systems, PVRO provides many advantages, such as low CAPEX, reasonable OPEX, and uncomplicated commissioning. The first report about the application of a PVRO system was published in January 1982[75]. This system is installed in Saudi Arabia, on the shore of the Red Sea, to provide drinking water for about 250 people. A DC pump was used to desalinate the feed water with more than 42000 mg/L salinity extracted from a borehole at the coast of the Red Sea. The water production capacity was less than 300 lit/h with a 22% recovery ratio. This technology, i.e., 1st generation of PVRO, was uncomplicated and robust. The technology involves batteries to stabilize the inherent fluctuation of solar energy and to provide fixed voltage for the pumps. Despite of simplicity and robustness of the design, the 1st generation suffers from high CAPEX and OPEX of the battery unit, especially in hot, humid, and remote areas.

During the last 40 years, various developments and optimizations have occurred to reduce the cost of the PVRO system[76,77]. Today desalination cost, by using RO technology, is around 1300-2500 USD/m^3/day[78] and still is reducing[79]. Price reduction and performance increment of PVRO components such as PV panels, battery units, inverters and membranes accelerated the price decline and increased the number of PVRO projects worldwide[80]. However, another significant cost change in PVRO technology was developing battery-less systems[81]. The technical details are described in section 2.1, and in general, removing the batteries from the PVRO systems remarkably reduced the investment costs and maintenance expenditures of the first generations. Although most of the market is based on this technology nowadays, removing the batteries, as the energy stabilizer unit, led to high fluctuations in the pumps and membranes[82], which is still unsolved in this technology.

The focus of this work was improving the 2nd generation by developing a new solution to control the energy fluctuations in a battery-less PVRO system. A new control system has been developed and more instrumentations are added to the conventional RO to make it compatible with the control system. Regarding the software, a new control algorithm is programmed. Two similar prototypes are designed and built to be tested in Germany as the accelerated test bench, and the second system was installed in Capes Coast, Ghana to provide field test data. Pro and cons of all three PVRO generations are compared in table 4.

Table 4 based on the technology, PVRO systems can be divided into three categories, including the developed method in this work. The advantages and disadvantages of each category are summarised in this table.

Category	technology description	Development date	Advantages	Issues
1st Generation	PVRO system including PV panels, inverter, batteries, and RO	1982*	Providing fixed and stabilized power for the pumps and RO	High CAPEX and OPEX because of the batteries
2nd Generation	Battery-less PVRO	2017**	Reducing investment and maintenance costs by removing batteries	High pressure fluctuation in mechanical parts
3rd Generation	Multifunctional driver (MFD) technology	2019	Providing fixed and stabilized pressure and water production	-

*The performance report of the first PVRO was published in January 1982.

** developing a commercial product.

2.1. State of the art: 2nd generation of PVRO

Conventional PVRO systems, i.e., first generation, include an electrical storage unit to stabilize intermittent and fluctuant solar power. However, in the second generation, the main idea was to balance the power consumption of the PVRO with the available solar energy[83,84]. In this way, batteries can be removed from the water treatment plant. To control the energy demand of the system, variable speed pumps are used. Actually, it is possible to adjust the pump power by controlling the pump's frequency. The schematic view of the system is shown in fig. 11.

The main challenge in this technology is to guarantee water quality while the pressure and frequency of the pumps continuously change. The working parameters should be adjusted so that the energy balance between input energy from the PV system and the energy demand of the RO is always reached without using any batteries.

The 2nd generation has solved the battery issues, but it is still based on conventional inverters. Even though inverters are robust, efficient, and reliable nowadays, they are not designed for dynamic desalination applications. Removing the batteries can reduce PVRO production costs. However, on the other hand, all solar fluctuations will be delivered to the system directly as there is no energy stabilizer between RE and PVRO. Especially in sharp energy reductions, which happen at least once a day[85], a rapid frequency decline will occur. While such a fast energy reduction is well practicable and tolerable for electrical components like

inverters and motors, the mechanical parts like pumps, valves will be damaged. Particularly the sharp energy decline shortens the membranes' lifetime and affects the membranes' integrity, as it will be exposed to sudden pressure fluctuations and strong backwash vibrations due to the forward osmosis[86].
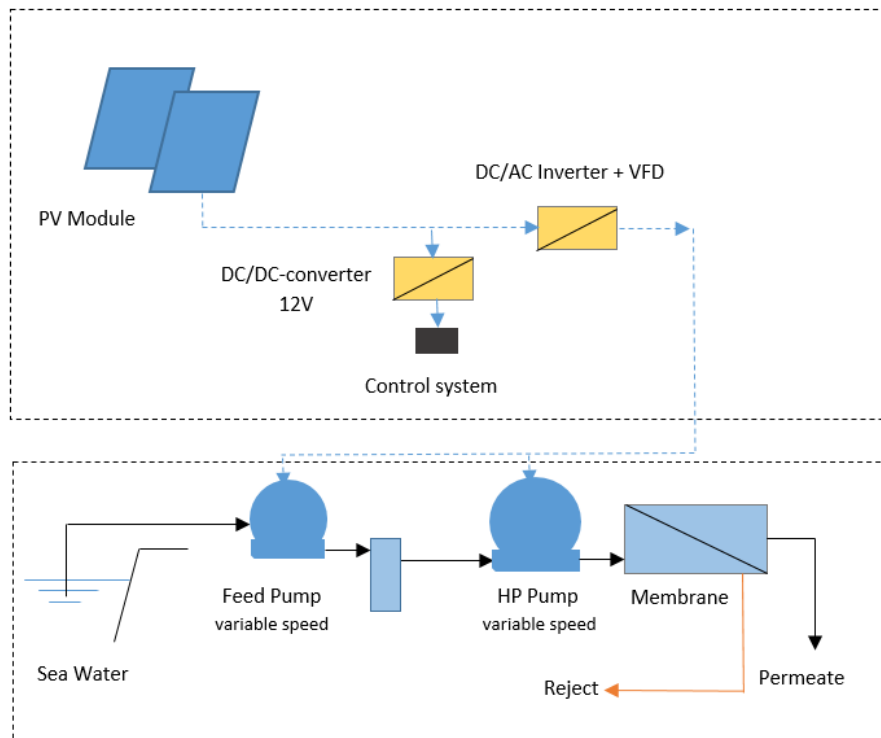
Figure 11 simplified process and connection diagram of the second generation of PVRO systems. By using this technology, batteries are eliminated from PVRO systems.

2.2. Developed technology: 3rd generation of PVRO

In the developed technology, a Multi-Functional Power Driver (MFD) replaced the conventional inverters from PVRO systems to solve all mentioned drawbacks regarding the second generation. As shown in fig. 12, the changes are just in the control system, and the desalination system is a conventional RO unit including a feed pump, high-pressure pump, pressure accumulator, pre-filtration and membrane system.
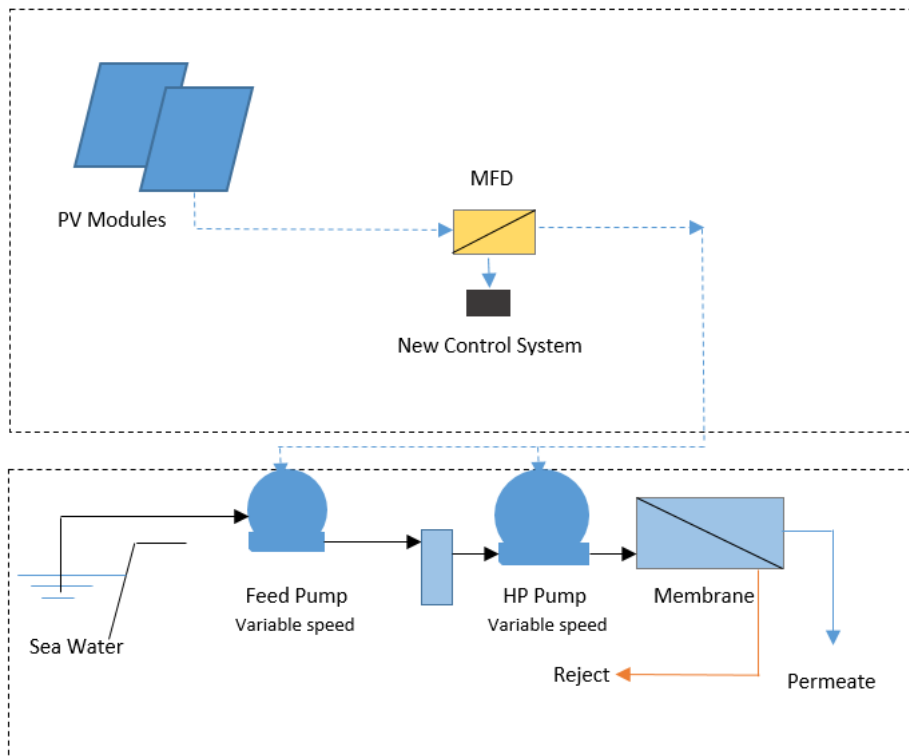
Figure 12 simplified process and connection diagram of the developed system. Instead of conventional inverters, a new energy management system (Multi-Functional Power Driver (MFD)) is developed, which is particularly compatible with the dynamic PVRO systems.

In addition, as shown in fig. 13, by using MFD, unnecessary energy transformations can be avoided, leading to significant energy and cost savings. To investigate the performance, the whole system is simulated in Matlab/Simulink®, and simulation results are explained in Chapter 3. The following sections provide explanations of the components' details and specifications.

Figure 13 Above: energy transform stages in a conventional system. Bottom: energy transform stages in the new MFD, half of the transform stages are removed.

2.2.1. Developed hardware

a- Multi-Functional Power Driver (MFD)

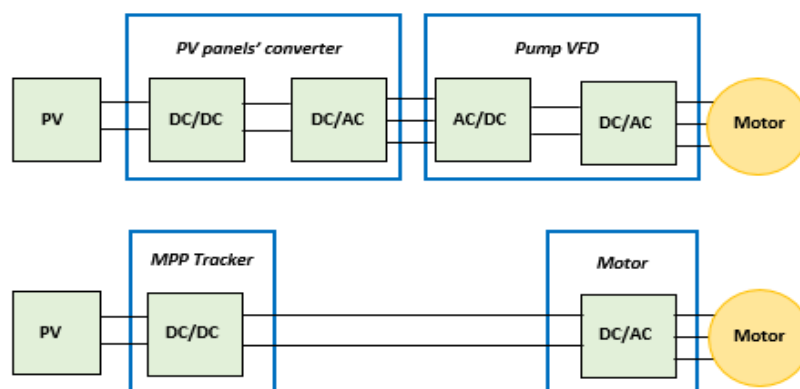To transfer the energy from PV panels to the desalination unit, a new energy management system, including hardware and software, is developed in this work. The first stage of MFD is a maximum power point (MPP) tracking system, which ensures that the output of PV panels (voltage V, current I) is matched to that being drawn by the system (the load). The second part of the driver is the DC-Bus regulator, which delivers appropriate power to the DC-Bus of a customized frequency driver. The regulator monitors and adjusts the output of the inverter on 600 VDC. The MFD has a modular structure to increase efficiency, especially under partial load conditions. Furthermore, the modular structure makes the driver scalable. While in conventional systems, four energy transform stages are needed to supply a variable speed pump (i.e., DC/DC and DC/AC in the PV system and subsequently AC/DC and DC/AC in the pump VFD) by this method conversions are diminished to DC/DC in the PV system and DC/AC in the pump VFD (see Fig. 13). In addition, principally, the dissipation of energy in DC cables is lower than in the case of AC cables:

$$P_{dc,loss} = 2 \cdot I_{dc}^2(t) \cdot r_{dc} \qquad\qquad \textit{Equation 2}$$

$$P_{ac,loss} = 3 \cdot I_{ac}^2(t) \cdot r_{ac} \qquad\qquad \textit{Equation 3}$$

The voltage in DC conductors is higher than for AC. Therefore, the current will be lower for the same power. As a result, according to equations 2 and 3, the energy dissipation decreases severely as it is related to the square of the current. On the other side, AC power suffers more "drop" because r_{dc} just involves resistance. Whilst r_{ac} includes impedance, which is always greater than resistance because impedance combines resistance with reactive effects such as capacitance and inductance, which are strictly positive for any given conductor in practice. This power loss is noteworthy when the cable distance between PV modules and the RO system is significantly prolonged.

The last part of the driver is a customized frequency driver, which has an additional interface for DC input. Standard VFDs only have one interface for AC input, and the first stage of VFD is an AC/DC converter. This stage is skipped in the developed frequency driver. A capacitor in the DC-bus absorbs any ripples and delivers a smooth DC voltage. The last stage of the VFD is a DC-to-AC inverter which generates AC current with the desired frequency. The output from

the frequency driver has a "rectangular" waveform. In general, a rectangular wave is not the perfect choice for all distribution purposes, but it could be used to supply a pump. The internal circuit of a typical VFD is shown in Fig. 14, and the internal circuit diagram of the developed system is depicted in fig. 15.
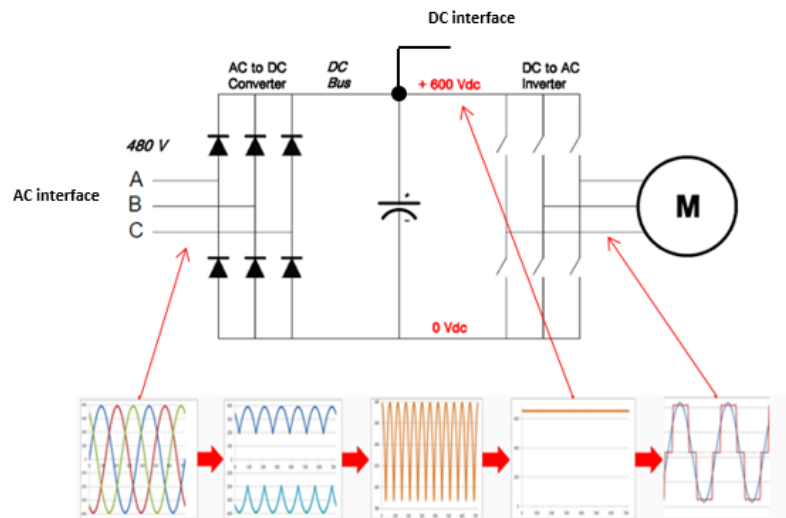

Figure 14 VFD internal circuit and output of each stage. The final outcome is a "rectangular" waveform with the desired frequency compared to a similar sinusoidal wave [87].

The control unit includes one master controller and three slave controllers (see fig. 15). This structure allows the control system to react very fast to any changes in the input conditions, including fluctuations in solar irradiation and feed water quality. One of the slave controllers is responsible for receiving and sending the control signals (digital and analogue signals (4-20 mA). The internal communication between controllers is based on CAN protocol, while the communication between the master controller and IoT router is based on Modbus protocol. The control system has three unique mechanisms to compensate for the fluctuations. These three approaches should be adjusted simultaneously and should work together smoothly to compensate for the energy drops in few seconds:

1- The first mechanism is using the stored energy of installed capacitors (see fig. 16), which can provide the nominal power of the system for about 20 seconds. The control system should balance the power consumption within this time.

2- The second stage is controlling the frequency of the pumps. There are three ratios of changing the frequency, deponing on the intermediate circuit voltage. When the voltage is in the normal operating range, i.e., 630 to 560 V, the slow ratio of 0.007 - 0.001 Hz/ms is sufficient. When the intermediate circuit voltage drops below 560 V,
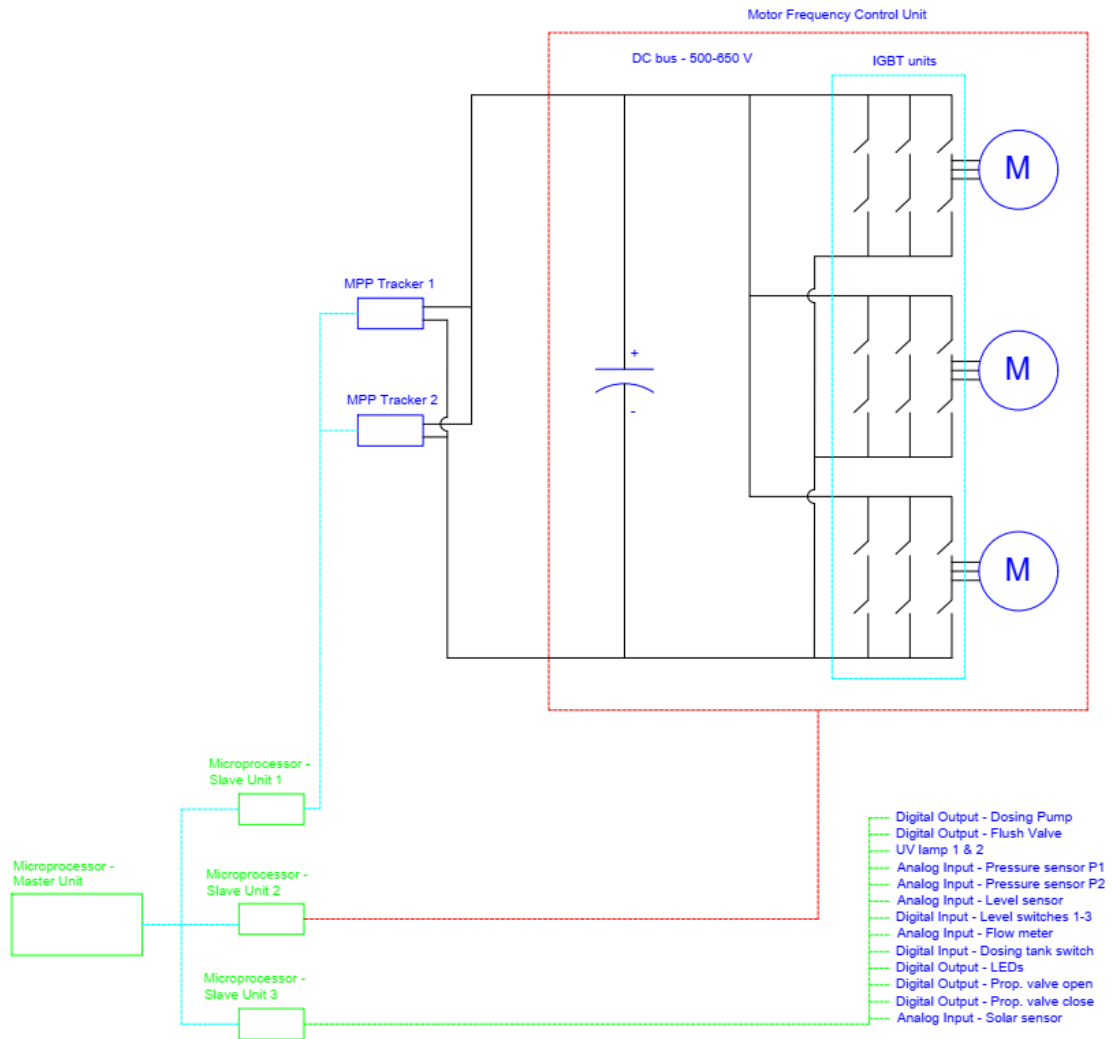
Figure 15 schematic view of the hardware structure of the developed control system.

the rate of frequency change is increased by a factor of 3. In the rare cases that the voltage drops below 540 V, the rate of change is increased by a factor of 10, i.e., 0.07 - 0.01 Hz/ms. This method assures smooth operation of the system in sunny conditions and guarantees fast reaction in low irradiance situations.

3- The last stage, which is slower than other mechanisms, is adjusting the TMP by using a controllable proportional valve (Gulex N802/8U/4S/K - see fig. 17), which is installed on the brine output. The valve can be opened/closed completely in four seconds. Therefore, the microcontroller can close/open the valve in each cycle by 0.25%.

By applying these three stages, the control system can smoothen the sharp fluctuations without using batteries. The performance of the MFD is investigated in Chapter 5 and pictures of the control unit and the pilot system are shown in fig. 16 and 17.
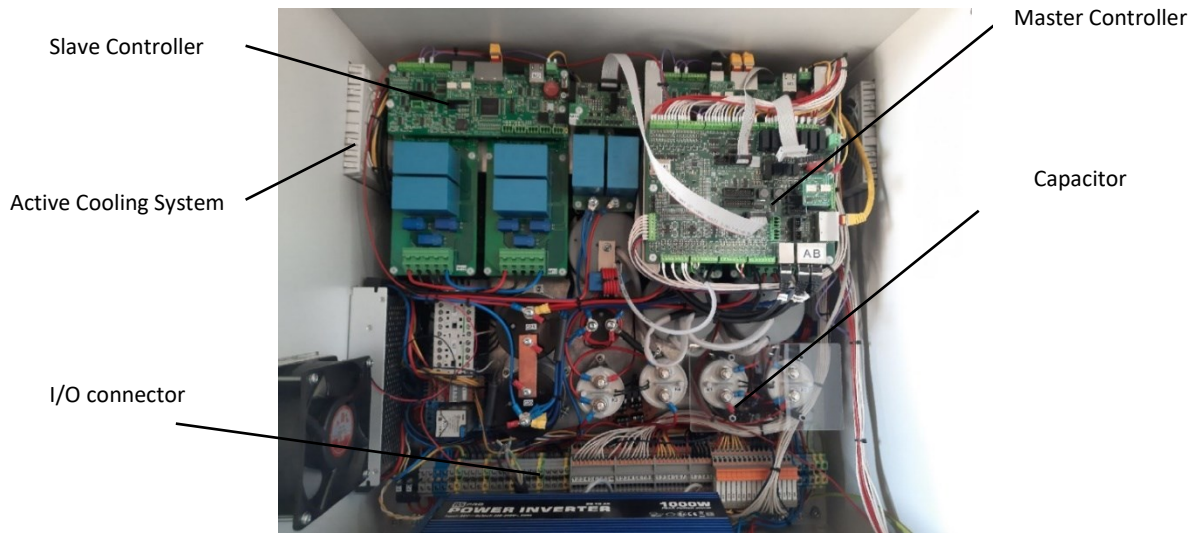
Figure 16 the developed MFD controller, including one master and three salve controllers.
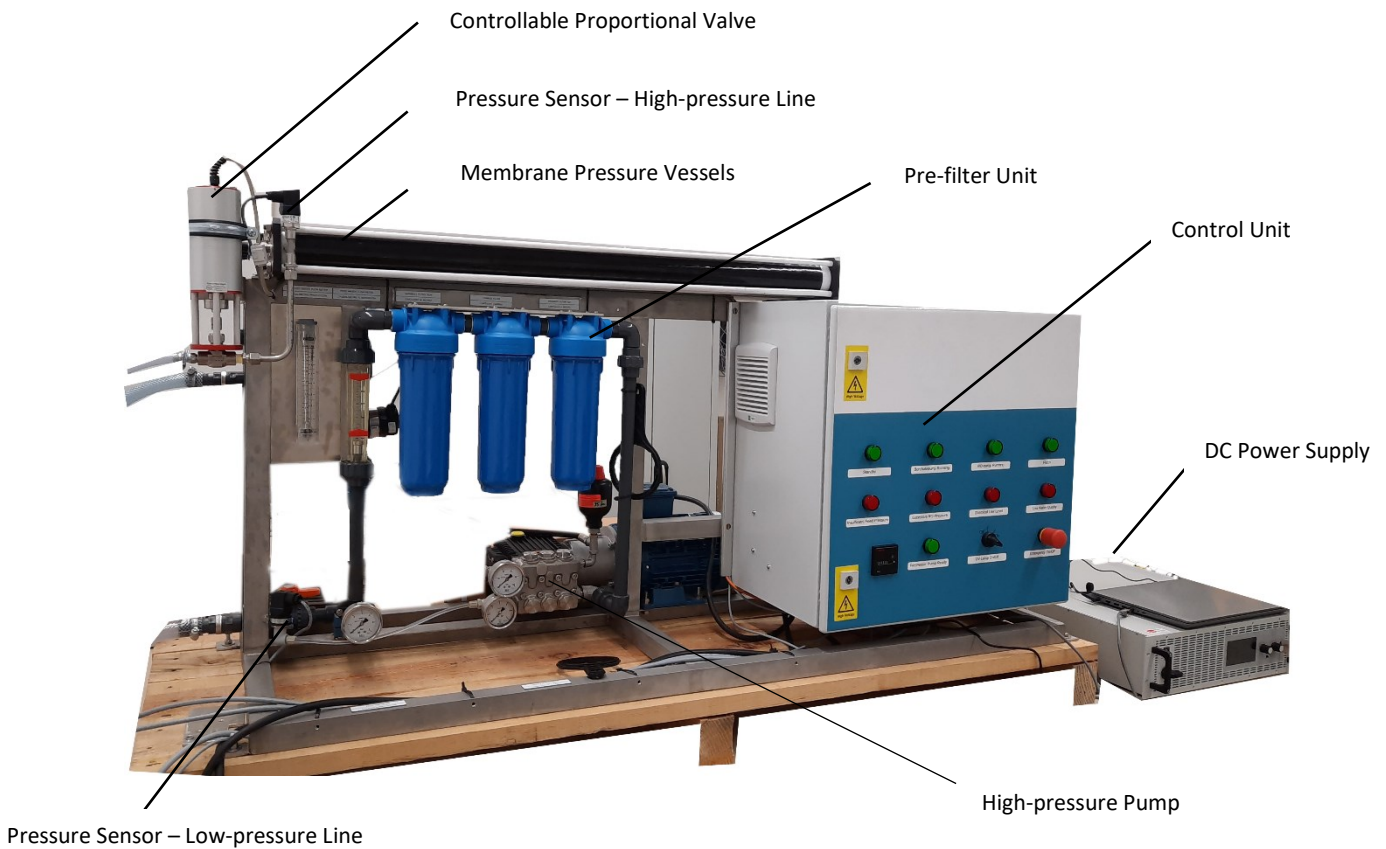
Figure 17 the developed pilot project, which is installed in Ghana.

The other unique feature of the MFD technology is controlling all pumps through one controller. As shown in fig. 18, in conventional systems, two separate PV arrays will be installed to supply the borehole pump and PVRO, respectively. However, in the MFD technology, all pumps, including the borehole pump, are connected to the same controller. Using two separate PV arrays makes the installation more straightforward, but it is the most

significant source of energy waste. In MFD technology, all generated solar energy will be transferred to one unit, and the master controller decides to share the energy between the pumps based on the operating condition of the system.

In addition, another application of the developed concept is using the PVRO as a controllable load in the mini-grids to increase the frequency stability, which is explained in sec 2.3.
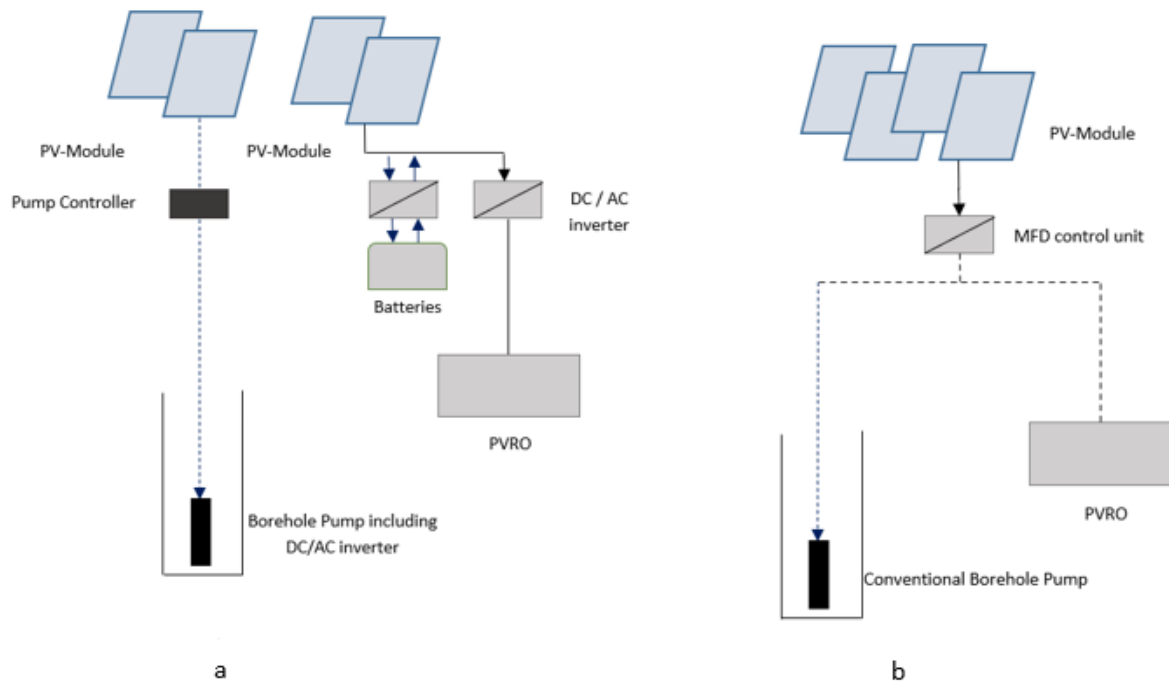

Figure 18 PV structure of a: conventional PVROP system including two separate PV arrays b: MFD technology, which can integrate the PV modules.

b- Desalination System

The desalination technology used in this work is based on RO, and to make it compatible with the MFD, more instrumentation, namely pressure sensors, digital flowmeters, and a controllable valve, is added to a conventional RO plant. Two prototypes are designed and assembled to measure the system's performance. The first system is installed in Cape Coast, Ghana, on the real condition, which takes the water from a coastal borehole (Appendix 1 shows the borehole water analysis), and an eight kWp PV system powers the system. The second system is tested under the simulated condition as an accelerated test bench in Germany to compare the performance results and validate the simulation software. The feed water was simulated according to the borehole water analysis, and two DC power supplies were used to simulate the PV power. To extract the data from the system in Ghana, a remote monitoring system is designed, which is described in section 2.2.3. A Java-based graphical

user interface (GUI) is designed to visualise and store the accelerated test bench data. Fig. 19 shows the schematic design of the prototype. A closed water loop is designed for the accelerated test bench to save water consumption, while the system in Ghana works in normal conditions. The results and details of the tests are explained in chapter 5.

As described above, the developed PVRO operates in dynamic mode and adapts itself to the available PV power at any time of the day. The electrical power consumption of the system is equal to the hydraulic power demand of the pumps, which can be calculated from the volumetric flow and the water pressure, as well as the hydraulic and electrical efficiency of the asynchronous motors. The available PV power is continuously measured and converted into three-phase current by the MFD to adjust the system's power consumption. The frequency of the three-phase current is a function of the pumps' speed, which determines the generated flow rate of the pumps. By changing the water flux, the hydraulic power consumption of the system is adjusted. The required pressure depends on the osmotic pressure of feedwater, and the primary task of the control system is to keep the working pressure constant by changing the feed flux through the proportional control valve. In fact, adjusting and stabilizing the transmembrane pressure (TMP) is the biggest challenge of the control system as the input power and inlet water quality are altering continuously. Because, as mentioned before, pressure fluctuations can harm and reduce the lifetime of the membranes.

As shown in 19, a centrifugal pump (feed pump) pumps the feed water through three pre-filters, including two porous filters with different pore sizes, i.e., 20µm and 5µm, and one activated carbon filter based on adsorption. The feed pump is necessary to overcome the pressure loss of the pre-filtration stage and simultaneously provide the inlet pressure of the following piston pump (high-pressure pump). The inlet pressure is essential to prevent cavitation at the high-pressure pump. The prototype system in Ghana has a multimedia filter before the cartridge filters to filter big particles (bigger than 50µm). This additional stage is necessary because, in Ghana, the feed water source is a borehole containing sands and other big particles. After the pre-filtration system, the high-pressure pump is installed to pump the feed water to four pressure vessels connected in series. Each pressure vessel involves one brackish water membrane (type: Polyamide (PA), Spiral-Wound Thin-Film membrane). The properties of membranes are explained in table 5.
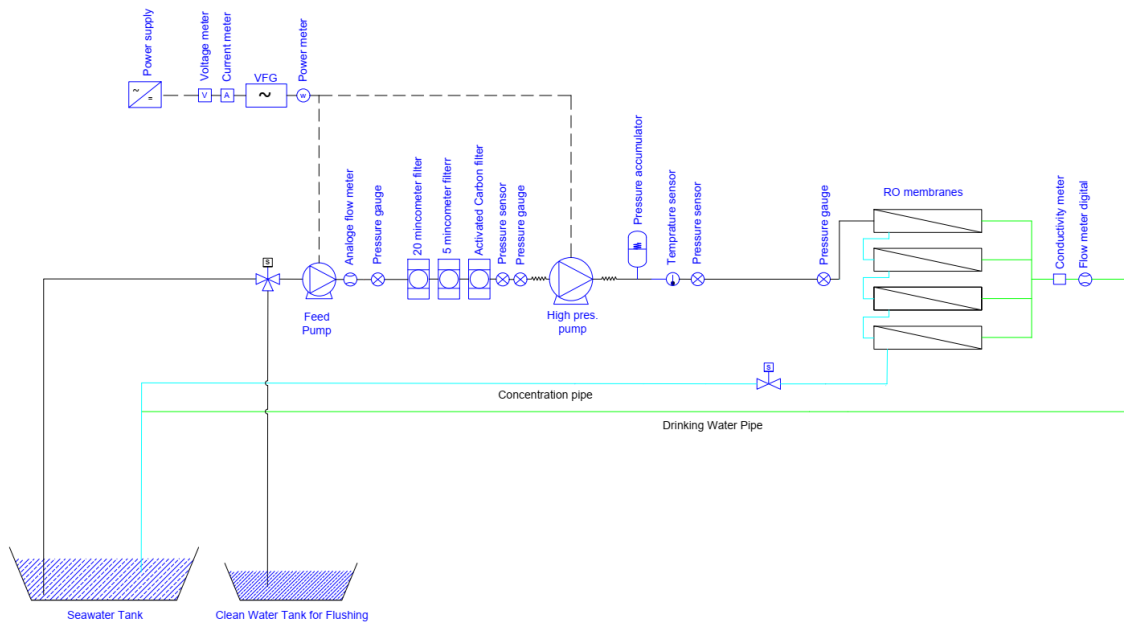
Figure 19 Piping and instrumentation diagram of the developed system.

The controllable valve can adjust the applied pressure on the membranes. However, this pressure should always be higher than feed water's osmotic pressure to produce water. About 30% of the feed water can pass through the membrane and flows out through the permeate side of the pressure vessels as drinking water. The concentrated water retained by the membrane has a higher salt content and is discharged through the brine outlet.

Table 5 properties of the membranes, which are used in the pilot project and the test bench.

Salt rejection ratio	Min. 99.4%	Recovery ratio	Max. 15%
Permeate Flowrate	125 l/h	Pressure Drop	Max. 0.1 MPa
Feed flowrate	Max. 1360 l/h	Operating pressure	Max. 4.14 MPa
Concentration flowrate	Min. 0.23 m³/h	Effective area	2.5 m²
Operating pH Range	2.0–11.0	Feed water Turbidity	1.0 NTU
Membrane size	40.0 x 2.5 inch	Feed water SDI	Max. 5.0

2.2.2. Developed software

The main part of this work was developing, testing, and optimizing the system's software. Two microprocessors from Texas Instrument are used in the MFD to control the whole plant. The software is written in C programming language, and a simple software structure is depicted in fig. 20. The software involves independent but interconnected "switch-case" syntaxes and details of each syntax are described in appendix 2.
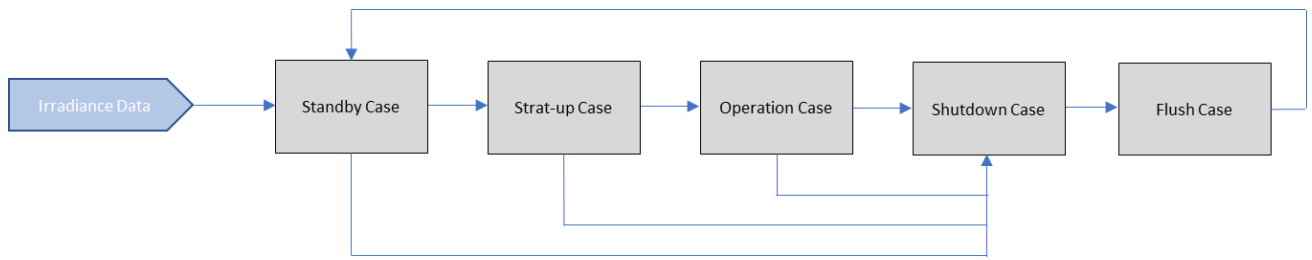
30

Figure 20 Software is mainly based on "switch-case" syntaxes, which makes the code easier to be followed and be debugged. If certain conditions are reached, the software can jump from one case to another; otherwise, the software stays in the same case, making the process faster.

2.2.3. Remote Monitoring System

A remote monitoring system is designed to gather, visualise, and analyse performance data. A phyton-based code is deployed on an Elastic Container (ECS) of Amazon Web Services (AWS)[2] to receive the data from an on-site router (Teltonika RUT240[3]). ECS transmits the data to InfluxDB[4], a database where the parameters are stored subsequently to Grafana[5], a platform for visualizing the data. Figure 21 depicts the structure, and Appendix 3 contains the phyton code and a list of the monitored parameters.

2.3. PVRO as a controllable load

Most of the Weak Grids, such as island grids, Smart Grids and Mini Grids, worldwide depend on diesel to supply electricity and look to reach higher shares of renewable energy (RE) to lower their dependence on global energy prices and environmental pollution. However, as weak grids are more sensible against energy fluctuations, integrating RE resources is challenging and limited. The amount of fluctuating RE that can be integrated into a mini-grid is limited by the flexibility of the diesel generator. The major challenge is that electricity produced via volatile energy sources such as wind and photovoltaics can disturb the frequency stability of the whole grid. As a guideline, up to 30% of the peak penetration in the weak grids can be powered by RE which results in an annual RE share of 7-10%, while The European Commission's 2020 targets to generate 20% of Europe's energy from renewable energy[88]. The United Nations Framework Convention on Climate Change (UNFCCC) also

---

[2] https://aws.amazon.com/
[3] https://teltonika-networks.com/de/products/routers/rut240
[4] https://www.influxdata.com/
[5] https://grafana.com/

encourages and supports the increment of RE shares in islands. Dedicated RE-Diesel hybrid mini grids can shift this limit to approximately 20% RE share. Currently, two leading solutions are available:

15 working parameters are measured or calculated by the MFD. MFD generates a JSON file including all date and sends them to the cloud-based monitoring platform.

Amazon Web Services (aws) platform is used as an application programming interface (API) to receive the monitoring data and prepare them for data base and visualization platform

InfluxDB is used as the data base to store the working data as the time series for one month. The platform is open-source and Go programming language is used to develop the platform.

To visualize the working data, Grafana dashboard is used, which is a open source platform. Grafna is compatible with influxdb and without extra programming can be connected to the database.
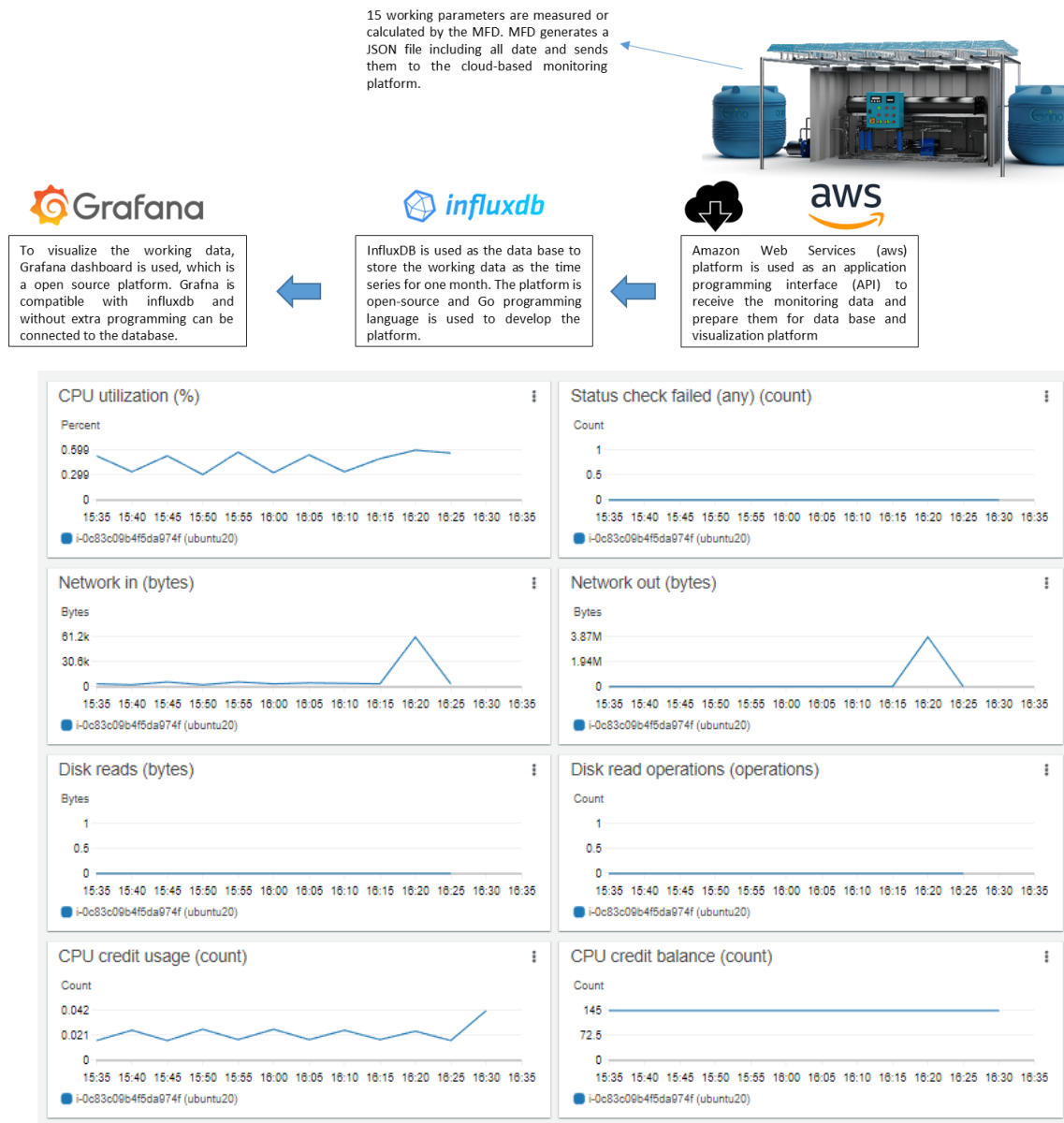
Figure 21 Above - Three different cloud-based platforms are used to gather, store and visualize the operational parameters. Below – AWS dashboard of the remote monitoring controls all receiving data.

1- **Storage integration:** batteries can "hide" RE volatility, but integration costs are high.

2- **Demand Side Management (DSM):** this method aims to adapt consumer demand through various solutions.

DSM can bring significant benefits to maximize the amount of RE in mini-grids, which leads to minimising the overall planning cost. Usually, two types of loads are considered for DSM: interruptible loads (IL) and shiftable loads (SL). In this work, we proposed a new kind of load: **controllable load (CL)**. Using the proposed system makes it possible to shift, interrupt and even partially run the desalination system as a significant energy demand. The desalination system can be operated between 50-120% of its nominal power, based on the grid condition and the forecasting data. Such a flexible load makes it possible to integrate the proposed system even in existing mini-grids, while to integrate SL and IL, it is necessary to design the grid in the planning stage. This method allows it to control the frequency of the mini-grid, maximize the grid solar fraction and reduce fuel cost.

Currently, islands with a high share of renewable energies are rather the exception than the norm. Mainly, conventional electricity producers still must support power production. Nevertheless, there are already promising approaches – such as the projects on the Danish island of Samsø or the Canary Islands of El Hierro, which have already come quite close to the goal of 100% renewable energies for self-sufficient island power supply. In 2016, SMA Solar Technology AG (SMA) commissioned a photovoltaic battery/diesel hybrid power plant on Sint Eustatius, Caribbean island belonging to the Netherlands with 4,000 inhabitants. The proposed concept is shown in fig. 22, which can significantly reduce the battery capacity and, consequently, the project costs. Therefore, such projects could be more economical.
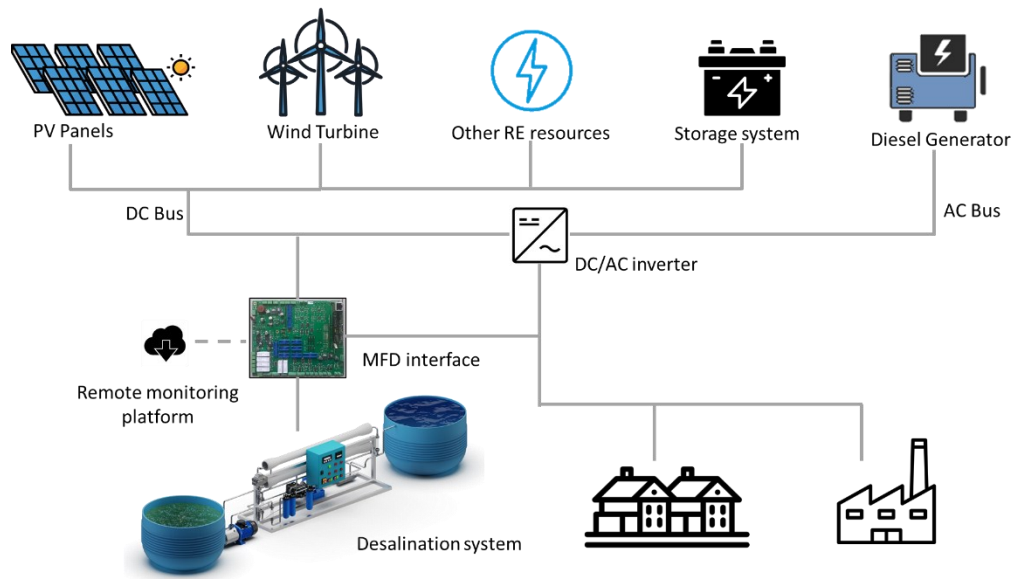
Figure 22 MFD is a microprocessor-based control system. Therefore, it can communicate with other components, and can be used as a controllable load in the weak grids.

As shown in fig. 21, the MFD has enough flexibility and customizability to be matched with different RE sources. Fig. 23 illustrates the general power diagram of the MFD for connecting different AC and DC energy resources with different properties to the RO plant.
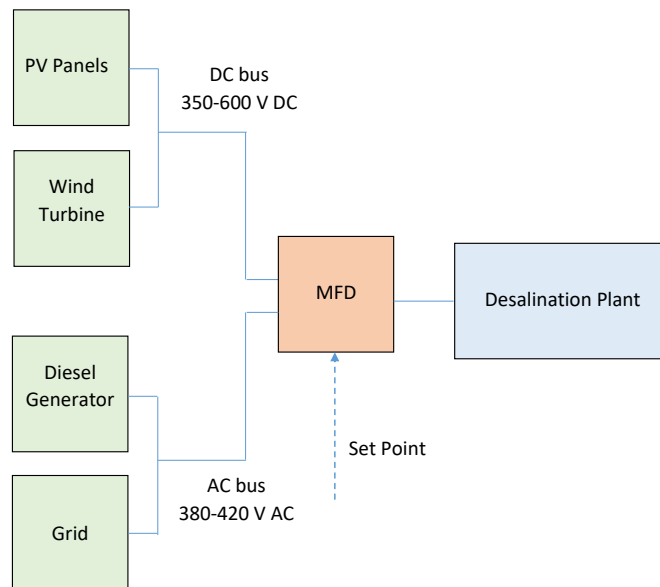

Figure 23 the developed MFD has the flexibility to connect different RE sources to the RO plant while controlling the RO as a controllable load for the mini-grid.

Chapter 3

Simulation of the developed system

3. Simulation Method

Physics-based and empirical equations of each component are presented in this section. These equations are used to develop a non-linear model of the proposed PVRO. Simulink is an appropriate software based on MATLAB functions and provides an interactive user interface for the simulated blocks and components. Therefore, Simulink can be used to simulate and analyse the dynamic systems via mathematical modelling of the plant's components in different blocks.

Each block contains the model equations and Input/Output signals, which can be defined in the MATLAB workspace. However, to simulate the model in Simulink, a proper Solver Method, and Time Series Mode, i.e., continuous time series, discrete time series, or a hybrid of both, should be selected.

In this work, different pre-defined Simulink blocks, like sinks, sources or passive devices are used from the software library, and some blocks are programmed in the MATLAB workspace and added to the model. All key factors, including solar intensity, salt concentration, ambient air temperature, and permeate flux, are considered in the model.

3.1. Solar array model

For the PV panel, the simulation is based on the classic two-diode model. Compared with the single diode model, this method provides more accurate curve characteristics, especially at lower insolation and temperature [89, 90].

$$I = I_{ph} - I_{D1} - I_{D2} - \frac{V+IR_s}{R_P} \qquad \text{Equation 4}$$

$$I_{D1} = I_{01}\left[exp\left(\frac{V+IR_s}{a_1 V_T}\right) - 1\right] \qquad \text{Equation 5}$$

$$I_{D2} = I_{02}\left[exp\left(\frac{V+IR_s}{a_2 V_T}\right) - 1\right] \qquad \text{Equation 6}$$

$$I_{ph} = A_c(C_0 + C_1 T_{cell})G_{mod,tot} \qquad \text{Equation 7}$$

$$T_{cell} = T_{amb} + \frac{G_{mod,tot}(NOCT-293.159)}{800} \qquad \text{Equation 8}$$

Where I_{ph} is the incident light current, and I_{D1} and I_{D2} are the Shockley diode current due to diffusion and charge recombination mechanisms, respectively. I is the current generated by the cells, I_{01} and I_{02} are the reverse saturation current of the diodes D_1 and D_2, respectively.

T_{amb} presents the air temperature in Kelvin and $G_{mod,tot}$ is the total incident solar insolation in $W.m^{-2}$. R_s is the solar cell series resistance in ohms, and R_{sh} is the solar cell shunt resistance in ohms. $G_{mod,tot}$ can be predicted by various models. The ASHRAE clear sky model, via proposing location-specific factors A, B and C, is used for this simulation[91]:

$$I_G = I_N \cos\theta_Z + I_D \qquad\qquad\qquad\text{Equation 9}$$

$$I_N = A \times exp\left[\frac{-B}{\cos\theta_Z}\right] \qquad\qquad\qquad\text{Equation 10}$$

$$I_D = C \times I_N \qquad\qquad\qquad\text{Equation 11}$$

Hourly global irradiance (I_G, W/m^2), hourly beam radiation (I_N, W/m^2), and hourly diffuse radiation (I_D, W/m^2) can be calculated using Eqs. 9 - 11 with factors A and B depending on the installation place. The zenith angle (θ_Z) is also dependent on the two parameters of latitude (Φ) and the hour angle (ω), which may be calculated as per Eq. 12. The n_{th} day of the year (n) is also defined through the declination angle of the sun (δ) as given by Eq. 13:

$$\cos\theta_Z = \sin\Phi\sin\delta + \cos\Phi\cos\delta\cos\omega \qquad\qquad\qquad\text{Equation 12}$$

$$\delta = 23.45\sin\left[\frac{360\times(284+n)}{365}\right] \qquad\qquad\qquad\text{Equation 13}$$

A standard block from the Simscape library is used for the simulation, and parameters are adjusted based on the application. Fig. 92 in Appendix 4 shows the applied parameters and simulation structure of the PV array.

3.2. Maximum Power Point Tracker

The output power of the PV array significantly depends on the applied voltage and current, which can be adjusted by the Maximum Power Point (MPP) Tracker. Climate conditions, namely solar irradiance and ambient temperature can make fast and significant changes to the VI (Voltage-Current) curve of the PV array. Fig. 93 in appendix 4 depicts the effects of ambient conditions on the IV curve of a sample PV system. The MPP tracker consists of a boost converter which can be adjusted via a Pulse-width modulation (PWM) generator. The Equivalent circuit of the simulated MPP tracker is shown in fig. 24.
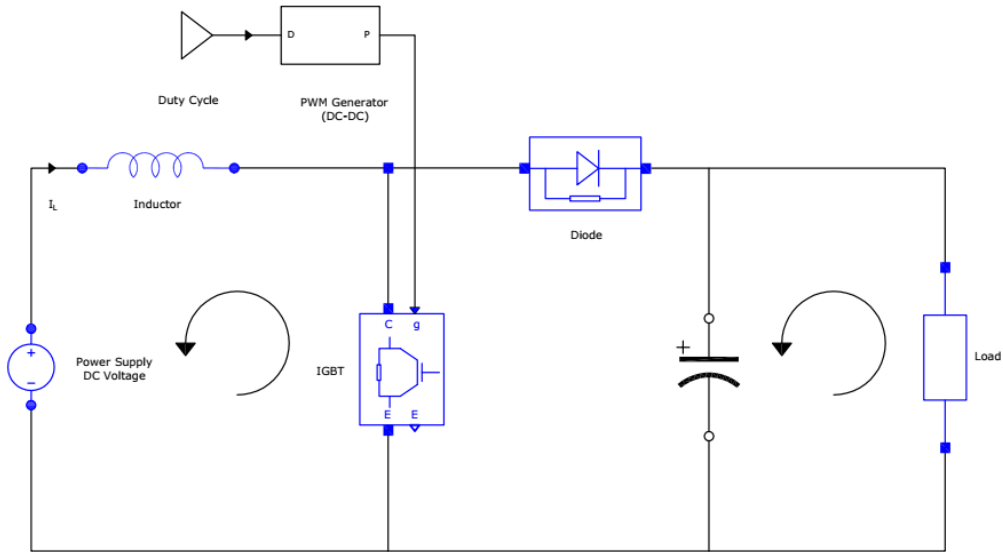
Figure 24 equivalent circuit of an MPP Tracker involving a boost converter, which is adjusted by the PWM Generator

Applied voltage to the load can be adjusted by the opening frequency of the IGBT's Mosfet, which is around 10 kHz and can be controlled via the duty-cycle value (δ):

$$\delta = \frac{TM_{on}}{T_S} \qquad\qquad \textit{Equation 14}$$

TM$_{on}$ is the period that the Mosfet switch is off, and the T$_s$ is the total switching time. During the off time, the inductance L will be charged, and when the Mosfet is on, the inductance will be discharged. In this case, the capacitor will be loaded, which acts as a voltage stabilizer. The voltage fluctuation can be calculated by eq. 15 and eq. 16. As shown, the duty-cycle value can control the voltage and its fluctuations.

$$\Delta I_L = \frac{V_0}{L} * T_{on} = -\frac{V_0 - V_c}{L} * (T - T_{on}) \qquad\qquad \textit{Equation 15}$$

$$V_c = V_0 * \frac{1}{1 - \delta} \qquad\qquad \textit{Equation 16}$$

A 100 µF capacitor and a 1 mH inductance are assumed for the simulation. A "perturb and observe algorithm" is used to generate the optimum duty cycle, which continuously measures the power and voltage of PV array and adjusts the duty cycle to reach the maximum power point. The simulated blocks are depicted in fig. 94 and fig. 95 in Appendix 4. After the MPP tracker block, a chopper is added to protect the motor against overvoltage damages in the DC bus. A trade-off between time series steps, duty cycle constant value and capacity of the capacitor should be made to get optimum simulation result.

3.3. Frequency controller

The voltage and frequency of motors should be adjusted to control the power consumption. However, to have optimum motor performance, the magnetic flux density (U/f) should always be kept constant, which is vital for smooth torque behaviour.

For controlling the frequency of each motor, three IGBTs are used, which are controlled via a PWM generator. Each IGBT has three switches, each with a 120° phase shift to generate a 3-phase current for the motor. The phase-to-phase voltage between the strings can be calculated based on the voltage of the DC bus, which the MPP tracker generates:

$$V_{ph-ph} = V_{DC} * 0.5 * \frac{\sqrt{3}}{\sqrt{2}}$$

Equation 17

A PI controller is applied to smoothen the voltage curve. PI parameters can significantly change motor behaviour. Therefore, they should be defined precisely. Rapid changes in voltage make the motor unstable, and if the reaction of the PI controller is slow, it cannot follow the MPP tracker signal, and the whole simulation will be unstable. For the simulation, P is set to 0.0015, and the optimum value for I is 666.

3.4. Pump and motor

The MFD connects the PV panels to the motors and pumps. Therefore, the efficiency of the MFD should be considered in the simulation:

$$V_{motor}I_{motor} = \eta_{MFD}V_{module}I_{module}$$

Equation 18

A three-phase asynchronous motor and a positive displacement pump, commonly used in RO systems, are modelled for the simulation. Performance of motor and pump in nominal power is determined by using:

$$P_{elec.-motor} = I_R^2 \times R_r(1-s)/s$$

Equation 19

$$P_{mech.-motor} = M \times n_s = M \times n(1-s)$$

Equation 20

$$\tau_{motor} = (I_{motor} - I_0)/K_T$$

Equation 21

$$\tau_{pump} = 100\frac{\Delta pD}{2\pi} + c_dD\mu n + c_f\frac{D}{2\pi} + \Delta p + T_c$$

Equation 22

$$\omega = (V - R_{mo})K_m$$

Equation 23

Where slip (s) is the difference between stator circuit frequency and rotor circuit frequency, I_{motor} and V are the current and voltage of the motor, respectively. Since the motor and pump share the same shaft, the speed and torque of the motor and pump are identical. Where $\overline{7}$ is the angular velocity, V is the motor voltage, R_{mo} is the resistance of the motor, and K_m is the motor speed constant in *rev/Vs*. The feed water volumetric flow produced by the pump Q is related to the angular velocity of the motor:

$$Q = \frac{D\omega}{2\pi} - C_S \frac{D}{2\pi} \frac{\Delta p}{\mu} - Q_R \qquad \qquad Equation\ 24$$

Where D is the pump volumetric displacement per revolution, C_s is the pump slip coefficient, μ is the dynamic viscosity of the water, Δp is the pressure difference across the pump, and Q_R is the flow loss due to inlet flow restriction. For part load conditions, affinity laws could be used to calculate pump performance. Based on the affinity laws, the flowrate changes linearly with speed, while pressure is a function of the square of the speed. The power consumption is proportional to the cube of the speed. This is very important because it causes a high sensitivity of power on the motor speed. For instance, the power required to operate the pump at 80% speed is half the rated power:

$$\frac{Q_2}{Q_1} = \frac{N_2}{N_1} \qquad \qquad Equation\ 25$$

$$\frac{P_2}{P_1} = \left(\frac{N_2}{N_1}\right)^2 \qquad \qquad Equation\ 26$$

$$\frac{HP_2}{HP_1} = \left(\frac{N_2}{N_1}\right)^3 \qquad \qquad Equation\ 27$$

Data from a 4 kW induction motor is used to model the motor, which can be found in fig. 96 in Appendix 4. The parameters of the motor and pumps are shown in table 7.

3.5. Reverse osmosis membrane

To simulate the water separation in the RO systems, the solution-diffusion model, developed by Merten and Lonsdale, is widely used in the literature[92,93]. In the proposed solution-diffusion mechanism, salt transport and separation occur due to the concentration gradient of the feedwater in the pressure vessel. Feed pressure and salt retention are two necessary parameters to define the performance of a RO system. A mass balance equation can be used to calculate the permeate flow Q. Ideal thermodynamic behaviour is assumed for the

simulation. However, in the real case, operation conditions and feedwater composition can create thermodynamic non-ideality on the salt transport mechanism, which is not considered in this simulation[94,95].

$$Q_F C_F = Q_C C_b + Q_P C_p \qquad \qquad \text{Equation 28}$$

Q_F, Q_C and Q_p are the feed, brine and permeate flux in L s^{-1}, respectively. C_f is the average feed concentration, C_p is the permeate concentration, and C_b is the salt concentration in the exiting brine. RO is not a perfect process, therefore always, some salt penetrates through the membrane to the product water. Assuming that the salt-water mixture is incompressible, eq. 28 could be simplified to:

$$Q_F = Q_C + Q_P \qquad \qquad \text{Equation 29}$$

The volumetric flowrate of produced water is also proportional to the membrane-wetted surface, the hydrodynamics of the system, and transmembrane pressure (TMP):

$$Q_p = AS_E (TCF)(FF)(\Delta\bar{P} - \Delta\bar{\pi}) \qquad \qquad \text{Equation 30}$$

$$TCF = exp\left(2640 * \left(\frac{1}{298} - \frac{1}{273+T}\right)\right); T \geq 25°C$$

$$TCF = exp\left(3020 * \left(\frac{1}{298} - \frac{1}{273+T}\right)\right); T \leq 25°C \qquad \qquad \text{Equation 31}$$

where S_E is the membrane surface area, A is the membrane permeability for water at 25 °C, TCF is the temperature correction factor of the membrane, FF is the membrane fouling factor, $\Delta\bar{P}$ is the average pressure applied across the membrane. $\Delta\bar{\pi}$ is the average osmotic pressure applied across the membrane, which is defined based on the van't Hoff equation[96] (see equation 32). In order to determine the fouling and temperature correction factors, the empirical relations and the design equations of DOW Filmtec SW30-2540 are used:

$$\pi = \sum \frac{iC_i RT}{M_i} = \sum iC_i RT \qquad \qquad \text{Equation 32}$$

$$\Delta\bar{P} = P_H - \frac{\Delta P_{fc}}{2} - P_P \qquad \qquad \text{Equation 33}$$

Where i is the van't Hoff factor[97], R is the ideal gas constant, P_H is the feed pressure, P_p is the pressure of the product water, M is the molecular weight of NaCl, and ΔP_{fc} is the pressure drop on the concentrate side:

$$\Delta P_{fc} = 0.756 \left(\frac{Q_C + Q_F}{2}\right)^{1.7} \qquad \qquad \text{Equation 34}$$

The brine pressure can also be defined via ΔP_{fc}:

$$P_c = P_H - \Delta P_{fc}$$
<div align="right">Equation 35</div>

$\Delta\bar{\pi}$ is calculated using the osmotic pressures:

$$\Delta\bar{\pi} = (pf)\frac{\pi_f - \pi_b}{2} - \pi_p$$
<div align="right">Equation 36</div>

Where pf is the concentration polarization factor, π_f is the osmotic pressure of the feed, π_b is the osmotic pressure of the brine, and π_p is the osmotic pressure of the freshwater. The osmotic pressure is calculated according to the ASTM Standards [98], and the polarization factor is also estimated based on DOW Filmtec SW30-2540. The salinity of permeate (C_p), concentration polarisation (CP), and salt flux (J_s mol m^{-2} h^{-1}) are calculated by[99]:

$$C_P = \frac{BS_E(pf)(TCF)C_{fc}}{Q_P}$$
<div align="right">Equation 37</div>

$$CP = \frac{C_{S0}}{C_f} = \left(1 - \frac{C_{fc}}{100}\right) + \frac{C_{fc}}{100} e^{\frac{J_v}{km}} = 1 + \frac{C_{fc}}{100}\left(e^{\frac{J_v}{km}} - 1\right)$$
<div align="right">Equation 38</div>

$$J_s = \frac{D_s^m}{x}(C_{S0}^m - C_{Sx}^m)$$
<div align="right">Equation 39</div>

Where B is the salt permeability of the membrane, x is membrane diameter, D_s is the coefficient of salt diffusion, C_f is solute concentration of feedwater, J_v is permeate volumetric flux (m/s), K_m is the mass transfer coefficient (m/s), and C_{s0}, C_{sx} are the salinity on the surface and permeate side. C_{fc} is the average concentration of the water on the concentrate (i.e., retentate) side of the membrane, given by:

$$C_{fc} = \frac{C_f + C_b}{2}$$
<div align="right">Equation 40</div>

For the simulation, eight membranes in series are modelled, and the Simulink subsystem is illustrated in fig. 97 in Appendix 4. The recovery ratio of eight membranes can be calculated via eq. 41 and other parameters are mentioned in table 7.

$$R = 1 - \sum_{i=1}^{8}(1 - R_i)$$
<div align="right">Equation 41</div>

3.6. Simulation model

Matlab/Simulink® is used to solve the nonlinear quasi-static equations 4 - 41. The block diagram of the model is shown in Fig. 25. Time series is set at 1.5 ms, a shorter period could theoretically enhance the results, especially in the MMP Tracker block, as it can find the

maximum power point faster. However, on the other hand, it leads to higher processing time, and more noise will also be created.
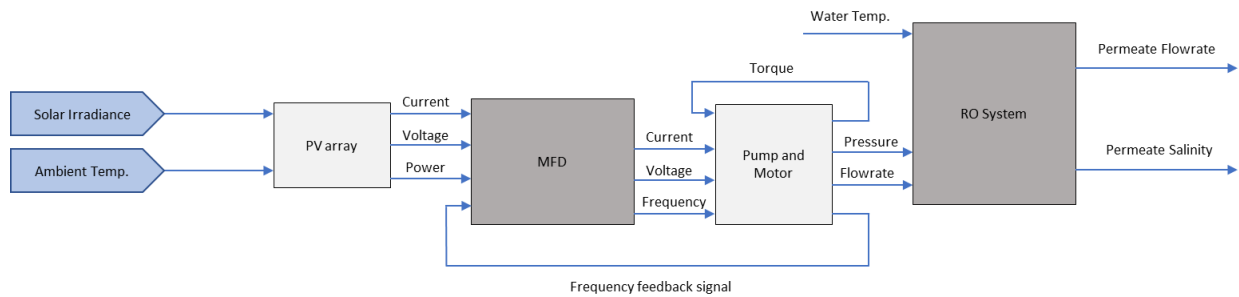

Figure 25 Block diagram of PVRO with variable speed pump, which is used for the simulation.

All parameters should be precisely calculated for the Simulink blocks to have an accurate simulation. The parameters are listed in table 7, and the performance of the developed system is compared with a fixed-speed conventional system. The simulation is performed for two different ambient conditions. The weather data of Lamu in Kenya as a sample installation location is used to run the simulation. Fig. 26 illustrates the dispersity of the solar irradiance at two different months of the year in Lamu. Furthermore, four different values for the maximum pump pressure are applied to investigate and compare the behaviour of the systems in a wide range. The maximum working pressure of the pump depends on the feed water salinity. Therefore, the provided results can cover a wide range of feedwater quality. However, first simulation is run for a short step time (10 seconds) to optimise the simulation parameters. Fig. 27 depicts the simulated ambient conditions used for the short-time simulation. Both ambient temperature and solar irradiance are variable, the changes are entirely random, and the only purpose is to investigate the model's behaviour. These values are used as the input parameters of the PV subsystem, including 18 panels in series, and the sampling time is set at 1.5 ms. The most important output values are shown in fig. 27. In the first 300 ms, PV power is used to charge the capacitor. Afterwards, the capacitor voltage will be fixed at 700 VDC, as it has reached the maximum capacity. During this period, the duty cycle reduces to about 0.09 to increase the voltage and power of the PV system. Then the duty cycle increases to about 0.2 to decrease the PV voltage. This process takes around 200 ms, which is fast enough, and on the other side, the changes in the capacitor voltage are pretty smooth. During the whole simulation (10 seconds), the perturb and observe algorithm searches the optimum value of the duty cycle and sets a new value every 1.5 ms, which leads to minor fluctuations in the duty cycle graph.
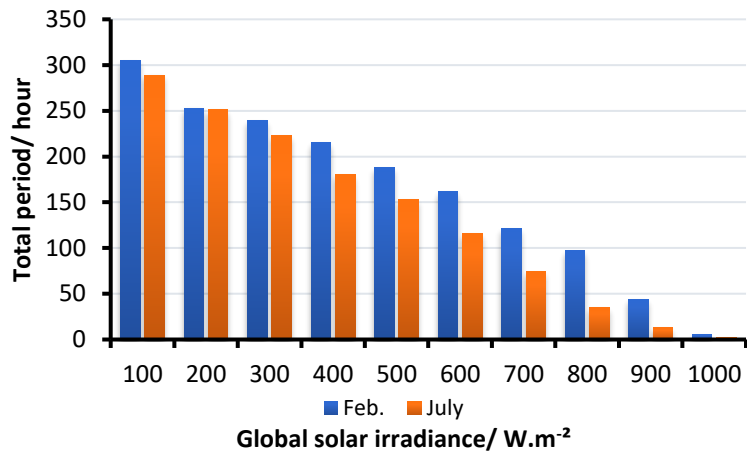
43

Figure 26 Solar irradiance histogram of two different months in Lamu, Kenya. July is a rainy and cloudy month and high irradiance days rarely happen compared to February.

However, it creates instability neither for PV power nor for the capacitor. Despite the fast and broad changes in the temperature and irradiance, to control the voltage and power of the PV array, the duty cycle only changes between 0.09 and 0.23. Therefore, it proves that all parameters which are set for the MPP Tracker are aligned with each other.
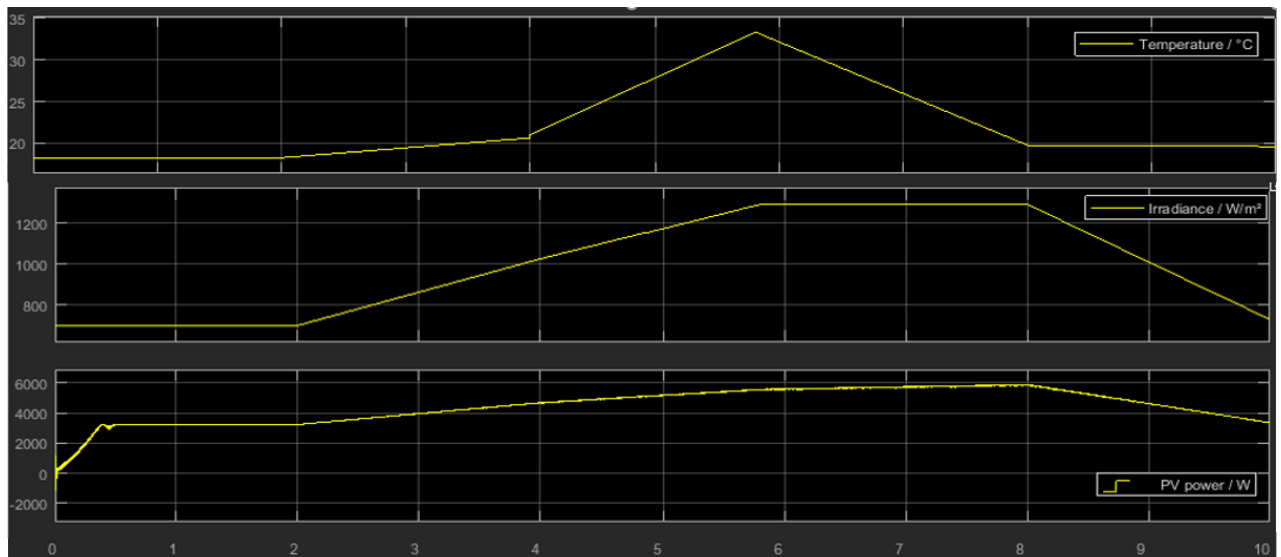
Figure 27 random changes in ambient temperature and solar irradiance to test the behaviour of the simulated model in a short period.

44
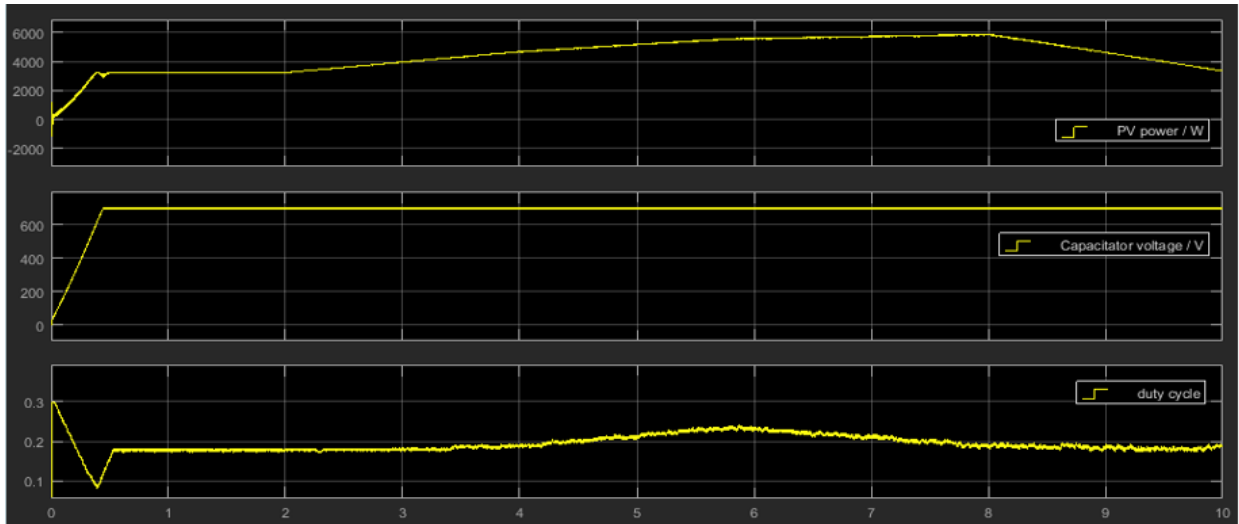
Figure 28 the behaviour of the MPP Tracker is shown under fast changes of the input values (see fig. 26). The perturb and observe algorithm sets a new value for the duty every 1.5 ms. There is no overshoot or significant fluctuation in PV power and capacitator voltage.

The same investigation is performed for the pump and motor subsystems to try out the implemented model and parameters. The input values of the motor subsystem, including voltage, frequency and connected load, are set manually solely to study the behaviour of the model under controlled changes. The 10-sec test scenario involves different steps:

- 0 to 2 seconds: no load is connected; the goal is to observe the performance of the motor under idle conditions.
- 2 to 5 seconds: pump is connected to study the behaviour of the motor with a fixed frequency (50 Hz)
- 5 to 10 seconds: frequency jumps from 50 Hz to 70 Hz by using a step signal to investigate the fast change of speed, especially out of the operating range.

The results are shown in fig. 28, the motor exactly runs at synchronous speed, i.e., 3000 rpm, during the first two seconds. After connecting the pump, the slip slightly increases to about 2%. According to the manufacturer data, the motor speed at such slip value should be around 2940 rpm. The simulation value is insignificantly lower; the value on the graph is about 2920 rpm.

45
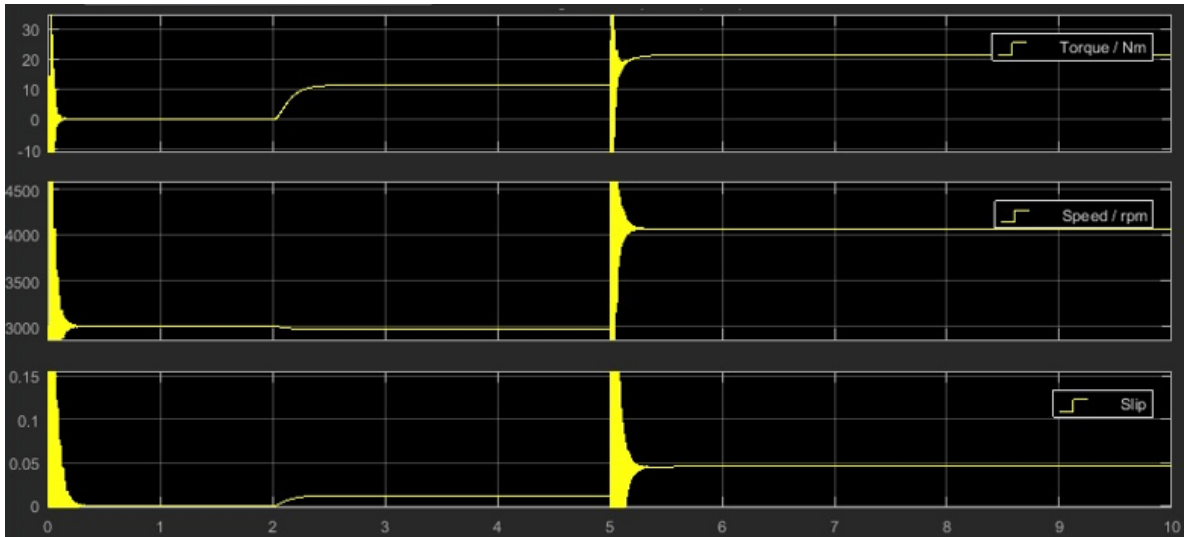
Figure 29 the performance of the motor subsystem under controlled conditions. Although there are some deviations and fluctuations, the model behaviour is acceptable.

The sharp change (step signal) in the frequency causes some instabilities in the model. However, it lasts only a few milliseconds, as shown in fig. 30, the motor current is relatively stable afterwards, and the model can immediately control such a fast change.
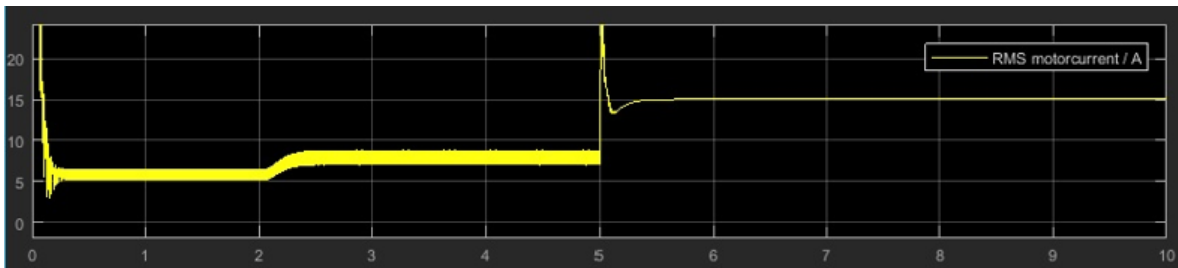

Figure 30 behaviour of motor current under fast frequency change.

The pump's values are proportional to the values of the motor. As the motor has smooth performance, stable behaviour in the pump is correspondingly expected. The graphs of the pump flux and pressure are shown in fig. 31.

As mentioned above, between 2 and 5 seconds, the motor and pump run with nominal power. In this phase, the values are matched with the manufacturer data, i.e., the nominal flow rate is 4700 lit/h, while the simulation value is 4850 lit/h. Therefore, the deviation is about 3%, which proves that implemented parameters are accurate enough.
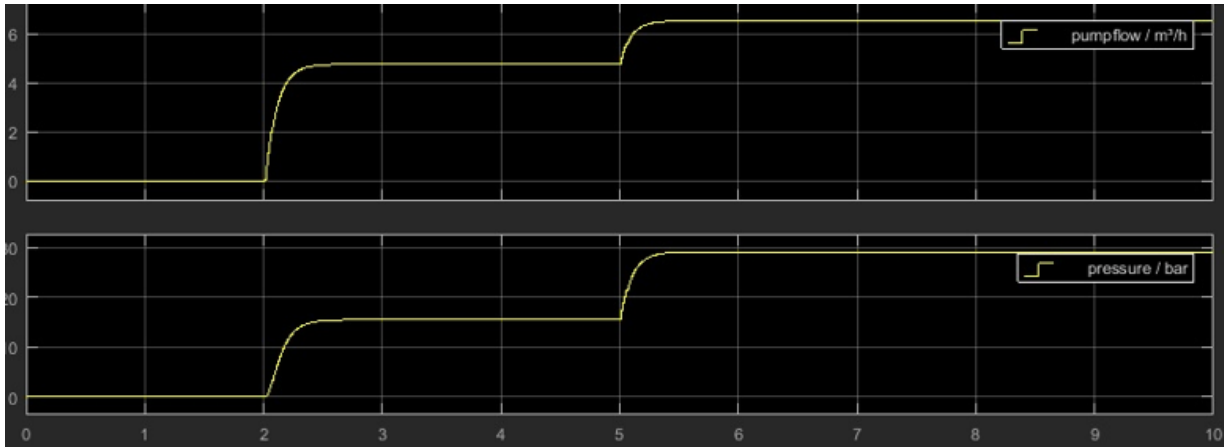
Figure 31 motor and pump share the same shaft. Consequently, the performance of the pump depends on the motor's behaviour. The graphs show that both motor and pump have a smooth operation attitude.

As the last subsystem, the membranes should be checked by a controlled scenario before applying the real data to investigate the model's performance. Values of the Filmtec Membranes from Dupont are used to validate the simulation. The system's performance with constant input values is also simulated in the test phase. WAVE[6] software (from Dupont) is used to simulate the system with constant values.

It is necessary to access the temporal variation of solar irradiance to enhance the accuracy of the investigation, especially the membrane performance. Meteorological data from Lamu in Kenya is used to study the simulated system's performance and compare it with conventional fixed-speed water desalination. Fig. 26 illustrates the dispersity of the solar irradiance at two different months of the year in Lamu, and fig. 32 depicts the daily maximum continuous operating period of the system for February. While the developed technology can operate continuously for at least 5 hours per day, the fixed-speed system works continuously for only four days for more than 4 hours in February. Fig. 33 illustrates pump pressure for two different days; a mostly sunny day and a day with high cloud coverage. Table 8 compares the system performance for fixed and variable speed pumps in different climate conditions and pump pressures. The table summarises all simulation results and shows that the developed technology yields higher working hours and water production.

For instance, for the pump with a maximum pressure of 69 bar, working hours are increased by 4 and 5 hours for sunny and cloudy days, respectively. In addition, permeate flow is

---

[6] https://www.dupont.com/water/resources/design-software.html

increased by about 34 % for the sunny day scenario. Furthermore, water production increased significantly for the cloudy condition (permeate flow is 2.4 times higher).

Table 6. simulation parameters are extracted from manufacturer data.

Membrane		Pump & Motor	
Water permeability, A	$3.111×10^{-4}\ L/m^2.bar.s$	Pump coefficient of viscous drag, c_d	$3.803×10^{-4}\ N\text{-}m/bar\text{-}L$
Salt permeability, B	$1.9481×10^{-5}\ L/m^2.s$	Pump friction coefficient, c_f	$4.033\ N\text{-}m/bar\text{-}L$
Total area, S_E	$2.8\ m^2$	Pump slip coefficient, c_s	$3.361×10^{-10}$
Feed water TDS	$4000\ ppm$	Pump volumetric displacement, D	$2.60×10^{-3}\ L/rev$
Solar Panel		Motor friction-related current, I_0	$0.65\ A$
Surface area, Ac	$1.489×10^{-3}$	Motor torque constant, K_T	$2.252\ A/N\text{-}m$
Light current constant, C_0	$3.318\ A/W$	Motor speed constant, K_V	$1.824\ rev/V\text{-}s$
Light current temp. constant, C_1	$2.525×10^{-3}\ A/W\text{-}K$	Stator resistance, Rs	$0.252\ \Omega$
NOCT	$45℃$	Stator inductance, Lls	$2×10^{-3}\ H$
Number of cells in each string, n_{cell}	72	Rotor resistance, Rs	$0.502\ \Omega$
Number of cells in each parallel, n_{string}	1	Nominal flowrate, Q_f	$4.8\ m^3/h$
series resistance, R_s	$1.911×10^{-3}\ \Omega$	Nominal Pressure, P_f	$15\ bar$
shunt resistance, R_{sh}	$1296\ \Omega$	Shaft power, $P_{elec.}$	$3.4\ kW$
MPP Tracker		Efficiency, $\eta_{mech.}$	57%
Inductor value, initial current	$0.001\ H,\ 15\ A$	Motor torque	$11.24\ Nm$
Capacitator	$100\ \mu F$	PI controller, P value	0.0015
Sample Time	$0.2\ mS$	PI controller, I value	666

As a negative consequence, the average salinity of produced water in the developed technology is higher and varies during the day but still within the thresholds for drinking water, i.e., 500 ppm[100] (see table 7).

Table 7 System performance in different pump pressures and weather conditions.

Pump max. Pressure (bar)		Sunny day			Cloudy Condition		
		Working hours (h)	Ave. output salinity (ppm)	Produced Water (lit/day)	Working hours (h)	Ave. output salinity (ppm)	Produced Water (lit/day)
69	Fixed speed pump	5	60	1300	2	60	520
	Variable speed pump	9	110	1745	7	94	1279
60	Fixed speed pump	5	83	936	2	83	374
	Variable speed pump	7	100	1150	7	156	840
50	Fixed speed pump	5	146	532	2	193	213
	Variable speed pump	7	221	613	6	395	359
45	Fixed speed pump	5	236	330	2	236	132
	Variable speed pump	6	324	342	2	236	132

The salt concentration is also higher because crossflow velocity on the membrane is a function of the solar irradiance. When PV power is low, water flow reduces. Under this circumstance, the thickness of the boundary layer on the membrane surface and, subsequently, the accumulation of retained salts will increase. Hence, due to the high salt diffusion, more salt can penetrate through the membrane to the product water (at constant pressure).

This is crucial to designing a system that consistently produces water fulfilling the World Health Organization (WHO) guidelines. However, a consistent quantity of water is essential as well. The maximum salinity difference in the developed system is about 200 ppm. As shown, the developed technology has more continuous working hours (see fig. 32). In contrast, fixed speed systems only work in a narrow range of solar irradiation (between 600 and 1000 W m^{-2}). The solar energy difference between summer and winter is about 45 % in this range. In comparison, the developed system can utilize a broader insolation range, i.e., above 300 W.m^{-2}. In this range, seasonal energy variation is just 25 %. Therefore, water production is steadier during the year.
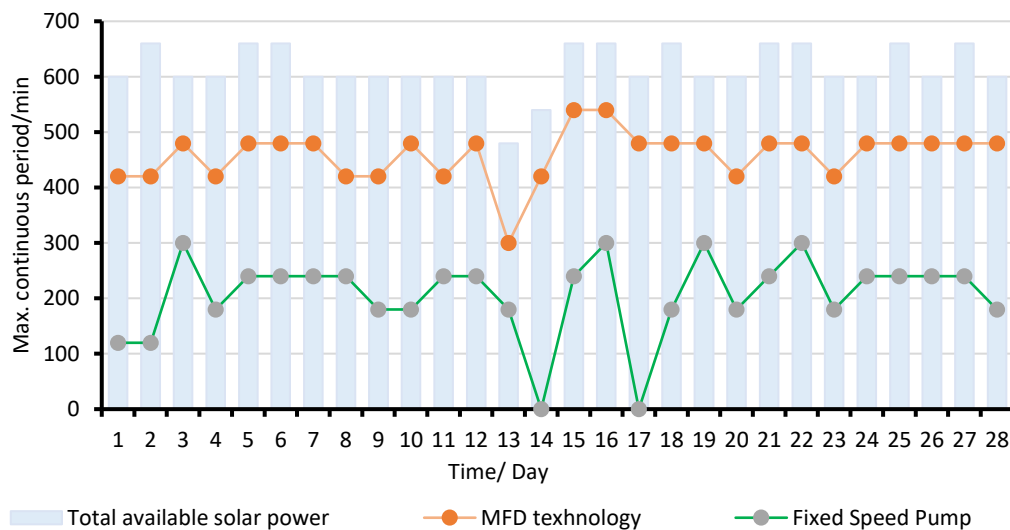
Figure 32 the temporal variation of solar irradiance defines the continuous working period of the system. The working time (min/day) of the developed system is compared with a fixed-speed pump.
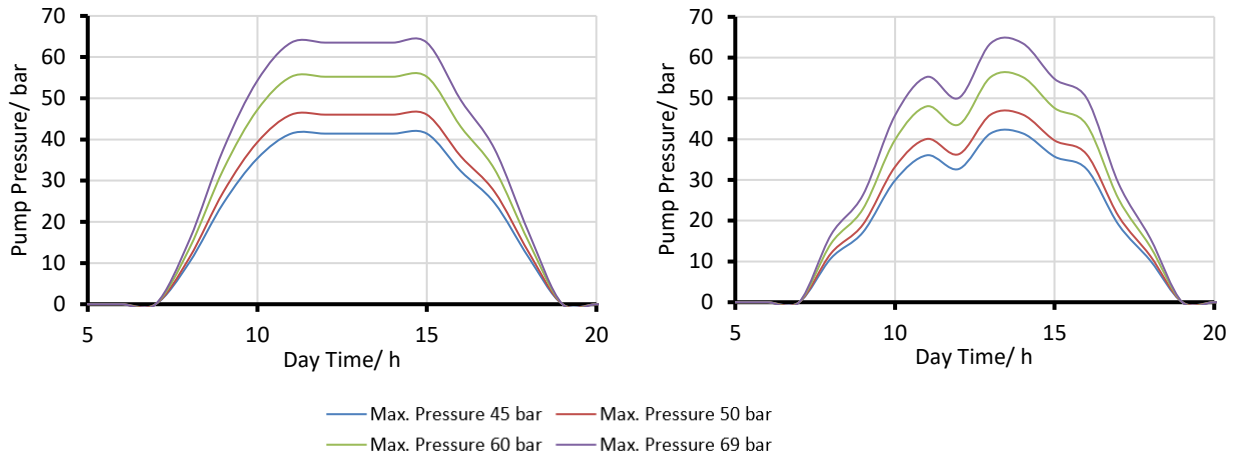
Figure 33 performance of the developed system under different pump pressure for two distinct days; left: a mostly sunny day, right: a day with high cloud coverage.
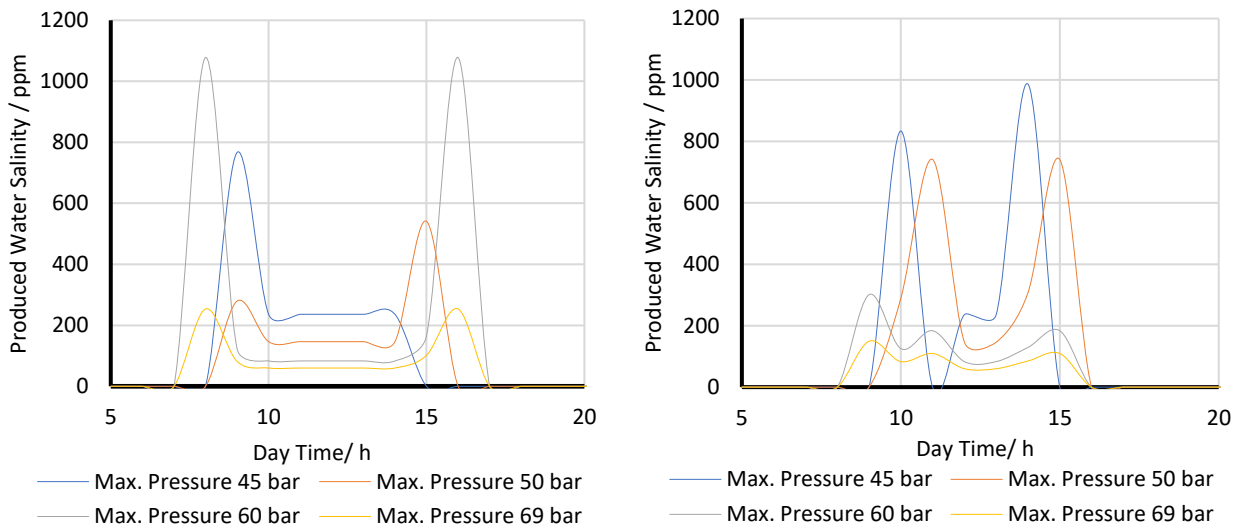
Figure 34 salt concentration (TDS) of the produced water is calculated for different pump pressure under two distinct days; left: mostly sunny day, right: a day with high cloud coverage.

As shown in fig. 34, TDS value changes according to the available solar energy. Especially for cloudy weather conditions, there are more fluctuations in the TDS curve as MFD continuously changes the frequency of the pumps based on the available energy. Table 8 compares the TDS values of the produced water when the pump's maximum pressure is 60 bar.

Table 8 the salt concentration in the produced water for sunny and cloudy weather conditions while the maximum working pressure of the pump is 69 bar.

Daytime - h	08:00	09:00	10:00	11:00	12:00	13:00	14:00	15:00	16:00	average TDS
sunny day	253.53	81.87	59.86	59.86	59.86	59.86	59.86	101.72	253.53	**110.00**
Cloudy condition	0.00	149.44	83.00	109.46	59.86	59.86	85.01	109.46	0.00	**72.90**

50

Although the water quality is higher in each hour for the sunny weather condition, the average daily TDS is higher because the system can start to produce water one hour earlier in the morning and one hour later in the afternoon. As the solar radiation is low in these hours, the water quality would be less, i.e., TDS would be higher. Therefore, during sunny days more water can be produced; however, the average water quality is lower. Nevertheless, the water quality is always within the guidelines of WHO for drinking water.

Chapter 4

Lifecycle analysis (LCA) of the developed system

---

4. Lifecycle analysis (LCA) of the developed system

Since 1990, several investigations have been done to examine the qualitative and quantitative environmental incidences of desalination systems[101,102,103]. In 2021, Thi et al. comprehensively compared the environmental aspects of different desalination technologies, including MSF, MED, and RO. Various energy resources involving fossil fuels, gas-fired, wind, solar, and nuclear energy are also considered. All applied analysis methods show that RO has the lowest environmental impact[104]. Furthermore, RO generates less airborne emissions like non-methane volatile organic compounds (NMVOC), nitrogen oxides (NOx), and sulphur oxides (SOx)[105]. Particularly, integrating RO with renewable energy resources can significantly reduce CO_2 emissions.

Compared to the other assessment methods like, material flow analysis (MFA) or environmental risk assessment (ERA)[106], Life cycle Assessment (LCA) provides a systematic and objective approach to measure the environmental burdens of any product (or system) through its whole life cycle, from raw material extraction to final disposal and aids in choosing the least detrimental option[107,108].

In this thesis, LCA method has been applied to analysis the environmental impact of the developed technology. The LCA is based on "ISO 14044 Life cycle Assessment – Requirements and Guidelines", which includes a complete cradle-to-grave analysis. ISO 14044 was released in 1997 for the first time, and in 2006, a revised version was published[109].

The main goal of this section is to provide objective and comparative parameters to compare the environmental performance of the developed MFD technology and the conventional PVRO. This assessment is crucial because, despite being more affordable, membrane-based water purification systems still have a noticeable negative impact on the environment[110]. As described in chapter 2, the developed system does not need any energy storage system. Removing the batteries could remarkably reduce the negative environmental impacts, which can principally remove all debates and concerns of policymakers/stakeholders related to the sustainability of PVROs. Four preliminary investigations should be done to quantify the environmental impacts, which are explained below[111].

4.1. Methodology

4.1.1. Goals and Scope Definition

In this phase, the exact goal of the LCA assessment should be defined, which could be development, optimization, or comparison. In addition, system boundaries and cut-off criteria should be determined, which describe the necessary processes and negligible parameters accordingly. Function units (FU) will be used to quantify the environmental impacts, which also make it possible to have comparable values at the end of the investigation.

This LCA aims to compare the developed system with conventional PVRO. For both systems, seawater is considered as the feed water (principally seawater systems have about 48–58% higher environmental effects in the most impact categories due to the higher osmotic pressure[112,113]), Ghana is the installation location, and 15 years is assumed as the system lifetime. The system boundaries involve PV modules, conventional inverter, the balance of PV system (BOS), battery unit including charging and discharging elements, VFG, water pumps, piping system, membranes and water tanks. Other components have negligible influence on the total LCA[114]. The FU is based on the produced water, and the amount is 1 m³/day, while the real production rate is 2.3 m³/day and 2.8 m³/day for the developed system and the conventional system, respectively.

An efficient pre-treatment system can significantly enhance the performance and, subsequently, the LCA of RO plants, particularly in seawater systems[115]. Environmental performance of different pre-filtration units, including multimedia filter, sedimentation-based pre-treatment, and UF system are investigated in the literature [116,117,118]. However, as identical pre-treatment is assumed for both systems, the effect of this sub-system is eliminated in the comparison. For the same reason, this thesis does not investigate the effect of brine disposal. Furthermore, brine disposal is a site-specific issue as opposed to a process-specific problem and might consequently distort the comparison. The environmental burden of different brine disposal methods has been evaluated in several studies. However, gate-to-gate investigations reveal that the contribution of brine disposal to the overall LCA can range from 3.1% to 5.6%[119,120,121]. Therefore, the system boundary involves three main sub-systems, namely power unit (PV array), control system, and RO components.

4.1.2. Inventory Analysis

After defining the system boundaries, the input and output flow of the system should be identified and qualified. The input flow consists of the required energy and raw materials, while the output flow can include a wide range of variables such as solid waste, air or waterborne emissions, and any other environmental releases. Standard databases (Ecoinvent[7]) or LCA software like SimaPro[8] and GaBi[9] can be used to quantify the components' inventory.

In this work, for the PV modules, the inventory values of another research are used, and all hydraulic system components are modelled by GaBi software (education version), using Ecoinvent database as the impact assessment method. The output flows are brine flow and permeate at the end of the membranes. Since the system is solar-based and entirely off-grid, LCA is independent of national electricity-production-related issues.

4.1.3. Life Cycle Impact Assessment (LCIA)

In this phase, inventory values should be summed up in specific categories. For instance, all parameters contributing to emissions should be aggregated in one category and presented by one equivalent unit. For instance, for the global warming and acidification potential, all emission flows are converted to kg CO_2-eq and SO_2-eq, respectively, using an appropriate characterization factor.

There are two main approaches for impact assessment: midpoint and endpoint methods. When the focus is on problem identification, midpoint (problem-oriented) assessment technique is more potent and can provide more details[122,123]. While in the endpoint (damage-oriented) method, the focus is more on quantifying the damages[124]. EDIP, ReCiPe, and CML are mainly used methods for midpoint assessment and Eco-Indicator 99 (EI 99) is often applied for endpoint investigations[125,126,127].

In this thesis, CML, as the most frequent midpoint assessment method, is used because the primary goal of this analysis is to identify and quantify the problem using the cause-effect approach[128]. Although the CML baseline method covers a wide range of LCA categories, CED

---

[7] https://ecoinvent.org/the-ecoinvent-database/
[8] https://simapro.com/databases/
[9] https://sphera.com/product-sustainability-software/

(Cumulative Energy Demand) is not part of this assessment. As CED is an important indicator, it is calculated separately and added to the LCA results. Fig. 35 shows the items which are included in the LCA.
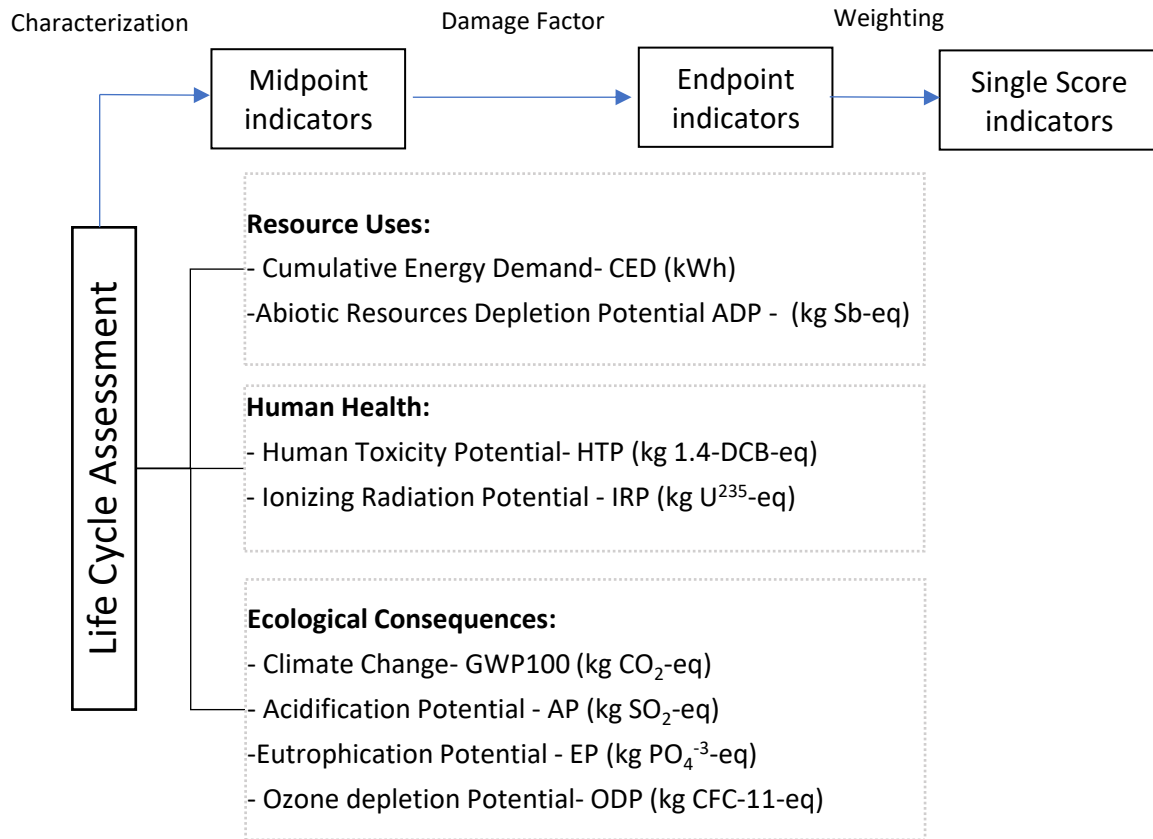
Figure 35 CML method, as a midpoint assessment method, is used in this thesis. The graph shows the studied impacts and the units. CED is also added to the categories and calculated separately to have a comprehensive assessment.

CED describes the total energy that is needed for the whole life cycle of a product or a service in kWh, ADP reflects how much non-biological resources are used in the process, including fossil fuels, minerals, metals, and water, which is measured based on kilograms antimony equivalents, GWP100 represents how the process contribute in global warming potential and producing greenhouse gases, based on IPCC values (Intergovernmental Panel on Climate Change), which is shown in kg CO_2 equivalent[129], ODP measures the damage of the process to the stratospheric ozone, and the unit is kg CFC-11 equivalents, AP reflects the acidic gases which are generated during the life cycle which is measured in kg SO_2 equivalents, EP shows the amount of toxic chemicals that are released by producing the goods in kg 1,4-DCB equivalents, IRP describes the damages through the radionuclides which are released during the process and its unit is kg of uranium-235.

In the end, using Normalization/Weighting, Single Score Indicators can be calculated, providing a better opportunity to interpret the results and consequences[130]. Other impact categories, weighting less than 1% of the overall result (cut-off criteria), like impacts on the marine environment, noise, ecotoxicity, and human toxicity of metals, are neglected and not considered in this work.

4.1.4. Interpretation

In this phase, all assumptions, simplifications, and restrictions of LCA for the operational phase are determined and calculated based on "cradle-to-grave" analysis, which can reduce assessment uncertainties[131,132]. Different methods can be applied to analyse the data and identify the environmental hotspots. The main goals of this step are to define potential improvement opportunities, give credibility to the LCA, and eliminate any prejudice[133]. One of the best approaches is TOPSIS (Technique for Order Preference by Similarity to the Ideal Solution), which is a multi-criteria decision analysis (MCDA) method[134]. For this analysis, a normalized decision matrix should be generated:

$$n_{ij} = \frac{x_{ij}}{\sqrt{\sum_{i=1}^{m} x_{ij}^2}} \quad i = 1,2, \dots m \, ; j = 1,2, \dots n \qquad \text{Equation 42}$$

x_{ij} is the i-alternative value based on the j-criterion. Based on the normalized values, a weighted normalized decision matrix should be calculated:

$$v_{ij = w_j n_{ij}} \quad i = 1,2, \dots m \, ; j = 1,2, \dots n \; \sum_{j=1}^{n} w_j = 1 \qquad \text{Equation 43}$$

R-value can ultimately measure how closely the outcomes match the ideal solution:

$$R_i = \frac{d_i^-}{d_i^- + d_i^+} \quad i = 1, 2, \dots m$$

$$d_i^+ = \sqrt{\sum_{j=1}^{n} (v_{ij} - v_j^+)^2} \; i = 1, 2, \dots m$$

$$d_i^- = \sqrt{\sum_{j=1}^{n} (v_{ij} - v_j^-)^2} \; i = 1, 2, \dots m \qquad \text{Equation 44}$$

v^+ is the maximum value of the benefit criteria and the minimum value of the cost criteria, v^- is maximum value of the cost criteria and the minimum value of the benefit criteria. The R-value is between 0 and 1.

4.2. Life cycle inventory (LCI)

This section describes all steps of calculating the LCI and impact categories, including assumptions and simplification. The accuracy of LCA significantly depends on the exactness of the LCI and the quantitative database of the material and energy flows. Thus, the quality of the LCA can never be higher than the quality of the underlying LCI data[135].

As shown in fig. 36, for each component, the whole lifecycle procedure is considered to identify the environmental hotspots. However, studies indicate that in the majority of the impact categories, the application phase has the biggest impact [136,137]. Operation and Maintenance (O&M) are the two primary activities that contribute to the LCA of the application phase. Nevertheless, as the latter has a negligible effect on the result[138], the operation is mainly investigated for this phase. Technique-defined and material-defined approaches are applied to choose appropriate datasets.

Regarding the transportation phase, it is assumed that all components should be delivered to Germany (production location), and then the complete system should be transported to Ghana (installation location). However, Li et al. demonstrated that increasing material transportation by 30% only results in a 1.4% rise in LCA[139]. The same investigation by Shahabi et al. even shows less effect as a 50% increment in transportation routes led to a 0.96% rise in GHG emissions[140].
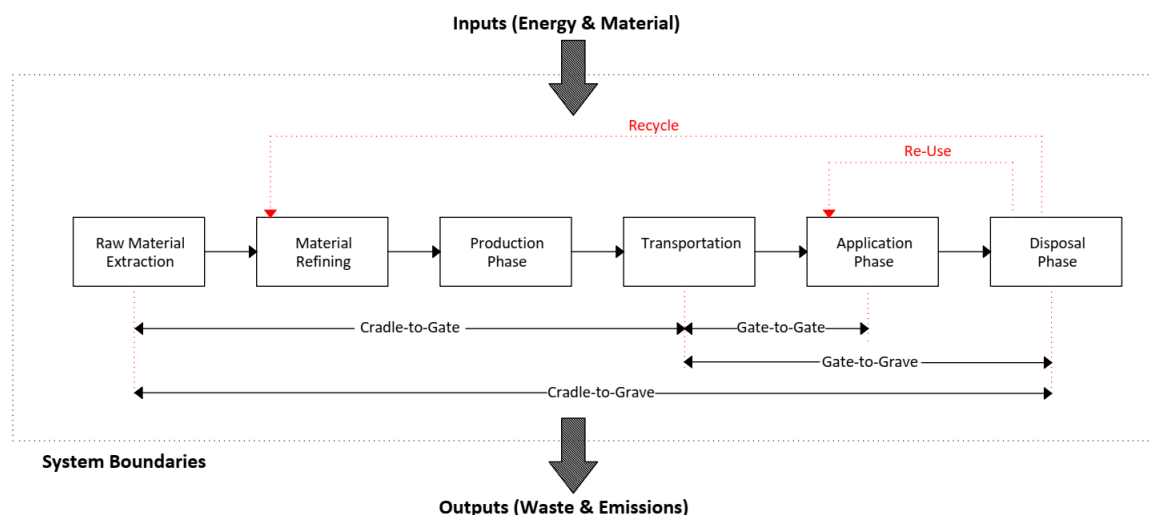
Figure 36 CML baseline is applied for lifecycle assessment which is a cradle-to-grave approach, and all lifecycle phases of each component are considered.

4.2.1. PV modules

The Lifecycle of PV modules is very complex and consisting different phases. In this work, data from another research work is used [141]. This reference is selected as ISO guidelines (Ecoinvent database) are used for the LCA. However, some units were different, which are converted to the correct units, using appropriate characterisation and normalisation factors [142,143]. Furthermore, some physical properties of the investigated PV modules, like wafer thickness and efficiency, were partially matched with the panels used and installed for the pilot project in Cape Coast. Thus, these parameters are also changed to the actual values.

Manufacturer data of a German company, Mastervolt is used for investigating the inverter. The lifetime of the inverter is 15 years, while the lifetime of PV panels is 30 years estimated. The lifetime of the RO is also 15 years. Therefore, 15 years is used as the base of the calculations. The same LCA values are considered for the VFG. Although VFG has fewer components than a conventional inverter, the difference in LCA is assumed to be negligible. It is also assumed that the whole PV array is sent from Europe to Ghana.

4.2.2. Battery unit

Cusenza et al. have investigated the LCA of the lithium-ion battery, including charging and discharging units for hybrid electrical vehicles EV based on ISO 14040 [144]. All LCA values are multiplied by three as the expected battery lifetime is five years. In addition, the power capacity is adjusted to 10 kWh according to the RO and PV capacity.

To keep the batteries in optimum operation condition, the charging and discharging unit should be installed with the batteries to protect the unit against overvoltage and low voltage operation. As the function and components of this unit are almost the same in all applications, the values from the literature are applied to this work as well.

4.2.3. Water desalination (RO) system

Although the components of the RO unit are less complex compared to the solar system, to consider all details and to have more accurate values, most of the inventories are collected from other references [145,146]. Pumps, high-pressure, and low-pressure pipes are considered in the LCA based on the system design (see chapter 3). All lifecycle phases, as shown in fig. 36,

are considered. Furthermore, it is assumed that the system will be shipped from Germany to Ghana, the system lifetime is 15 years, and the landfill is the disposal method.

Membranes have a shorter lifetime, about three years, which is also considered in the assessment. There is no inventory for the seawater membranes however, according to the manufacturer data[10], the structure is very similar to the brackish water membranes, and this kind of membrane is assumed in this work. In addition, it is assumed that the pressure vessel is built from polypropylene (PP), while based on the manufacturer data, fibreglass-reinforced plastic (FRP) is the correct material. However, as GaBi software has no database for the FRP, PP is used in this work because it has the closest material properties[147]. The lifetime of the pressure vessels is 15 years, and the manufacturer is located in South Korea, which is considered in both energy emission and transport. Two water tanks, each 6 m^3, are considered in the LCA, the lifetime is 15 years, and high-density polyethene is selected as the material.

4.3. Results

In this chapter, all values regarding the LCA will be presented. Some simplifications are considered in the assessment. As the final goal is to compare the two technologies, the simplifications are identical for both cases.

The water production capacity of the system per day is selected as the function unit for all impact categories to make them comparable. Fig. 37 shows the relative values of each inventory for a conventional system and the developed technology. Fig. 38 compares and visualizes the impact of removing batteries on the LCA. All categories are normalized to 100%, and the following section provides an explanation of the parameters and interpretation of results.

---

[10] *Filmtec XLE-2540 membrane.* Retrieved July 10, 2019, from https://www.lenn tech.com/Data-sheets/Dow-Filmtec-XLE-2540.pdf
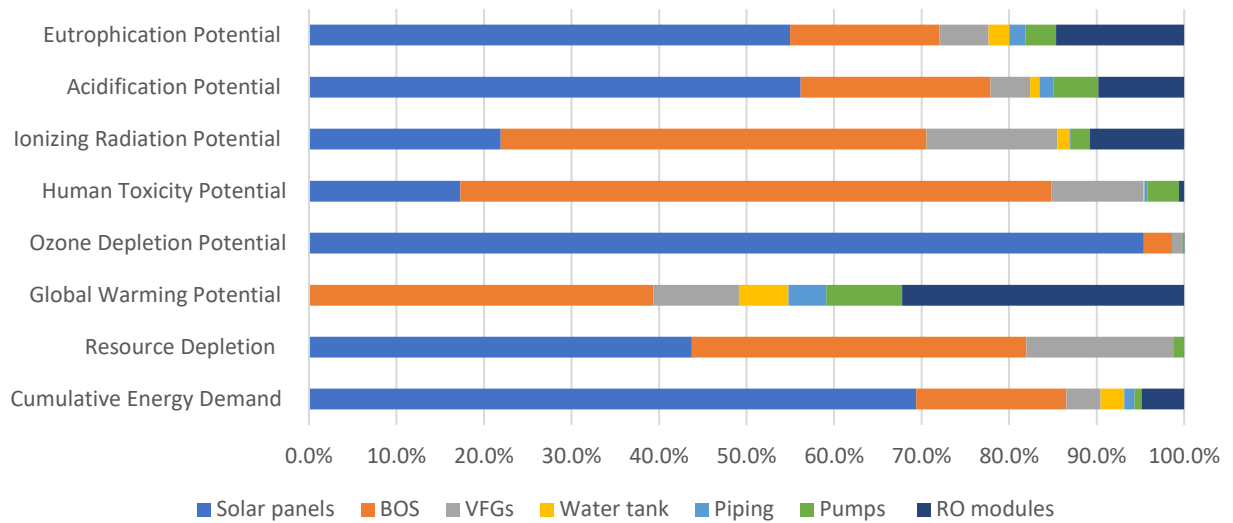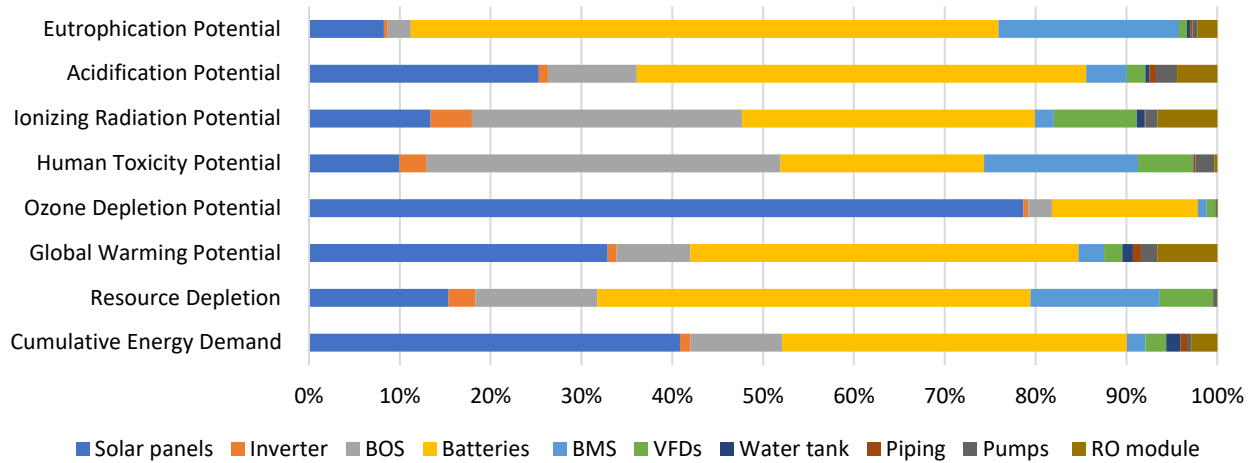
Figure 37 relative LCA values for: Top. conventional PVRO system including batteries, Bottom: developed MFD technology. The conventional system consists of more equipment, while using MFD technology can remove batteries and the battery management system.
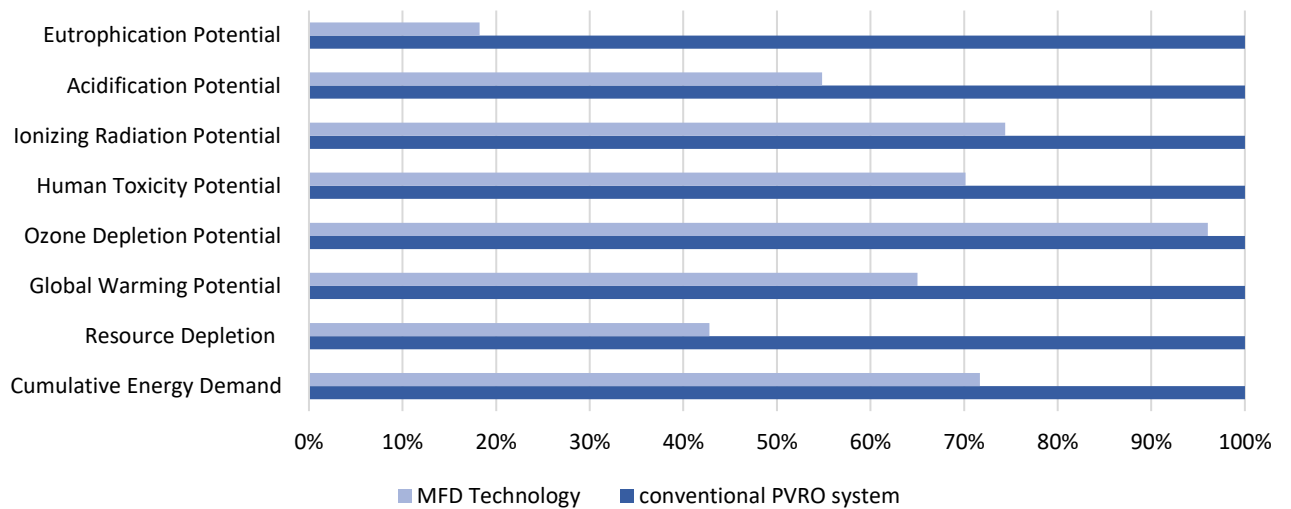
Figure 38 LCA comparison between MFD technology and a conventional system.

a- Cumulative energy demand (CED)

CED is a metric to measure the overall energy inputs (directly and indirectly) required throughout the entire life cycle. CED aids in determining the most energy-intensive stages and in evaluating the possibilities for energy savings and reducing the environmental burdens of the product. PV panels, BOS and batteries are mainly contributed in the CED of the PVRO systems, and among the lifecycle, the production phase had the highest value as the system does not need any external energy source during the operation phase. For instance, producing the battery cells causes 80% of the whole CED of the battery lifecycle and all other steps like transportation, application, and disposal from 20% of CED.

Considering the entire PVRO system, batteries account for more than 25% of the total CED. Therefore, removing the batteries leads to a significant and direct reduction of CED (see fig. 39.)
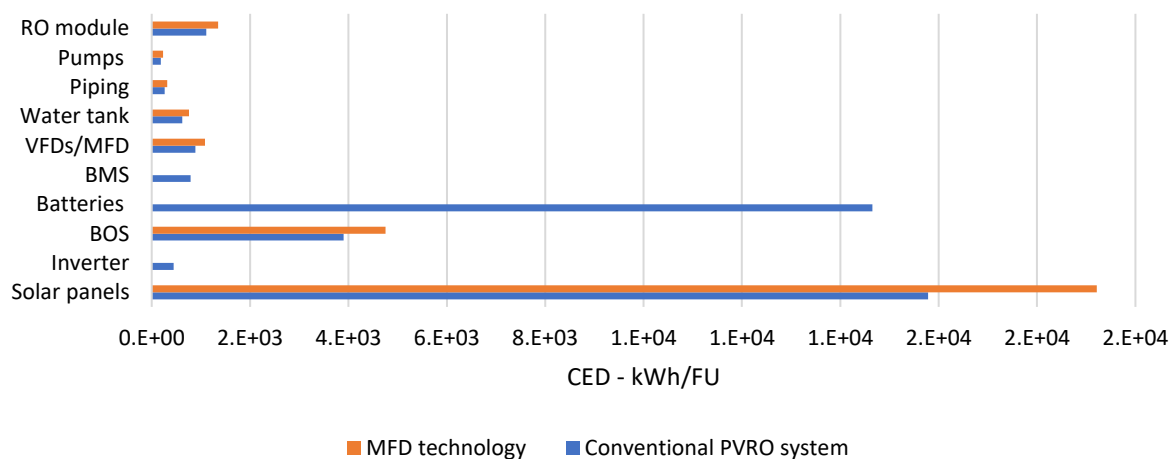
Figure 39 comparing the Cumulative energy demand (CED) for a conventional system and MFD technology.

b- Abiotic resource depletion

The amount of non-renewable resources, such as minerals, metals, and fossil fuels, used by a product or process is measured by the concept of abiotic resource depletion. Therefore, it is a critical aspect of LCA as it reveals the resource depletion potential and the necessity of resource conservation. Rare elements such as cobalt, lithium, and manganese are needed to produce battery and BOS. These two elements share more than 60% of the total resource depletion in PVRO systems. The values are shown in fig. 40, which proves that MFD technology removes more than 50% of the resource depletion.
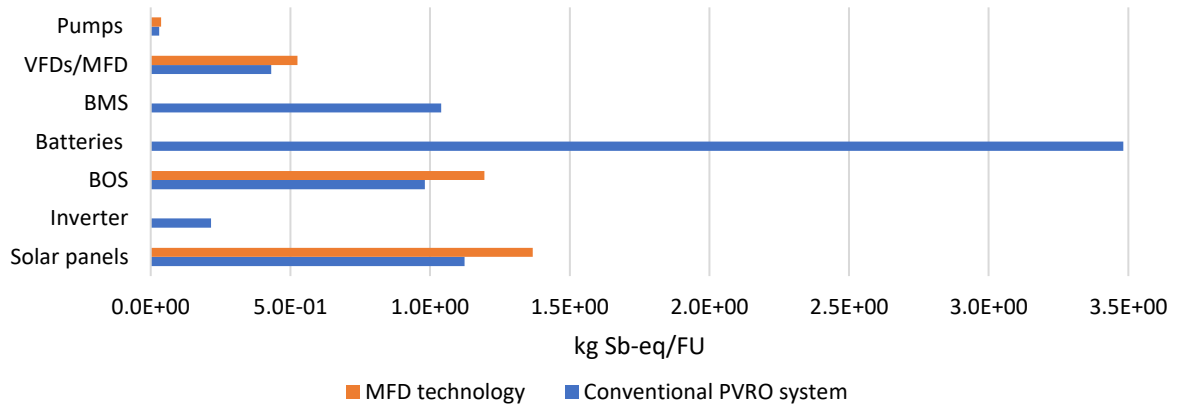
Figure 40 comparing the abiotic resource depletion for a conventional system and MFD technology.

c- Ecological consequences - Climate change (GWP100)

GWP describes the change in global temperature caused by the greenhouse effect. Based on the cumulative radiative forcing impact of different greenhouse gases, GWP provides a relative index to compare emissions over a predetermined time frame, often 100 years. The main GWP components of typical PVROs are batteries and solar panels. According to fig. 41, using MFD technology lowers the GWP by more than 30%.
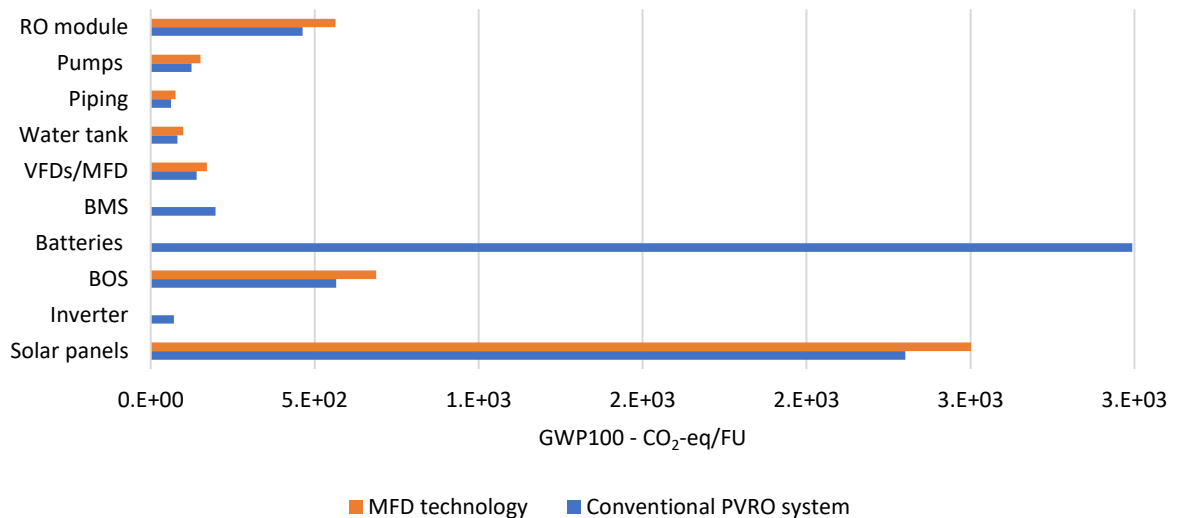
Figure 41 comparing the climate change potential of a conventional system and MFD technology.

d- Ecological consequences - Ozone depletion potential

The Ozone Depletion Potential (ODP) is used to estimate the relative effectiveness of the product or process in the depletion of the stratospheric ozone layer based on the ratio of the atmospheric lifetime and infrared radiative efficiency of emitted substances. During battery fabrication processes, Chlorofluorocarbons (CFCs) are released, especially during the production of aluminium and steel, halogenated compounds are used in solvents, refrigerants

and foam-blowing agents which have a negative effect on ozone depletion (ODP). Although the ODP is dominated by PV panels production, removing the batteries can reduce the ODP by about 10%. ODP is the only impact category in that MFD technology could not improve the result significantly. The values are compared in fig. 42.
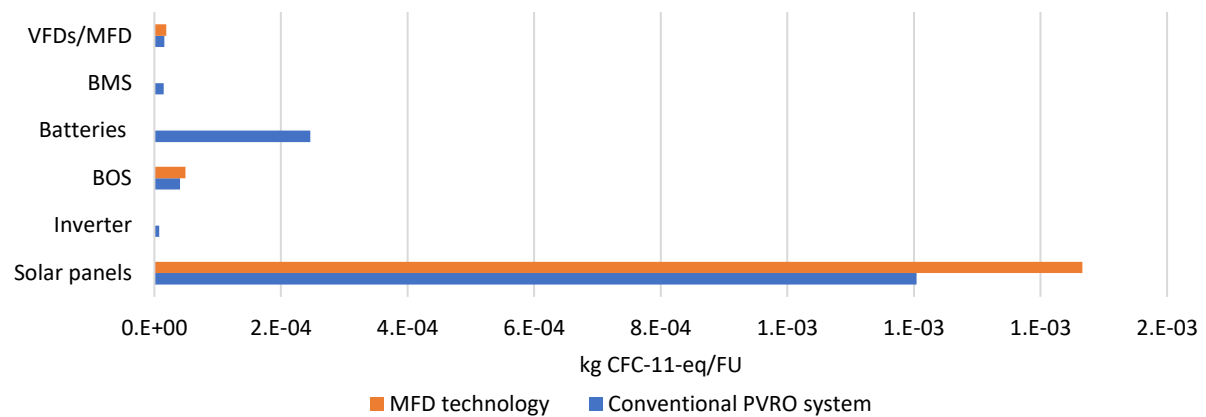
Figure 42 comparing the ozone depletion potential for a conventional system and MFD technology.

e- Ecological consequences - Acidification potential

Acidification Potential (AP) is a metric to quantify the contribution potential to the acidification of the environment, which may have detrimental effects on human health as well as on biodiversity, soil fertility, and water quality. The primary source of AP is sulfuric and nitric acids, which can be generated by SO_2 and NO_x emissions. Batteries and BOS are the primary sources of acidification in PVRO systems. This aspect can be reduced by more than 40% in MFD technology, i.e., the acidification is 35.9 kg SO_2-eq and 19.7 kg SO_2-eq in conventional PVROs and MFD technology, respectively.

f- Ecological consequences - Eutrophication potential

The emissions of nitrogen compounds, such as nitrates and ammonium, can increase the concentration of nutrients, like nitrogen and phosphorus, in a body of water, leading to an overgrowth of algae and other aquatic plants that degrades the water's quality and harms aquatic life. Using MFD technology has the highest effect on this category, as batteries and BMS mainly cause eutrophication. Eutrophication potential dropped from 7.62 kg PO_4^{-3} to 1.39 kg PO_4^{-3} by removing batteries. Fig. 43 depicts how eutrophication potential is dominated by the battery system, and the value of other components is entirely negligible.
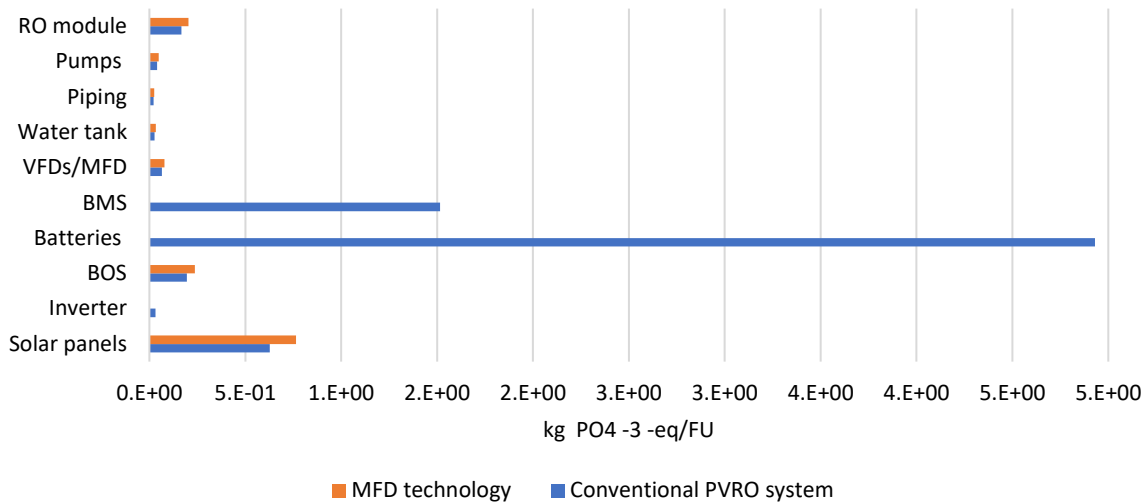
Figure 43 comparing the Eutrophication potential for a conventional system and MFD technology.

g- Human health- Human toxicity potential (HTP)

Calculating the effect of a system on human health is one of the challenging parts of any lifecycle analysis in general. HTP measures the harmful chemicals generated and released to the ambient during the whole lifecycle. Excavation and mining process of the raw materials, especially aluminium, cadmium, lithium, nickel, copper, and mercury, which are used in PV panels, BOS and batteries, are the main contributions to this field in PVRO systems.

HTP also has a proportional relation to the CED because generating power and electricity is always bonded with the releasing non-methane volatile organic compounds (NMVOC), which has a high effect on the HTP.

The value of the HTP for the conventional system is $9.1 \times 10^{+3}$ kg 1,4-DCB equivalents, which is 30% higher than MFD technology with an HTP of $6.38 \times 10^{+3}$ kg 1,4-DCB equivalents.

h- Human health - Ionising radiation potential (IRP)

Ionizing radiation potential (IRP) is used to measure a substance's ability to release ionizing radiation, which can negatively impact both the environment and human health. IRP refers to the amount of different radiations like α-, β-, and γ-rays, which are emitted in different stages of the product life cycle[148]. Similar to the HTP, the mining process has the highest effect on the IRP. Because during the excavation, ionising bedrock can simultaneously be extracted. In PVRO systems, IRP is dominated by PV panels. Therefore, removing the batteries enhances this environmental aspect by about 25%. The IRP of the conventional system is $7.06 \times 10^{+2}$ kg of uranium-235 (U^{235}) equivalents, while this value for the MFD technology is $5.25 \times 10^{+2}$ kg of uranium-235 (U^{235}) equivalents.

66

Chapter 5

Accelerated test bench and validating the performance data

---

5. Accelerated test bench and validating the performance data

As explained in chapter 2, in MFD technology, batteries can be removed, and the system works in a dynamic mode. The speed and frequency of the pumps are adjusted via using customized variable frequency drivers (VFDs) since the output power of photovoltaic (PV) modules varies between 0 and 1300 $W.m^{-2}$ throughout the day, depending on the ambient conditions.

In fact, the MFD technology tracks the solar energy curve and adjust the energy demand of the system according to the available solar power. The main task of the control system is to compensate for fluctuations in solar energy by regulating the speed of the pumps and adjusting the working pressure of the system. The dynamic operation can considerably change system hydrodynamics conditions like concentration polarization (CP), membrane-foulant interactions, and transmembrane pressure (TMP)[149,150]. In recent years, several studies have been performed to investigate the effects of energy fluctuation on the performance and lifespan of membranes. These experiments were either carried out in lab conditions without validating the results or in real conditions with a constrained time[151].

Richards et al. investigated the effect of fluctuant energy on the retention of dissolved contaminants from real Australian groundwater using a solar PV-powered ultrafiltration–nanofiltration/ reverse osmosis (UF–NF/RO) system[152]. Similarly, a recent study investigated the influence of intermittent working conditions on a lab-scale solar RO system. The operating conditions and feed water properties are taken from a real-case system in La Mancalona, Mexico. Different test scenarios have been investigated, including using anti-scalant and flushing the system prior to each shut-down period. The intermittent operation was defined as 8 hours working at a fixed pressure (20.7 bar), fixed recovery ratio (75%), and fixed flow rate (9×10^{-6} m^3/s), followed by 16 hours shut-down period. In addition, cross-flow cells were used in the prototype instead of spiral wound membranes. The short-term (several days) investigation does not show any destructive influence. However, using an anti-scalant and flushing the membrane could improve the system's performance[153].

In this work, the long-term performance of the PVRO system under intermittent operation is investigated by designing an accelerated test bench. There are two main power fluctuation sources in solar energy. First, according to the specific character of the solar radiation at different locations, a bell-shaped curve appears initially on a daily time scale. Second, cloud

coverage causes changes in power generation over a shorter period. Based on the wind speed, the shadow movements can happen very fast, which leads to sharp energy decline and fast fluctuations. These changes can cause significant pressure drops in pressure vessels, which are considered in this study as well.

The other critical issue is investigating the fouling and scaling status. The scaling mechanism is very complicated and depends on various parameters like feedwater chemistry, concentration polarization, electrostatic attractive forces, van der Waals forces, chemical bonding, hydrophobic interaction, and hydrogen bonding[154,155]. In general, there are four different main foulants; Sparingly soluble inorganic compounds, like calcium, carbonate, sulphate, magnesium, phosphate, can form a scaling layer, specifically if concentration polarization has occurred on the membrane surface[156]. Because in this situation, the solubility of the dissolved ions reaches the precipitation threshold[157]. Particulate and colloidal particles, which cannot pass through the membrane, have a high potential to form a dense fouling layer on the membrane surface[158]. Organic fouling occurs because of the interactions between organic substances [159], mainly aquatic and natural organic matters (NOM)[160]. However, compared to the other foulants, organic matters can be effectively detached from the membrane by alkaline chemical cleaning[161]. Nevertheless, organic substances with aromatic carbon can create an adhesive and irreversible scaling layer on the polyamide membranes due to the strong foulant-membrane hydrogen bonding[162]. Biofilms can form on the surface and in the internal layer of the membrane by microbial cells[163]. Especially, Low Molecular Weight (LMW) organics, which are tinier than the pore size (molecular weight cut-off (MWCO)) of the membranes, can deposit on the active layer or even penetrators the deeper layers[164].

In addition, scaling increases the concentration polarization potential as it reduces the back diffusion[165,166]. Therefore, scaling layers also indirectly reduce membrane's efficiency. However, Park et al. showed that the turbulent crossflow induced by the dynamic operation could physically detach the fouling layers from the membrane surface[167].

5.1. System Assembly

In this section, an accelerated test bench is designed to investigate the durability of membranes under dynamic operation conditions with surrogate feed water. The same system

(pilot project) is installed in Cape Coast to validate the data. At the end of the project, performance and conditions of membranes of both systems are compared. The pilot project in Cape Cost is shown in fig 44. The only difference between the systems is the feed water source, i.e., the pilot project gets the water from a deep coastal borehole (110 m), while the test bench works in a closed loop to reduce water consumption. The feedwater of the test bench is exactly simulated based on the borehole water analysis from the pilot project.

Figure 44 the pilot project was installed in October 2020, and performance data were gathered using a remote monitoring system. 8 kWp panels were installed to power the system.

5.1.1. Hydraulic system

In the test bench, surrogate feedwater is dragged by the feed pump (LOWARA pump, model 1HM08N) to provide a certain input pressure for the high-pressure pump to overcome the pressure loss of the pre-filtration system and to avoid cavitation. The pre-filtration system contains three cartridge filters, including a 20 µm, a 5µm, and an active carbon filter. Analogue pressure gauges, an analogue flowmeter, and a pressure sensor are installed on the piping system.

The filtration system and instrumentation of the pilot project are the same. Just as the borehole water contains more suspended solids, a multimedia filter is added before the feed pump. The multimedia filter can remove all particles larger than 50 µm, and the filter will be flushed automatically after filtering 3 m^3 of feed water.

A triplex plunger pump is used as the high-pressure pump (Interpump - Model SS 1414) to provide 840 L h^{-1} for the membranes. To reduce the vibration, a compressed-gas Pulsation Dampener is installed at the pump output, which smoothens the pressure. An analogue high-pressure gauge and a pressure sensor are installed at the pump output to measure the

membrane's pressure. Four membranes are connected in series. Hence, the brine of the upstream membrane is applied as the feedwater of the downstream membrane.

An electric proportional valve is installed at the brine output of the last membrane. Opening or closing the proportional valve determines the system pressure. When the hydraulic pressure in the membrane vessels exceeds the osmotic pressure of the feedwater, feed water split into two streams. The first stream leaves as the brine flows through the proportional valve, and the second flow as the permeate through the membrane pores. The permeate temperature is measured by using a temperature sensor (PT1000). In addition, the permeate flux is measured via an electric vortex flowmeter. A conductivity meter is used to measure the remaining salt concentration in the permeate stream. Another analogue floating flowmeter is installed in the permeate output line to observe the permeate production.

The permeate line has a non-return valve to prevent the produced water from diffusing back to the membranes when the system is off.

5.1.2. Control system

The control system is mainly responsible for converting the DC power, generated by the photovoltaic modules into AC power with different frequencies to supply the pumps. Moreover, as mentioned before, the main challenge for the control system is to compensate for the power fluctuance without influencing the system's performance.

The control unit includes one master controller and three slave controllers. Fig. 45 illustrates the function of each controller and the communication structure.
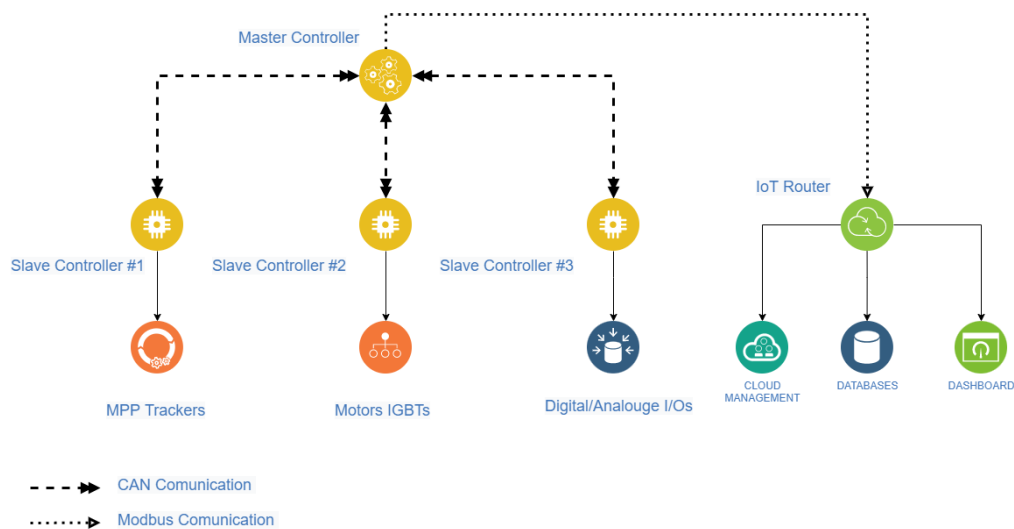
Figure 45 Communication topology of the system; Modbus is applied to transfer the data to the remote monitoring system, whereas CAN protocol is used for internal communication between the controllers as it is faster.

71

Input data will be gathered and processed by slave control #3. Based on this information, the master controller calculates the duty cycle of the MPP-Trackers and generates the set point for slave controller #1. In the same way, the set points for pump frequencies and the working pressure of the system are generated and delivered to slave controller #2. The CAN signal, specifically to deliver integer values, is fast enough to provide smooth operation between the controllers. However, using float values can reduce the communication' speed significantly. In this situation, as the microprocessor is faster than the signal transportation, generated set points cannot be delivered to the relevant slave controllers at the defined time. Consequently, the control unit will face serious problems. Therefore, all float values should be transformed into integer format.

The pilot project has three main pumps, including a borehole pump, feed pump, and high-pressure pump, while for the accelerated test bench borehole pump is not applicable. However, to simulate the same load and energy management condition for the control unit, an external centrifugal pump (Model: Lowara BG11/D) is added to the system. Therefore, the MPP-Tracker can be tested in real-case power consumption.

The slave controller #2 controls the frequencies of all pumps. The AC frequency of the pumps determines the speed of the pumps proportionally and, consequently, the water flux. By adjusting the frequency, the power consumption of the pumps can be varied and therefore, the system's energy demand can be adapted to the available solar power.

The pilot project is powered by 24 PV Panels, which can provide 8 kWp of solar energy. The panels are divided into two separate PV arrays, including 12 panels in series in each array. The arrays are directly connected to each MPP Tracker of the control unit. To provide the same condition for the accelerated test bench, the PV system is simulated using two separate Solar Power Simulator units (DataTec PSI 9750-20 3U[11] - see fig. 46). Each Simulator Unit is connected to one MPP Tracker and generates the same power and condition as the real situation in the pilot project. Simulation of the PV panels is performed based on DIN EN 50530[168], and ambient parameters (irradiation and temperature) are imported into the unit in time-series data. The panel parameters are mentioned below:

V_{oc} = 505.0 V, I_{sc}= 10.0 A, V_{mpp}= 440.0 V, I_{mpp}= 9.0 V

which results in a total power of 3.960 kWp for each Simulator Unit.

---

[11] https://www.farnell.com/datasheets/1907680.pdf

Figure 46 two DC Power suppliers from Datatec (series 9000) are used to simulate the solar power for each MPP tracker. The performance accuracy of the system is <0.1%, the Load Regulation 0-100% accuracy is <0.05%, the accuracy of the Line regulation ±10% ΔU_{AC} is <0.02%, the Regulation Speed 10-100% load is <2 ms, and Slew rate 10-90% is maximum 30 ms.

The pilot project is an off-grid solution, and there is no grid available. Subsequently, the battery of the remote monitoring system should be simultaneously charged with the available solar energy during the daytime. The input solar energy provides max. 600 V DC, the control system adjusts the intermediate circuit voltage in the range of 500 to 610 V DC. The same circuit and voltage should be used to supply the battery management system, which works between 20-28V. Therefore, a voltage transformer is added to power the battery unit.

5.2. Test conditions

5.2.1. Surrogate Feedwater

To simulate the feedwater for the accelerated test bench, the borehole water of the pilot project is analysed (See Appendix 1). The composition of the tab water of Nuremberg (the location of the test bench) is subtracted from the compositions of the borehole water.

The tap water needs to be mixed with additional chemicals and salts to have the same borehole water chemistry. Table 9 shows the information and amount of chemicals added to the feedwater. The values are calculated based on the capacity of the feed tank (640 L).

Table 9 different chemicals are added to the feed water to simulate the exact properties of the borehole water from the pilot project. Chemicals and the added amount are listed in the table below.

Item	Chemical	molar mass g/mol	Chemical (mol)	Cation (mol)	Anion (mol)	Chemical (g)	Cation (g)	Anion (g)
						Chemical amount to be added		
1.	$Fe(II)Cl_2 \times 4H_2O$	198.81	0.01980	0.01980	0.05939	3.90	1.11	2.10
2.	K_2SO_4	174.26	0.17136	0.34273	0.17136	29.90	13.40	16.46
3.	$MgCl_2 \times 6H_2O$	203.3	1.86900	1.86900	3.73800	380.0	45.43	132.52
4.	$CaCl_2 \times 2H_2O$	147.02	2.00609	2.00609	4.01218	294.90	80.40	142.24
5.	NaCl	58.44	8.78362	8.78362	8.78362	513.30	201.93	311.40
6.	$Mn(II)SO_4 \times H_2O$	169.02	0.01073	0.01073	0.01073	1.80	0.59	1.03
7.	NH_4Cl	53.49	-0.00037	-0.00037	-0.00037	0.00	-0.01	-0.01
8.	Na_2SO_4	142.04	0.52931	1.05862	0.52931	75.20	24.34	50.84
9.	NaF	41.99	0.00670	0.00670	0.00670	0.28	0.13	0.13

Different chemicals like Sodium chloride 99.5%, Calcium chloride 99%, Sodium hydroxide 99%, and Magnesium chloride 99% from Stierand GmbH are used to simulate the feed water. In addition, Sodium sulfate 99% from Merck, sodium disulfate 97% from WHC GmbH, and Magnesium chloride 99% from Riedel-Haen are added to the water. Other chemicals are supplied from different manufacturers.

After adding the chemical to the feed tank, four water samples were taken, and the physical and chemical properties of the water streams were tested. The values are shown in table 10 and table 11 compares the simulated water (2W20274-5 and 2W20274-8) and the borehole water (2W20274-1). The sampling conditions are explained in table 10.

Table 10 complete water analysis is done to measure the physical and chemical properties of the simulated water.

Sample ID	Sample stream	Sampling description
2W20274-1	Borehole water	After 24 hours of pumping from the borehole
2W20274-5	Feed water tank	Directly after adding the chemicals
2W20274-6	Concentrate stream	After 50 min running the system at 50 Hz
2W20274-7	Permeate stream	After 50 min running the system at 50 Hz
2W20274-8	Feed water tank	After 50 min running the system at 50 Hz

Parameter	method	2W20274-5	2W20274-6	2W20274-7	2W20274-8	unit
Calcium	DIN EN ISO 11885 2009-09	315.6	430.5	0.70	305.2	mg/L
Magnesium	DIN EN ISO 11885 2009-09	305.8	417.0	0.67	296.0	mg/L
potassium	DIN EN ISO 11885 2009-09	36.5	54.5	0.52	38.1	mg/L
sodium	DIN EN ISO 11885 2009-09	347.7	473.3	6.12	338.3	mg/L
Fluoride	DIN 38405-D4-1 1985-07	0.86	1.20	<0.15	0.91	mg/L
Nitrate	DIN EN ISO 10304-1 2009-07	8.5	11.1	<0.5	8.4	mg/L
Chloride	DIN EN ISO 10304-1 2009-07	1714	2593	11.3	1726	mg/L
Iron	DIN EN ISO 17294-2 2017-01	1.22	<0.01	<0.01	0.39	mg/L
manganese	DIN EN ISO 17294-2 2017-01	6.07	8.18	<0.01	5.85	mg/L
Sulphate	DIN EN ISO 10304-1 2009-07	94.3	131	<0.5	96.2	mg/L
pH	pH meter	7.5	NA	NA	7.5	
TDS	TDS meter	3750	NA	NA	3700	mg/L

NA   Not Measured

As shown the table 11, the average value is 13.1% and 18.5% for deviation 1 and 2, respectively. However, Deviation 2 is mainly influenced by the deviation of iron. The value is remarkably high because iron particles can be deposited as sediment immediately on the pre-filters. Therefore, the iron concentration is reduced. By removing the iron, the average value of deviation 2 will be reduced to 11.7%, which shows an acceptable approximation between simulated water and properties of the borehole water. Fig. 47 illustrates the deviations.

Table 11 to provide the same working condition for the test bench, the borehole water (2W20274-1) from the pilot project in Ghana is simulated. The deviation between the simulated water (both 2W20274-5 and 2W20274-8) and borehole water is calculated in this table.

Sample ID	TDS	Na	K	Ca	Mg	Fe	Cl	Sulphate	Mn	F
2W20274-1	3528	380	30.4	292	280	1.98	1643	80	6.19	0.74
2W20274-5	3750	347.7	36.5	315.6	305.8	1.22	1714	94.3	6.07	0.86
2W20274-8	3700	338.3	38.1	305.2	296.0	0.39	1726	96.2	5.85	0.91
Deviation 1	6.29%	8.50%	20.07%	8.08%	9.21%	38.38%	4.32%	17.88%	1.94%	16.22%
Deviation 2	4.88%	10.97%	25.33%	4.52%	5.71%	80.30%	5.05%	20.25%	5.49%	22.97%

| Note: |
| Deviation 1:   Deviation between simulated water, 2W20274-5 and the borehole water (2W20274-1) |
| Deviation 2:   Deviation between simulated water, 2W20274-8 and the borehole water (2W20274-1) |

Feedwater composition shows a high potential for scaling. In general, negative ions, including bicarbonate, silicate, and sulphate, can facilitate the precipitation of other compounds. The presence of other elements in the fouling layer is also pervasive, including aluminium silicates, carbonate compounds of Ca and Mg, and sulphate compounds of Ca, Sr, and Ba[169]. Furthermore, multivalent metal cations, particularly Ca^{2+}, have a high tendency to create fouling layers in combination with natural organic matter (NOM) and to connect the organic foulant molecules and form a Ca-NOM structure[170], especially in the presence of the negative charge NOMs like carboxylic and phenolic types[171]. The same interaction can occur between calcium and humic acids, with protein or polysaccharide-like structure, which forms a Ca-HA porous layer on the membrane[172,173]. Especially due to the high pH value of the feedwater, Ca-HA formation can be enhanced[174].

The high value of $CaCO_3$ also increases the scaling probability as the solubility product constant (K_{sp})[175] of $CaCO_3$ is very low (K_{sp} at 25°C= 2.8×10^{-9})[176]. $CaCO_3$ can create three types of crystalline polymorphic, namely calcite, aragonite and vaterite. Especially, as the calcite crystals are thermodynamically very robust and can form both rhombohedral morphology with sharp straight edges and small aragonite needle batches[177]. Therefore, $CaCO_3$ can form an irreversible and dense alkaline scaling layer.
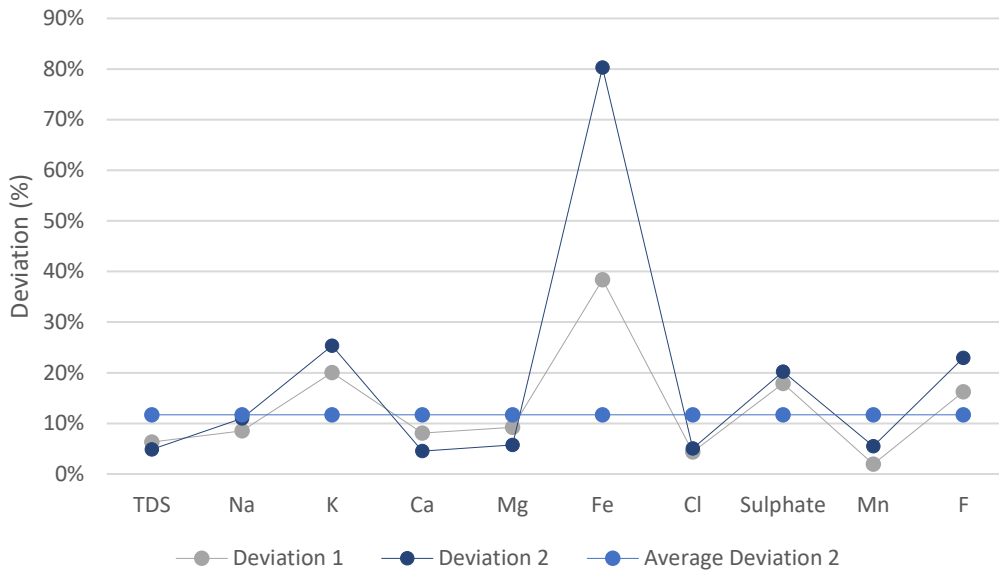
Figure 47 borehole water is simulated for the test bench by adding different salts to provide the same working condition. The graph shows that the average deviation between borehole water and the simulated water is about 10%.

5.2.2. Accelerated test scenario

An extreme test scenario is defined as an accelerated test of the real condition to investigate the performance and lifetime of the membrane under dynamic conditions, i.e., variable pressure and flowrate. The daily operation time of the pilot project usually is around 6 hours, which is simulated and accelerated in 90-min cycles for the test bench.

Irradiation fluctuation is the main reason for the power and, consequently, the pressure changes in the system. Specifically, sharp energy decline induced by clouds' movements can create significant power changes. If these fluctuations are not controlled and damped via the control unit, they can lead to severe damage to the lifespan of the membranes and other mechanical equipment.

To create harsh test conditions, sharp irradiation fluctuations are considered, i.e., in each test cycle, the irradiation drops to the minimum operation power every ten minutes and increases to the same power in ten seconds. Therefore, each cycle has nine sharp energy reductions. 540 measurement points are considered for each cycle. Essential performance data are observed to investigate the behaviour of the membrane during the test. Fig. 48 shows the simulated energy curve of each 90-min test cycle, including 540 measurement points. After each cycle, the system will be shut down for 30 minutes and starts another cycle again. This procedure is repeated four times a day to have the same conditions for the scaling, as the pilot project is off overnight.
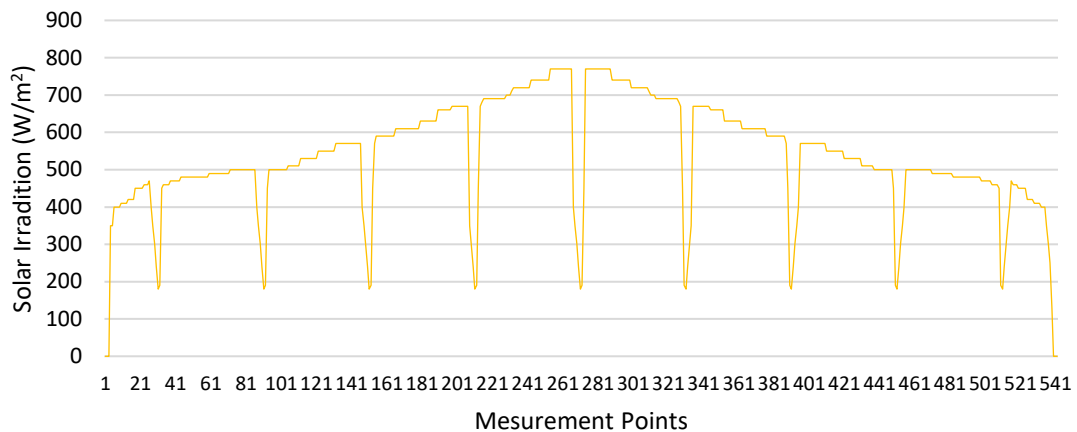
Figure 48 The solar energy curve, including both types of fluctuations, is simulated using the Solar Simulator from Datatec (see fig. 46). Each curve has a 90-min running period and includes nine sharp energy reduction shocks. The test will be followed by a 30-min standstill period.

To the best of my knowledge, this is the first time that a PVRO system has been tested under such a comprehensive test scenario, including both types of solar radiation fluctuations. In addition, the accelerated test bench was working for a long-term period, i.e., eight months, that simulated three years of the normal operation. Besides, enough standstill periods are considered to simulate the same working condition for the overnight scaling.

5.2.3. Logging and observation

The main challenge of the control system is to adjust the frequencies of the pumps in a way that the water quality is always within the standard values. At the same time, the lifetime of mechanical parts, especially the membranes, should not be endangered. A remote monitoring system is designed for the pilot project, and a JAVA-based software is programmed for the accelerated test bench to monitor the system's behaviour. Both logging systems have a ten-second resolution. While all data are monitored, only the crucial parameters, which highly influence the system's performance, are recorded to reduce the data volume. These parameters include battery voltage, system power, the pressure of the feedwater line, the pressure of the membranes, permeate salinity, permeate temperature, the flow rate of produced water, and the voltage of the intermediate circuit. Logging samples can be found in Appendix 5.

Water samples have been regularly taken and sent to an accredited water analysis laboratory to observe the water quality[12]. As mentioned before, there are three streams in the system,

---

[12] https://www.fem-online.de/en/content/accreditation

namely feed, permeate, and brine flow. Four samples should be taken from each stream; therefore, in total, twelve samples were sent in a temperature-controlled condition to the laboratory. The tests were done in less than 24 hours after taking the samples because time and temperature can affect the results of the microbiological tests. Part of the test results is shown in Table 12.

Table 12 both physical analysis and microbial examination are performed to investigate the variation in water properties during the time. The complete set of results is listed in the table below.

Par	04/03/2021			09/03/2021		
	Feed	**Permeate**	**Concentrate**	**Feed**	**Permeate**	**Concentrate**
Al	<0,01	<0,010	<0,01	<0,010	<0,010	<0,010
As	<0,001	<0,001	<0,001	<0,001	<0,001	<0,001
Bromide	<0,1	<0,1	0,13	<0,1	<0,1	0,15
Ca	184	< 0,5	364	182	< 0,5	482
Cd	<0,0002	<0,001	<0,002	<0,0002	<0,0002	<0,0002
Cl	958	3,7	1780	982	4,63	2376
Cu	<0,005	<0,005	0,034	<0,005	<0,005	<0,005
F	1,08	0,15	2,14	1,08	<0,15	1,47
Fe	0,910	<0,01	0,094	<0,010	<0,010	<0,010
K	23,1	< 0,5	44,6	22,9	< 0,5	60,8
Kol20	>2000	252	>2000	13100	275	2500
Kol36	>2000	253	>2000	18400	248	1500
Conductivity	3450 (16,9 °C)	17,4 (16,6 °C)	6390 (16,9 °C)	3440 (18,4 °C)	20,9 (18,8 °C)	8370 (18,8 °C)
Mg	92,8	< 0,5	118	92,2	< 0,5	245
Mn	1,7	<0,005	3,3	1,6	<0,005	4,0
Na	357	2,5	693	362	3,4	929
NH4	<0,05	<0,05	<0,05	<0,05	<0,05	<0,05
Ni	<0,001	0,001	0,016	0,004	0,004	0,004
NO3	10,3	<2	43,42	9,00	<2	26,11
o-PO4	<0,03	<0,03	<0,03	<0,03	<0,03	<0,03
Pb	<0,001	<0,001	<0,001	<0,001	<0,001	<0,001
pH	7,5 (17,5 °C)	5,6 (17,0 °C)	7,7 (17,3 °C)	7,7 (20,3 °C)	5,8 (19,3 °C)	7,8 (19,0 °C)
SO4	106	<2	196	104,91	<2	256
TOC	0,58	<0,2	0,97	1,1	0,52	0,92

5.3. Result and discussion

5.3.1. System performance

5.3.1.1. Performance of the accelerated test bench

a. Analysis of logging data from the control unit

The most critical point of system operation is throughout the irradiation fluctuation, especially during the sharp energy reductions. The test bench operated under the defined test conditions (see sec. 5.2.2) for four months in the first round. Fig. 49 depicts the system's behaviour during the simulated sharp energy fluctuations. The whole process, i.e., reducing the energy to the minimum allowed value and increasing it back to the initial point, takes 60 seconds. The graphs in fig. 48 shows the performance of the system for this short period. Each graph illustrates the logging data taken at the end of each 30-day test time. A complete set of the logging data is shown in Appendix 5.

As shown in the graphs, the control unit compensates for the power drop via reducing the frequency of the pumps and, consequently, by reducing the system's power consumption. As mentioned above, nine power drops at different points of the energy curve are planned in each cycle. The frequency changes between 50 Hz and 30 Hz depending on the fluctuation time. Such a fast frequency drop can cause a severe and significant fluctuation in the system, especially in the working pressure and consequently on the salinity of produced water. To avoid this effect and guarantee water quality, the control system applies the three mechanisms explained in section 2.2.1. Therefore, despite the sharp frequency decline, the TDS value is always stable in all graphs. Other parameters like working pressure and permeate flux are marginally reduced.

These results confirm that the control unit can successfully compensate for the sharp energy reductions and adjusting the frequency did not cause any problem or significant effect on the system operation. Especially fig. 49 (d) indicates that, although the pump frequency is reduced to 30 Hz, the permeate flowrate is just decreased slightly to 8 l/min and the salinity of the permeate stays almost the same.
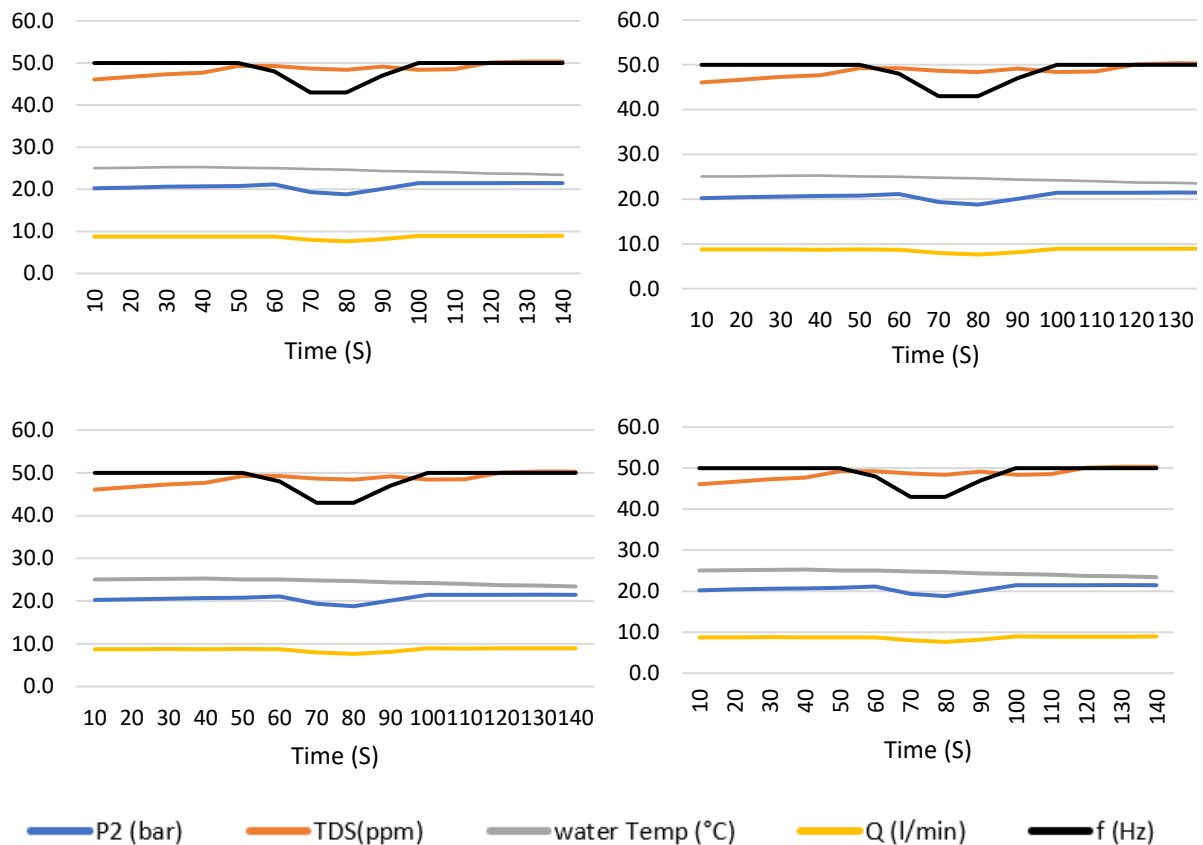
Figure 49 operating properties of the system under the fluctuation phase (first round of the tests). Each diagram is taken at the end of each month of the test.

To investigate the potential degradation, after four months of the accelerated tests, which is equal to 480 cycles, i.e., 480 simulated working days, the performance parameters are compared at the same condition (50Hz) at the end of each 30-day test period. Fig. 50 and table 13 show the values of the system under dynamic operation. The values are all taken at 50 Hz when the system is entirely stable to neglect other variations. As shown in fig. 50, the conductivity of the permeate stream has increased from 75 microS/cm to 242 microS/cm, which confirms that the membranes are degraded to some extent. This decline in the salt retention efficiency of the membranes can be due to the formation of scaling layers or can be attributed to a physical damage. However, the conductivity value is still below the critical value in WHO guidelines. Membrane degradation is normal, and in fixed-speed RO systems, membranes should be changed after three years. The main reason for such degradation is fouling and scaling on the surface of the membrane[178], which is investigated in the following sections. Other factors like permeate flux, working pressure, and temperature stayed the same and verified that dynamic operation did not influence the system's performance.
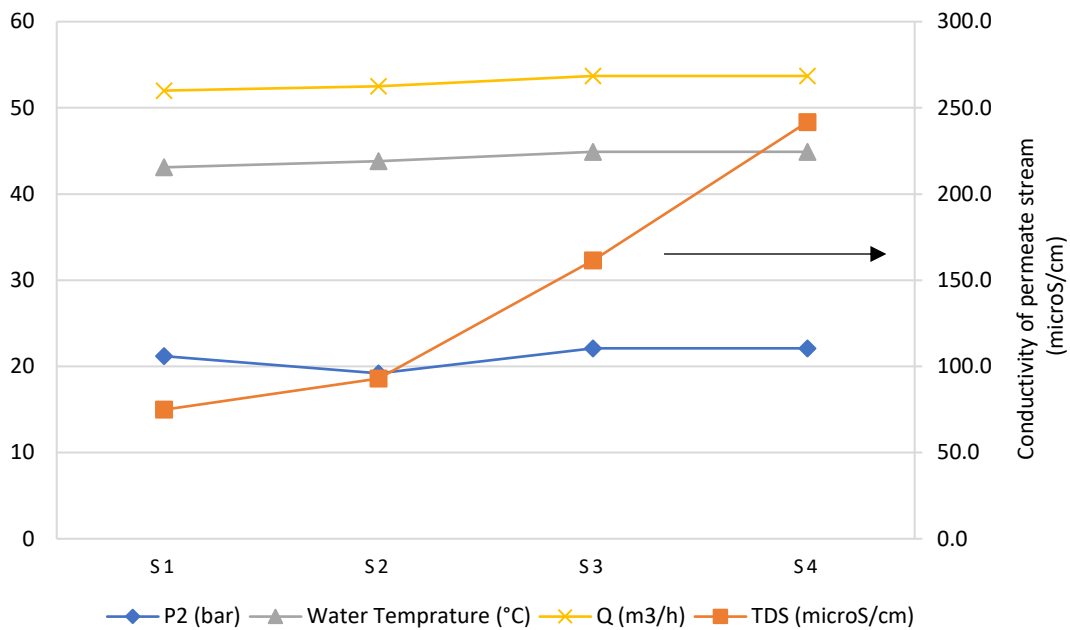
Figure 50 performance parameters are shown at the end of each month. There is a significant increase in water conductivity, which is normal after 480 cycles, i.e., 480 working days in harsh operating conditions.

Table 13 the operation parameters during four months of operation.

	P2 (bar)	TDS (microS/cm)	Water T (°C)	Q (l/min)
S1	21.2	75	21.9	8.9
S2	19.2	93.2	24.6	8.7
S3	22.1	103	22.8	8.8
S4	22.1	103	22.8	8.8

The results from the water analyses are investigated in the next section to find out the exact reason for the degradation.

b. Investigation of water analyses

- Dissolved salts

The most important performance indicators in RO systems are the electrical conductivity of the permeate and the transmembrane pressure (TMP). According to table 13, the TMP has an insignificant increment, i.e., 4.2%, while conductivity increased by 37.3%. Scaling can be attributed as a potential reason. However, scaling deposition should also increase the TMP[179]. Therefore, the exact reason should be investigated. Fig. 51 shows the different streams' conductivity, throughout the test period, including more measurement points.
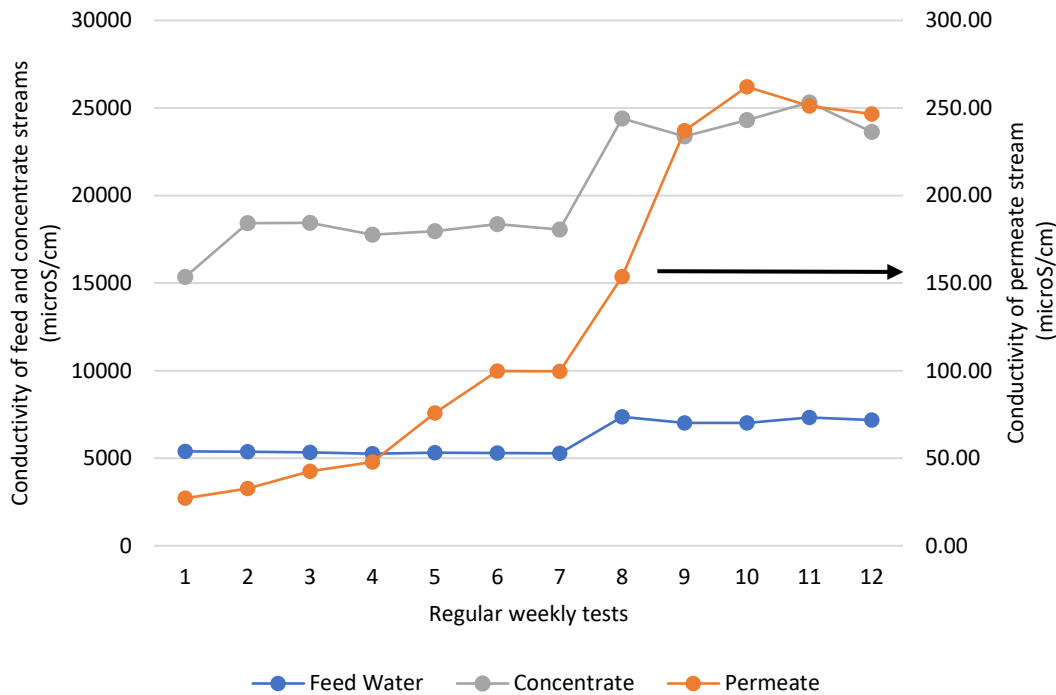
Figure 51 water conductivity is mainly due to NaCl ions in water. Therefore, it is the best indicator to measure the quality of the produced water and, consequently, the performance of the membranes. The conductivity of all streams is measured weekly, depicted in the graph.

During the first seven weeks, conductivity increased gradually due to the formation of scaling layers. However, there is a remarkable rise in conductivity value in weeks eight and nine, followed by stable conditions. This sharp increase indicates a physical degradation, like micro-cracks formation or membrane integrity loss[180]. Which leads to less salt retention in membranes. Salt rejection efficiency (R) is defined in equation 45, and based on the test results, R is reduced from 98.9% in week #7 to 97.8% in week #10, while it was 99.6% in the first week. If salt retention reduces by 5-10%, the membrane should be cleaned or changed[13]. Therefore, the membranes are still in operational status.

$$R = \left(1 - \frac{C_{Permeate}}{\frac{C_{feed}+C_{concentrate}}{2}}\right) * 100 \qquad \qquad \text{Equation 45}$$

The same analysis is performed for other dissolved ions to evaluate if this decline in salt rejection is due to physical degradation and is not a measurement mistake. It is expected to have a similar trend for other chemicals too. Fig. 52 shows the concentration of sulphate (SO_4) in different streams.

---

[13] Dupont, FilmTec reverse osmosis membranes technical manual
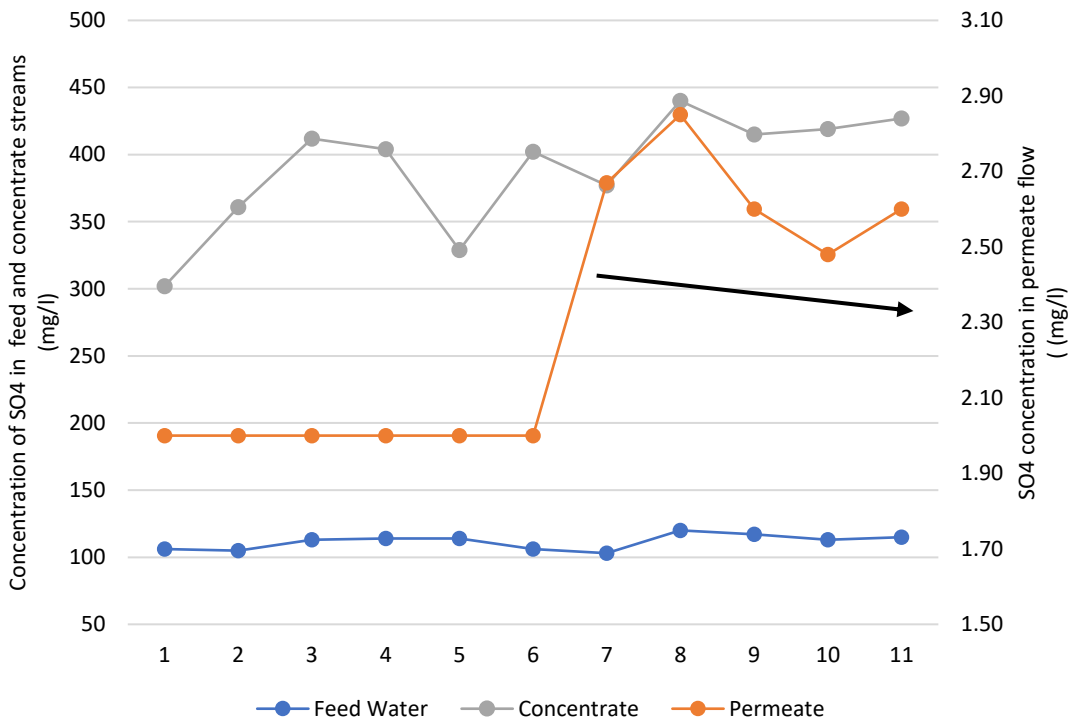
Figure 52 concentration of sulphate (SO₄) in permeate, concentrate, and feed water.

After week #6, the concentration of SO_4 increased remarkably, which depicts the same behaviour as the conductivity measurement. Hence, a kind of physical degradation occurred in week #6. Although the values decreased again after week #8, it seems more like an error during the measurement.

Other dissolved ions, such as Fluoride, Magnesium, and Potassium, also can pass through the pre-filtration unit. However, as they are larger than the membrane's pores, these particles are mainly rejected into the brine stream. The salt rejection is 98.5%, 98.4%, and 99.7% for Fluoride, Magnesium, and Potassium in the first week, respectively. However, salt retention decreased after week #6 due to the physical degradation, which was discussed in the previous section. For instance, the salt rejection of Fluoride reduces to 96.7% in week #10. The same trend occurred for Magnesium and Potassium, with one week delay. It shows that the degradation happened in week #6 and got worse during weeks #7 and #8. At the beginning of the degradation, i.e., week #6, solely smaller ions could pass through, while in the following weeks, bigger ions penetrate the membrane as well. Fig. 53 shows the filtration behaviour.
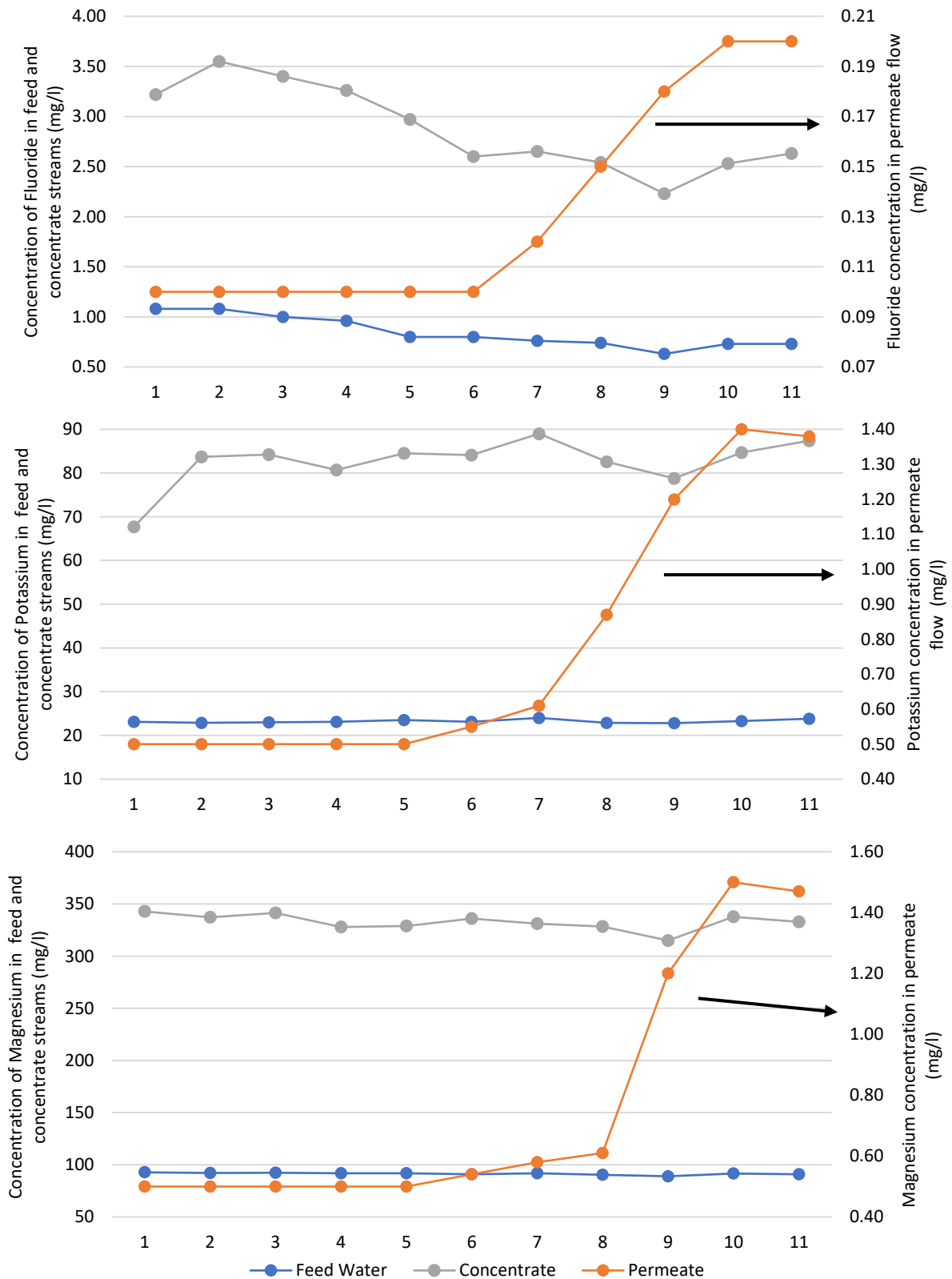
Figure 53 dissolved ions like Fluoride, Magnesium, and Potassium can pass through the pre-filter. The graphs show that the membranes could reject these ions in the first weeks, but the ions could gradually penetrate the permeate side after the physical degradation.

The filtration behaviour of other ions like Iron and Manganese are different. Iron is mainly filtered by pre-filtration. Fig. 54 (top graph) shows that iron concentration in feed and

concentration stream dropped to almost zero within the first week. The iron rejection efficiency is 98.0% in the first week, and the permeate contains a small amount of iron. As iron is filtered in the pre-filtration unit and does not affect the project, it was decided not to add more iron to the feed water anymore to reduce the workload. That is another difference between the test bench and the pilot project. However, the only influence is the more frequent changing of pre-filters in Ghana than in the test bench

Manganese can be partially filtered by the pre-filtration unit. Therefore, the concentration of manganese reduced gradually in the concentrate and the feed water with the same trend as manganese ions are slowly trapped in pre-filter pores (Fig. 54, bottom). Still, some ions can pass through the pre-filter. However, these ions could not pass through the membrane in the first weeks. The manganese rejection ratio in the first week was 99.8%. As is shown in fig. 54 (bottom graph), the concentration of manganese in permeate increased from week #8, i.e., two weeks after starting the physical degradation.
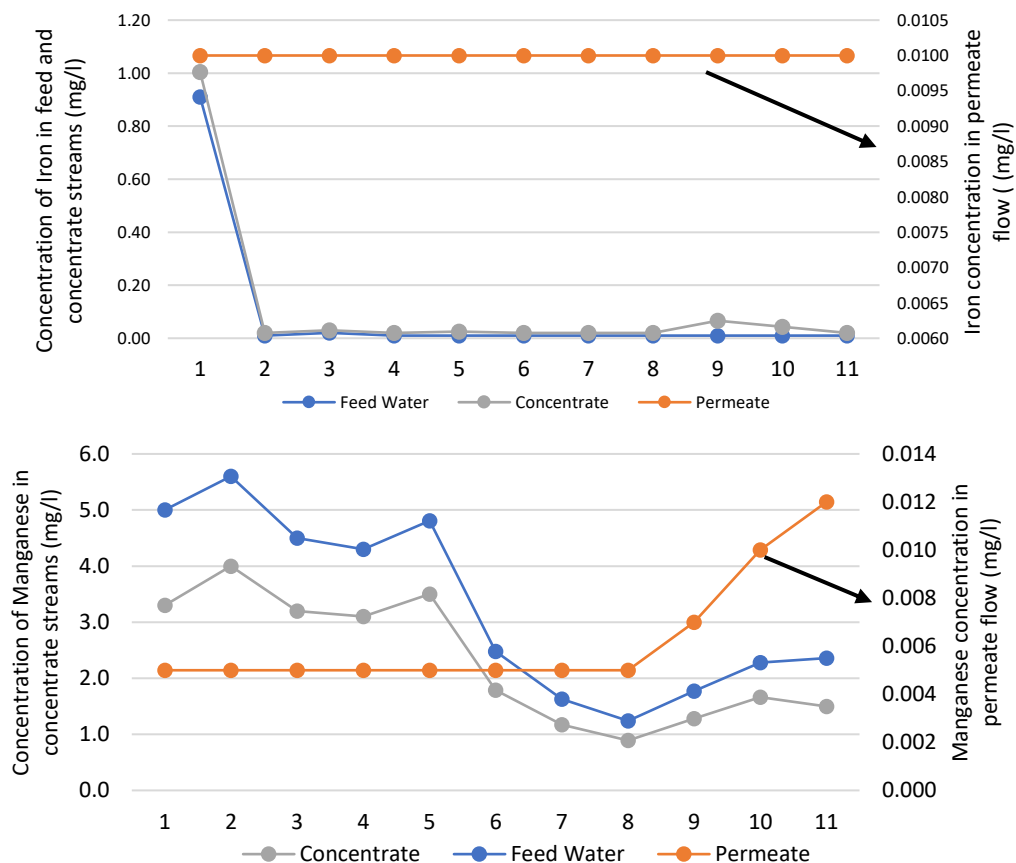
Figure 54 top: iron is entirely filtered by the pre-filtration unit. The reddish colour of the pre-filter after a few days also indicates that iron is collected by the pre-filter, and the concentration of iron in the permeate, concentrate, and feed water is almost zero after week #2. Bottom: concentration of manganese in permeate, concentrate, and feed water

This result again proves that the cracks were small in the first two weeks, and merely some dissolved ions could pass through. However, after two weeks, other ions like manganese

could also penetrate the permeate side. The rejection ratio of manganese in the last week reduced to 99.1%. After week #8, a slight increment of manganese concentration in the feed and brine stream can be observed. It shows that part of the manganese is deposited on the membrane as sediment, reducing manganese concentration in the feed water. However, after the physical degradation, part of these particles penetrates the permeate side, and as the system works in a closed loop, these particles can be found in the feed water again.

- Microbial examination results

Bacteria and viruses cannot pass through the RO membranes[181]. However, a microbial examination is performed on all samples to investigate colony formation in different water streams. The sample tubes and all sampling valves and outlets should be thoroughly disinfected to have the most accurate result. In addition, the samples should be sent at a controlled temperature, and the test should be done within 24 hours of taking the samples. In general, different microorganisms can be found in the water, including E. coli, Coliform bacteria, Ente-ro-cocci, Legionella, Clostridium perfrin-gens, and Pseudomonas aeruginosa. However, just colony count at 20°C and 36°C has been performed during the test. Although colony count does not detect the exact type of microorganisms, the results provide valuable information regarding the presence and behaviour of aerobic mesophilic germs during the operation. Furthermore, microorganisms can form biofouling on the membrane, which dramatically reduces the salt retention and permeate flux[182]. Hydrophobic and electrostatic interactions between bacteria and membrane surface are the driving force of biofouling formation, especially in hydrophobic and non-polar areas[183].

Fig. 55 shows the test result on the feed water. As seen in the first three weeks, the number of microorganisms increased remarkably. The main reason is that some of the additional chemicals added to the water are the best nutrients for the microorganisms. Furthermore, the feed tank provided a better environment for the microorganisms to grow initially. After reaching a peak value in week # 3, the colony formation decreased again.
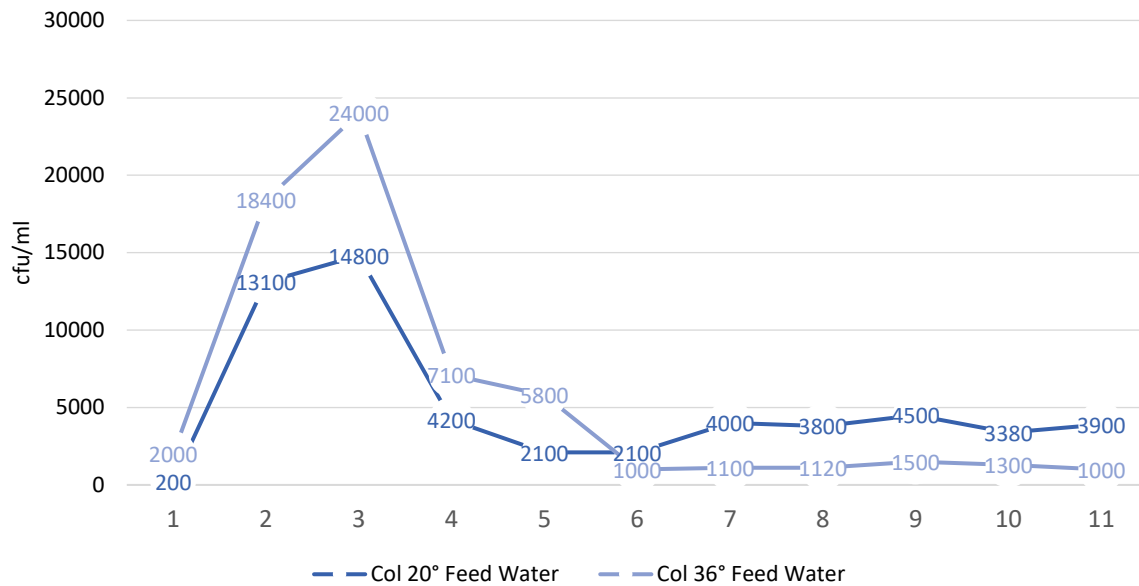
Figure 55 water samples from feed water are exposed to an incubator with standard temperatures, i.e., 20°C and 36°C, to measure the total amount of the microorganisms.

The same test with the same conditions is also carried out for the permeate and concentrate (see fig. 56). In the first four weeks, a notable amount of microorganisms was detected in the permeate water. After optimising the sampling process, including adding stainless steel valves for taking the samples and also collecting the samples ten seconds after opening the valve, the numbers reduced notably, especially in the permeate. The new process also slightly enhanced the results of feed water (see fig. 55) and the concentrate after week #4. This process also shows how sampling conditions can influence the results. Even after week #5, i.e., after the sampling improvement, some microorganisms are detected in the permeate. These values can be neglected as the process still is not wholly optimum. Particularly as the values are very small and the process is sensitive to the sampling process[184,] transport conditions and timing of the test.

5.3.1.2.   Performance of the pilot project

-    Normal Working conditions

Before investigating the system's performance under harsh conditions, first, the normal operation of the MFD technology, especially the start-up process of the system, under typical weather conditions is explained. Fig. 57 shows part of the parameters collected by the remote monitoring on a typical sunny day. Solar irradiation is increased slowly in the morning. The solar power curve is very smooth and includes no remarkable fluctuations.
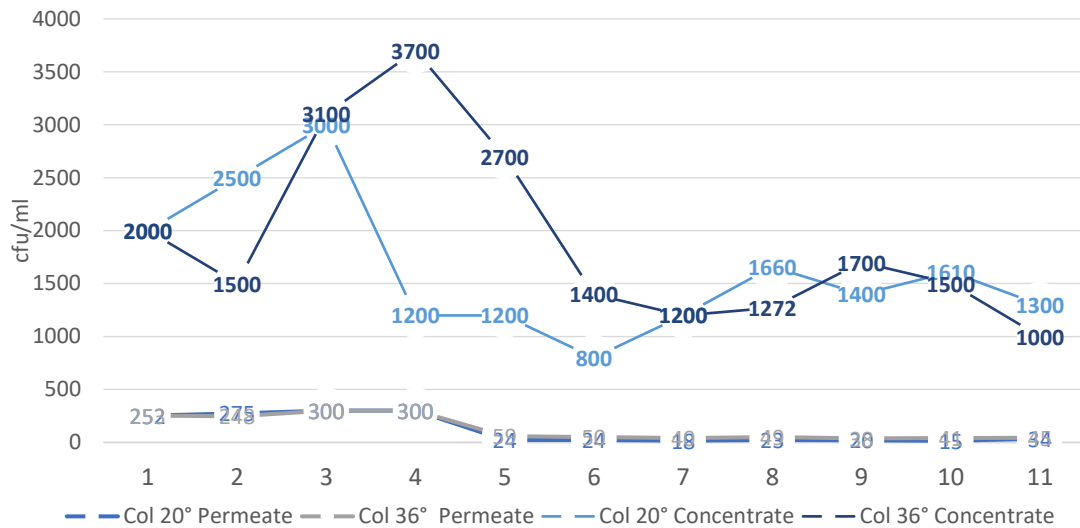
Figure 56 amount and behaviour of the aerobic mesophilic germs are measured during the test.

The control system continuously measures the solar power (see appendix 2 "Standby Case"), and as soon as solar energy is enough to start the borehole pump, i.e., 9:05 (equal to 8:05 Ghana time), this pump will be started, see point 1 in fig. 58. Shortly after starting the borehole pump, the control system detects that available solar energy would be sufficient to start the RO system if the power consumption of the borehole pump is slightly reduced. Therefore, as can be seen in point 2 in fig. 58, the control unit reduced the frequency of the borehole pump to have enough energy available to run the RO unit simultaneously. The period between starting the borehole pump and the RO unit depends on the increment ratio of solar energy and the water level in the feed water tank.

Figure 57 start-up process of the pilot project in Ghana on a typical sunny day.
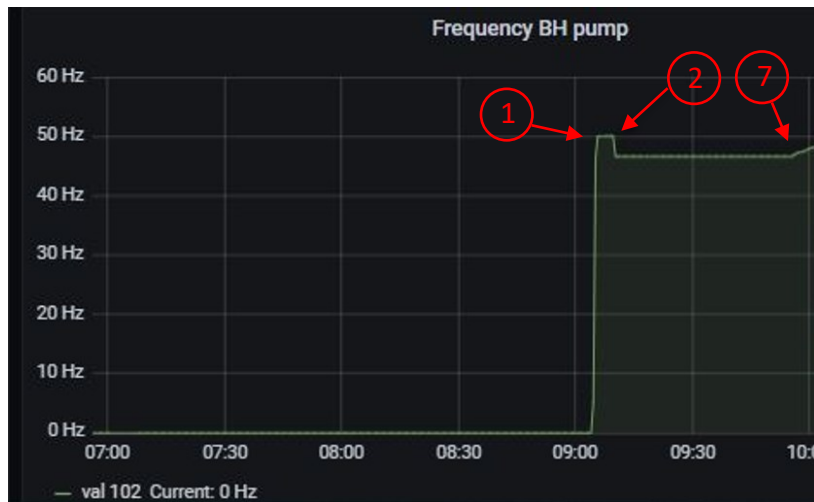
Figure 58 the borehole pump automatically starts every morning as soon as the V_{DC} from solar panels is higher than $V_{PV\ min}$. The control unit adjusts the frequency of the pump to have the highest performance efficiency.

When there is sufficient energy, the control system runs the RO unit. First, the feed pump will be started to provide enough feed pressure, see point 3 in fig. 59. Afterward, the high pressure will start at the minimum frequency, see point 4 in fig. 59. As the priority of the system is to maximise water production, by increasing the solar energy, first, the frequency of the high-pressure pump will be increased, see point 5. At the same time, the control unit continuously adjusts the frequency of the feed pump to avoid cavitation in the high-pressure pump, see point 6. Details of start-up process are explained in appendix 2 in "start-up case".

Figure 59 the control system adjusts the frequency of all pumps to optimize energy sharing and maximize water production.

When the high-pressure pump and feed pump reach their maximum operation point, i.e., 50 Hz, then the control system increases the frequency of the borehole pump, see point 7 in fig. 58. The same steps are used in the evening to turn off the system.

- Performance of the pilot project under dynamic condition

Solar radiation, which is received by the PV panels, varies continuously due to many factors like the appearance of patches of clouds, accumulation of water droplets and dust particles

in a particular section of the atmosphere, and changes in air density with temperature and humidity. The most prominent factor affecting the solar panel's output is due to the appearance of clouds. In almost all seasons, the appearance and disappearance of patches of clouds are so frequent that solar PV output suffers large fluctuations in voltage and current. To investigate the behaviour of the system under dynamic conditions, the data of a cloudy day, June 9th 2021, is selected as the solar irradiation has a low value in the morning due to the heavy clouds. In addition, solar power significantly fluctuates in the morning, especially between 10:00 and 11:00 a.m. The system faced harsh power fluctuations in midday as clouds were passing the sky. Fig. 60 shows the solar curve of this day.
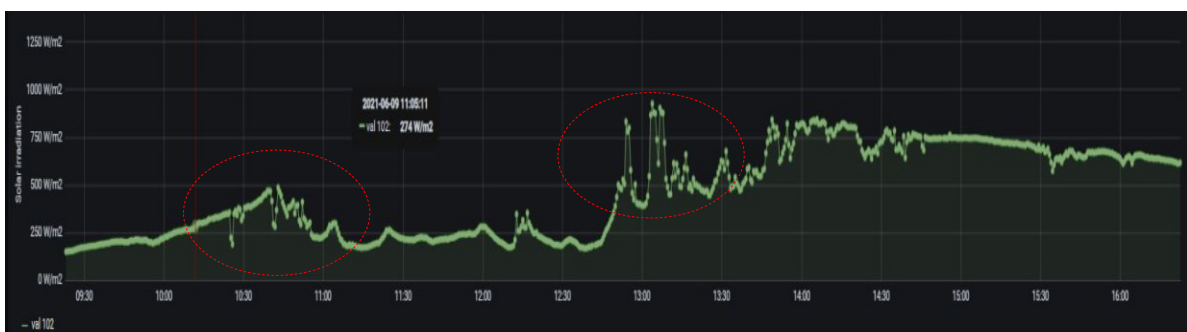
Figure 60 remote monitoring data showed harsh working conditions on June 9th 2021. In the morning, PVRO receives low and fluctuant solar power, followed by remarkable fluctuations in the midday.

Fig. 61 shows the behaviour of the system under such circumstances. By morning, when the irradiation is only 250 W m^{-2} (25% of the maximum irradiation), both feed and high-pressure pumps work with approximately the highest frequency. Both pumps simultaneously compensate for the fluctuations by varying the frequency between 50 and 40 Hz. The last graph in fig 61 shows the permeate flux. It confirms that although solar irradiation is only 25% of maximum irradiation, including all fluctuations, the water production stayed almost the same with the average value of 5.2 L min^{-1}, which is just 35% less than the maximum production capacity of 8 L min^{-1}.

As a result, these graphs prove that the control system managed to follow the solar curve in real conditions, and by adjusting the frequency of the pumps, the MFD technology could run the system continuously and without any interruption in water production, even in very low solar irradiation. Furthermore, despite the high frequency fluctuations in the feed and high-pressure pump, the water production curve is totally smooth, which confirms that membranes are not facing any pressure shock or flux variation.
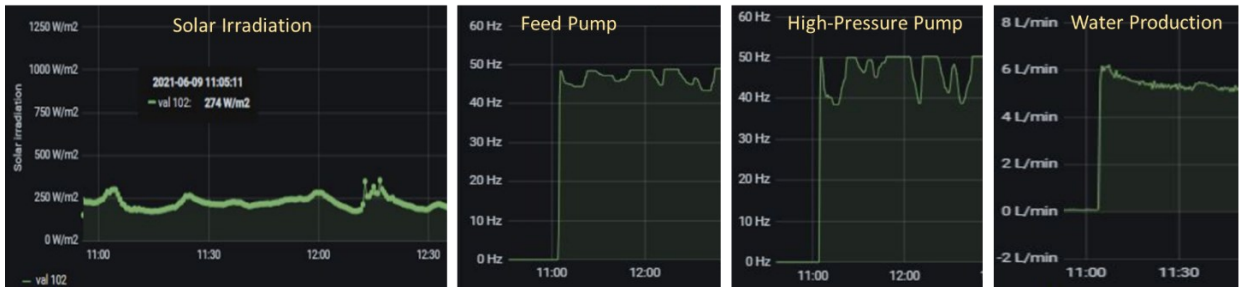
Figure 61 the control unit adjusts the frequency of the pumps to compensate for the energy fluctuations. However, the changes in frequency do not affect the working pressure of the system and permeate flux curve is totally smooth.

The other challenging condition on this specific day happens midday when clouds pass through the sky, which causes significant energy fluctuations. The second generation of PVRO systems will face the risks of many emergency shutdowns in such circumstances. These shutdowns, which will happen at least once per day, pose the risk of technical damage for the mechanical parts like pumps and dramatically reduce the lifespan of the membranes because membranes are highly sensitive to pressure fluctuations.

As it is shown in fig. 62, the solar energy curve faces a significant irradiation decline around 13:10 from 900 to 400 W m^{-2}. Almost the same reduction ratio is simulated for the test bench. Despite facing such a sharp energy decline, the graphs of the feed and high-pressure pump show a constant operation at the maximum point, i.e., 50 Hz. It proves how the control system can stand against fluctuations and compensate for fast energy drops. In addition, as there is no fluctuation in the pump frequency and subsequently in the pump pressure, the water production curve is perfectly smooth and stable. Therefore, no physical damages can be caused by dynamic operation of the PVRO.
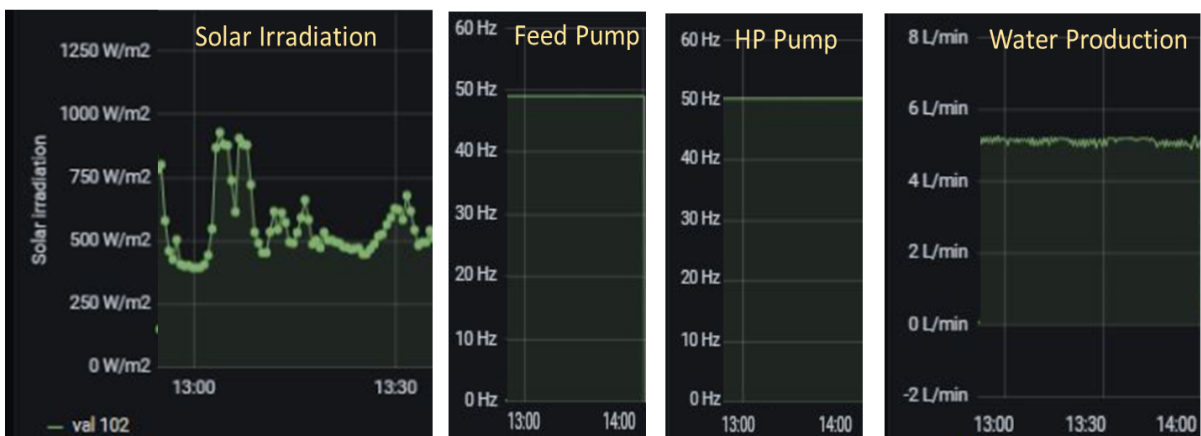
Figure 62 performance of the system under sharp energy reductions.

However, according to the results from the water analysis in the previous section, to some extent, physical degradation was observed in week #6. To investigate the reason and find

91

more details, in the next section, the microscopic investigation is performed on the membranes for both the test bench and the pilot project.

5.3.1.3. Membrane characterization

The membranes are autopsied and analysed to investigate the morphology of foulants and scalants and determine the chemical or mechanical damages that could potentially occur during the dynamic operation of the systems.

Tran et al. proved that the composition, structure, and evolution pattern of scaling is uneven on the surface of the membranes[185]. To have more accurate data, microscopic images from the top surface of the membrane, the inner side, and the cross-section are taken and investigated. This investigation is necessary because performance analysis and water quality investigation only can show the initiation of fouling. However, imaging and visualization is the best method to study the origin, development and physico-chemical properties of fouling or scaling[186,187,188]. For the autopsy and tests, one membrane from the first stage and one from the last stage is removed (see fig. 63) since:

i. The first membrane in the system will face the highest volume of suspended solids.

ii. The last membrane in the system receives water that has been concentrated in the previous stages and has the highest scaling potential.

iii. Biological fouling and organics can be found on all membranes in the system. However, hydrophobic bacteria tend to attract to the membrane surface, which is also slightly hydrophobic. Therefore, biofouling always is worst at the first membrane, where the bacteria stick to the first available hydrophobic surface. On the other side, humic acids are hydrophilic at non-acid pH levels. They can spread evenly throughout the last membrane and create a more adhesive foulant layer[189]. Because due to the high hydrophobicity, a strong membrane-foulant interaction forms between humic acids and the active layer[190].

iv. Suspended solids and precipitated metals (such as iron) can precipitate on any membrane in the system. Therefore, if suspended solids such as limestone particles are found in the last membrane, this data should be compared with the first membrane. Otherwise, it would be difficult to conclude any result.
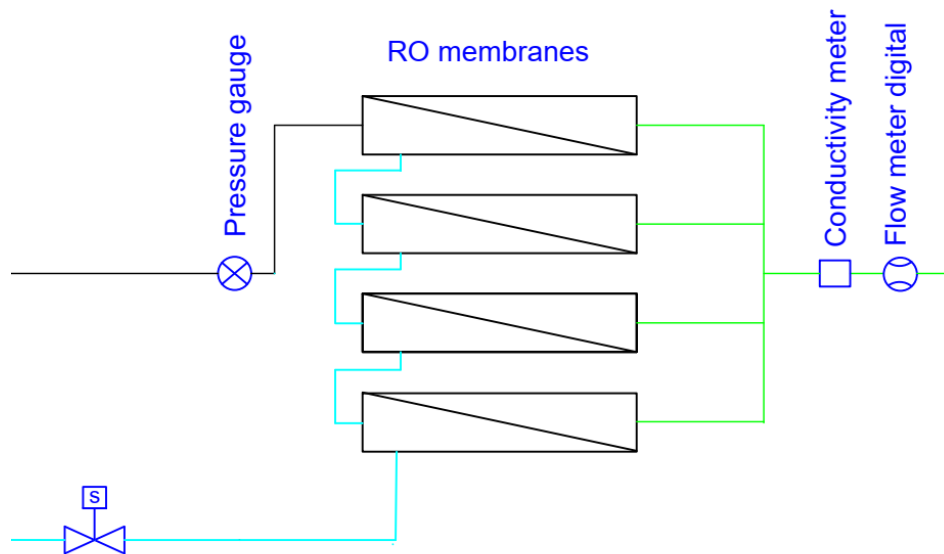
Figure 63 the membranes are connected in series (the structure is the same for the pilot project and the test bench). As shown in the picture, the brine of the first membrane is used as the feed of the following membrane. Therefore, the first membrane faces the highest suspended solids, and the last membrane is exposed to the highest salinity in the feed water.

Fig. 64 shows the cross-section cut of the first membranes of both systems, i.e., the test bench and the pilot project. The membrane of the pilot project got more suspended solids as feedwater source is a real borehole and continuously pumps sand and other particles to the surface, while the test bench works in a closed loop. The pilot project started earlier than the accelerated test bench, and the system ran for twelve months before removing the membrane. The test bench was running for four months, simulating 16 months of regular operation. Therefore, both membranes have almost the same working age.

Figure 64 cut cross-section of membranes from the first stage. Left: the membrane from the test bench after four months of running, equal to 16 months of regular running. Right: the membrane from the pilot project in Cape Coast is removed from the system after twelve months of working.

The samples were cut from the wound and rolled membranes to approximately 1x1 cm pieces, then dried at 105 °C and stored in a desiccator over a desiccant. The sample was taken as far as possible from the strands of the membrane feed spacers to have more comprehensive insights about fouling. Principally, feed spacers are used in the membrane structure to enhance the eddy mixing, which leads to higher mass transfer and, subsequently, less concentration polarization within the whole membrane[191]. However, higher particle precipitation can occur in the vicinity of the feed spacer strands[192].

The scanning electron microscope (SEM) images were taken using a Gemini SEM 300 (serial number 8202017062 from Carl Zeiss Microscopy GmbH). Fig. 64 shows the SEM images of the samples. The images are taken at the Forschungsinstitut Edelmetalle und Metallchemie (FEM)[14] as the project partner, and the project was jointly financed by FEM, Grino Water Solutions GmbH and Deutsche Bundesstiftung Umwelt (DBU)[15].
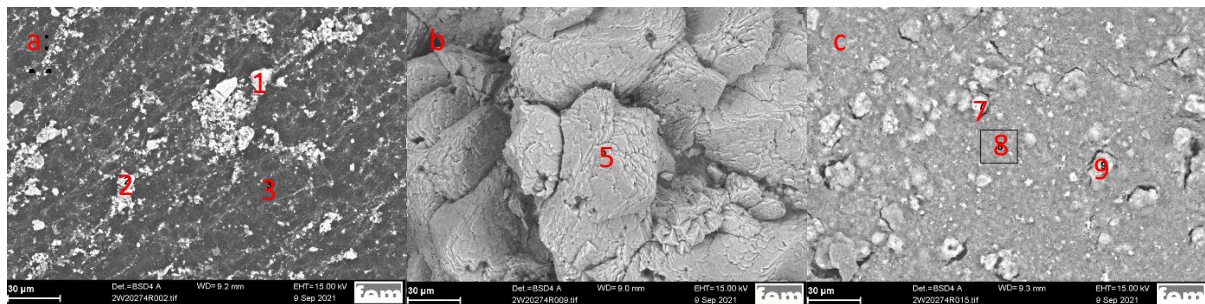
Figure 65 SEM images from: (a) the first membrane of the test bench Membrane, (b) the last (4th) membrane of the test bench, and (c) the first membrane from the pilot project. The images are taken at the Forschungsinstitut Edelmetalle und Metallchemie (FEM).

The images show that a considerable coating layer is formed on all membranes. As shown in Fig. 65 (a), a complete coating of amorphous material is interspersed with probably crystalline particles. Crystalline layer on top is formed because of the bulk crystallisation mechanism (homogeneous nucleation), which is a porous and incoherent cake layer. While the amorphous layer may be attributed to the surface crystallisation (heterogeneous nucleation) and forms a coherent layer[193,194]. The cake layer leads to higher hydraulic resistance, and surface crystallisation mainly blocks the active layer and enhances further scaling.

In contrast, fig. 65 (b) shows exclusively crystalline structures over the entire surface of the membrane. Because the first membrane trapped all coarse suspended particles, such as

---

[14] https://www.fem-online.de/en/content/institute
[15] https://www.dbu.de/projekt_35511/01_db_2409.html

organic material or rust particles. On the other hand, this membrane, i.e., the last membrane, is only exposed to the "processed water" of the other stages, which has the highest salt concentration. Further water separation in this membrane significantly increases the solubility value of the inorganic salts, which initiates the crystallization.

The image of the first membrane from the pilot project (Fig. 65 (c)) shows a similar result to the first membrane from the test bench, a two-dimensional coating with an apparently amorphous substance interspersed with crystalline particles.

Furthermore, to have a better understanding of the chemical characterization of the layers, Energy-Dispersive X-ray spectroscopy (EDX) has been done. EDX detector (X-Max 150 serial 74553) is used for the spectroscopy, and INCA software from Oxford Instruments GmbH is applied to analyse the data. The analysed points are marked in fig 65.

The EDX data proved the hypothesis from SEM images. Actually, the spectra of the first membrane show high values of oxygen and iron in the EDX (see fig. 66, top and middle images) for the crystalline areas (see points 1 and 2 in fig. 64). For the amorphous areas (see point 3 in fig. 65) high carbon and calcium contents are recognized (see fig. 66, bottom image).
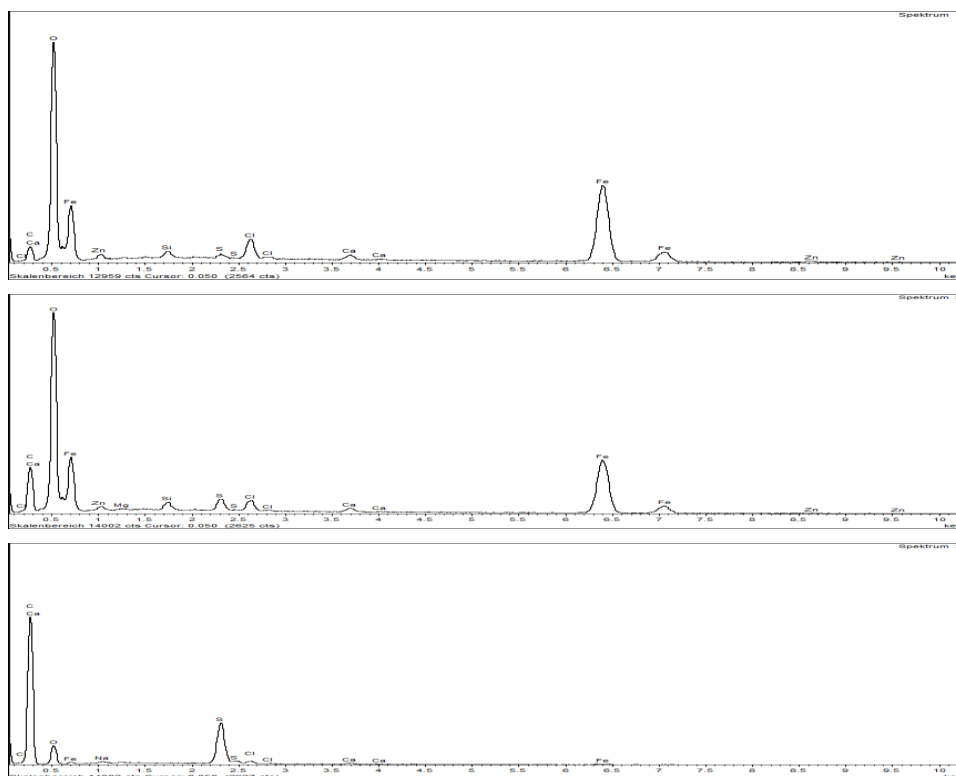
Figure 66 EDX spectra from the first membrane of the test bench. Based on the surface structure, Three points are selected, which are pointed in the SEM image (points 1, 2, and 3 in fig. 65). The images are taken at the Forschungsinstitut Edelmetalle und Metallchemie (FEM).

The organic and biological particles probably contribute to the development of carbon and oxygen peaks. Organic matters can be absorbed by calcium, as a multivalent ion, due to the electrostatic repulsion/attraction[195]. Therefore, the foulant-foulant chemical bonding interaction is the dominating scaling mechanism in this membrane.

As shown before, a major part of the iron is settled on the cartridge pre-filters. However, EDX depicts that iron could partially reach the first membrane. Even the CIP methods (Clean In Place) might not be able to eliminate the iron residue due to the creation of an irreversible fouling layer on the membrane[196]. EDX also shows a small amount of Cl and S. Probably, the chloride peak is formed because dissolved Cl ions are trapped in the scaling layers. While, sulphur could be detected because of the polysulphone layer of the membrane, as it can be lifted to the fouling layer. EDX values of thicker layers can prove if S was part of the fouling layer or just lifted parts of the membrane. The values of other elements like Mg, Si, and Zn are negligible.

Fig. 67 provides a more vivid view of the crystalline and amorphous areas on the surface of the membrane. It can be estimated that crystalline particles are enormous compared to the amorphous layer. A cross-section view would be advantageous.
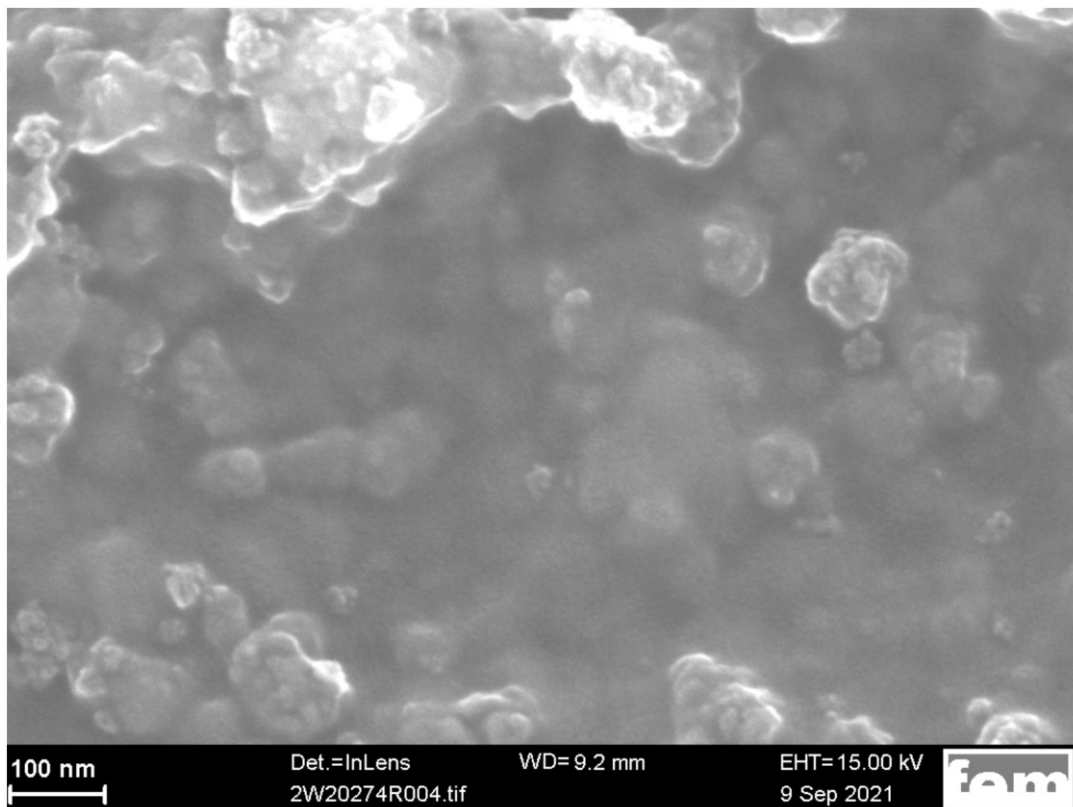
Figure 67 SEM images from the first membrane of the test bench Membrane with better insights about the fouling components and areas. The images are taken at the Forschungsinstitut Edelmetalle und Metallchemie (FEM).

In this thesis, the interior side of the membrane was also investigated to understand better the fouling or scaling layer on the permeate side. Fig. 68 shows the SEM and EDX images from the membrane pores from the inside.
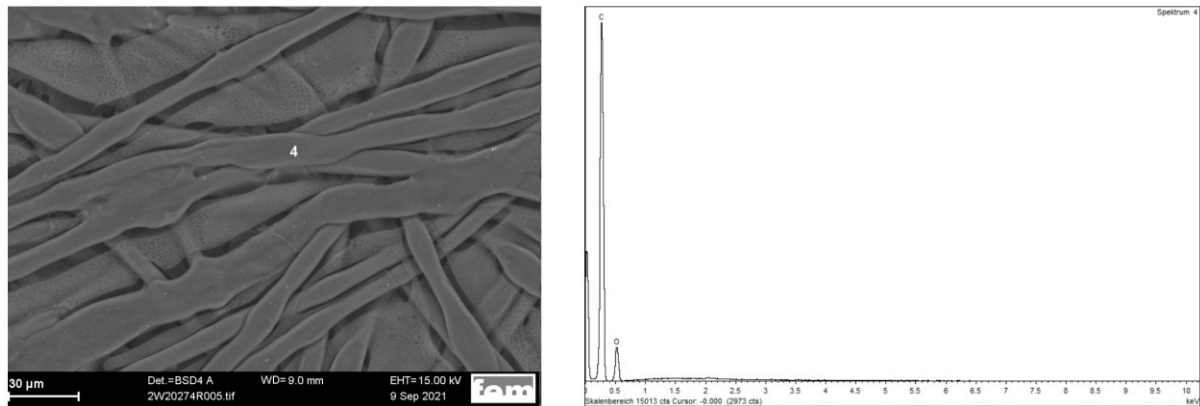
Figure 68 SEM and EDX images from the permeate side of the first membrane of the test bench Membrane. The images are taken at the Forschungsinstitut Edelmetalle und Metallchemie (FEM).

Finding the cracks or any physical damage on the interior side is improbable. However, the SEM image also shows a typical structure of the pores. Furthermore, the EDX shows that all big particles like iron and silicon are entirely removed, and small items like carbon and oxygen could reach this internal layer.

The situation is different for the fourth membrane of the test bench. As mentioned before, this membrane is exposed to the "processed water" of the other stages. Therefore, as the main part of natural organic matter (NOM), suspended solids and dissolved ions are already filtered, the EDX spectrum from the membrane's surface depicts very high calcium values in combination with high signals of oxygen and carbon. In addition, the strong crystal formation proves that lime deposition has accrued on the membrane surface (see Fig. 65) and fig. 70 shows how this lime layer is spread on the membrane surface.
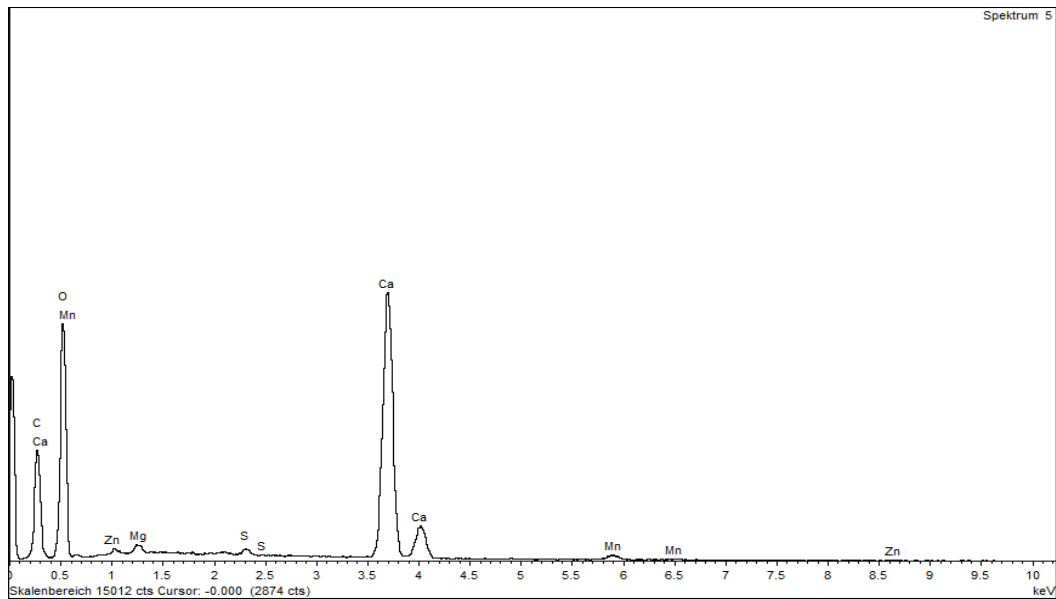
Figure 69 EDX spectra from the last membrane of the test bench. The image point is shown in the SEM image (point 5 in fig. 65). The images are taken at the Forschungsinstitut Edelmetalle und Metallchemie (FEM).
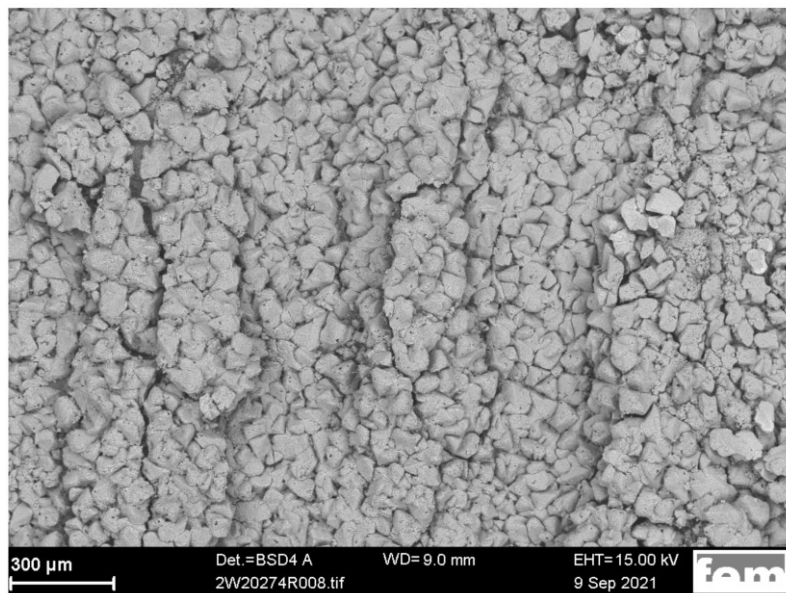
Figure 70 a uniform lime layer is spread on the surface of the last membrane of the test bench. The images are taken at the Forschungsinstitut Edelmetalle und Metallchemie (FEM).

Although the structure of the fouling layer on the surface of the first and last membrane is entirely diverse, the images from the permeate side are pretty similar. The pores' structure is normal, and almost all ions and particles are retained (see fig. 71).
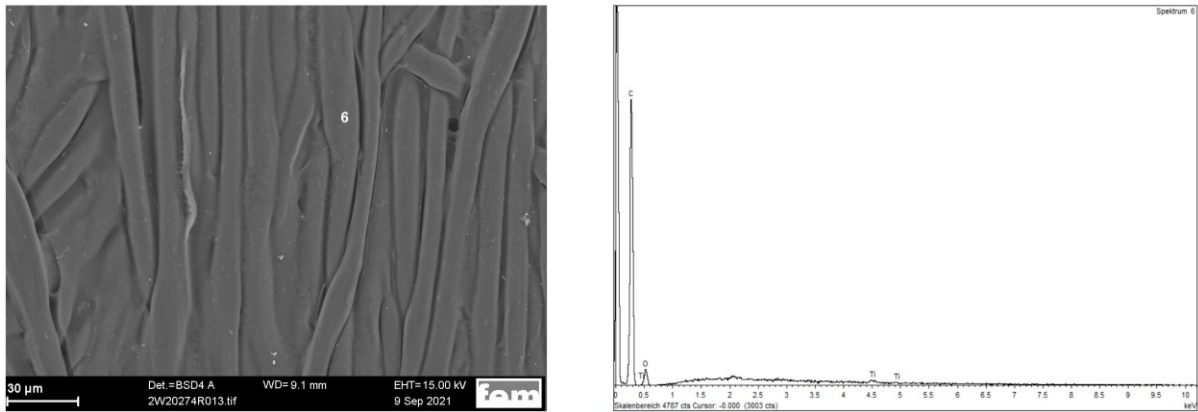
Figure 71 SEM and EDX images from the permeate side of the last membrane of the test bench Membrane. The images are taken at the Forschungsinstitut Edelmetalle und Metallchemie (FEM).

The EDX results of the membrane of the pilot project are depicted in fig. 72 shows a similar picture to the corresponding membrane from the test bench. In addition to the iron and oxygen signals, there are also remarkable signals of aluminium, manganese, and silicon. This is probably due to the seasonal changes in the borehole water during the one-year operation of the system. Also, silicon signals are higher because borehole water contains a significant amount of sediment particles, such as sand, which apparently pass through the pre-filters. As this is not the case in the test bench, the silicon signals are not that significant in the EDX spectrums of the membranes of the test bench.
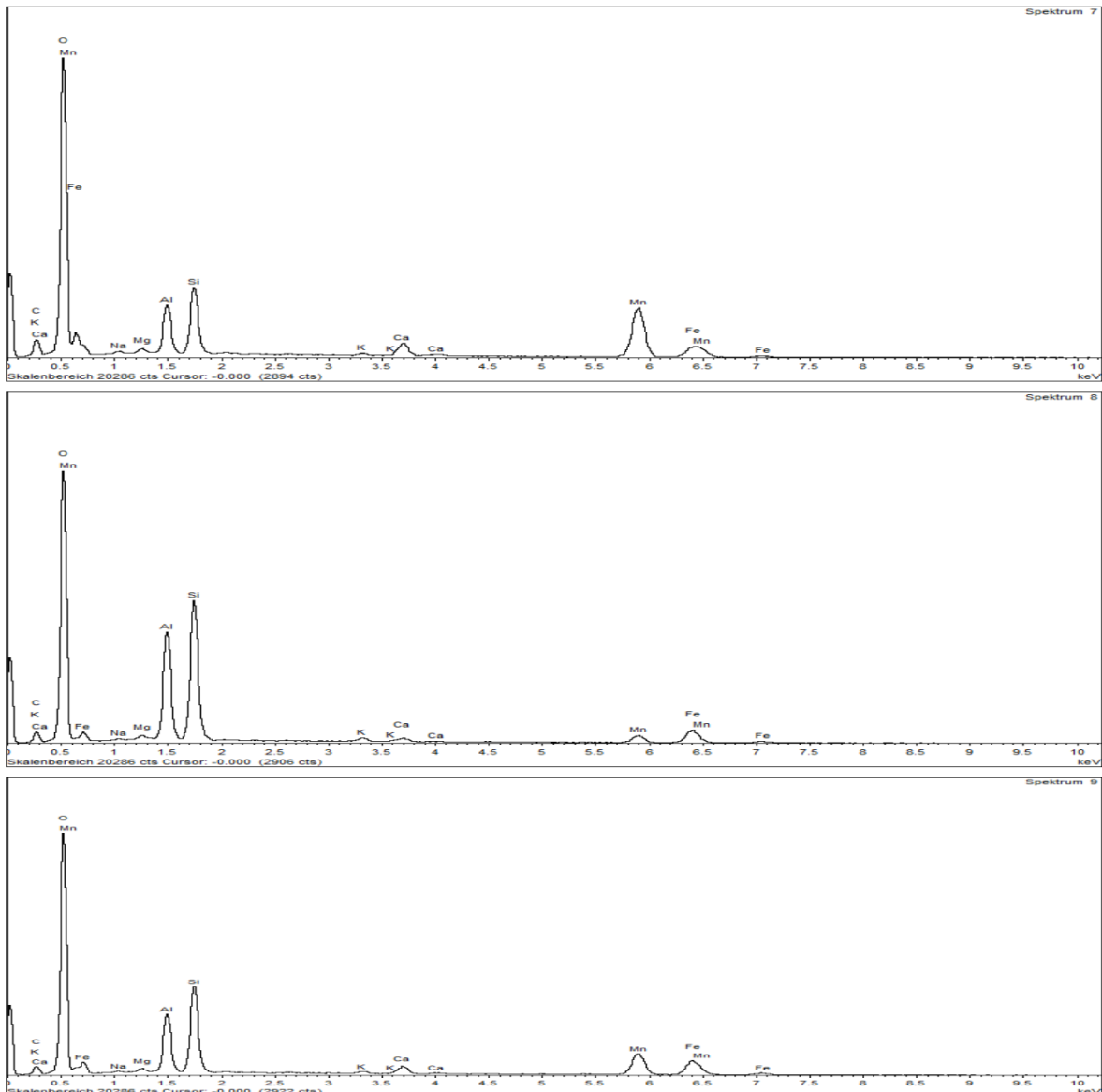
Figure 72 EDX spectra from the first membrane of the pilot project. The image points are shown in the SEM image (points 7, 8, and 9 in fig. 65). The images are taken at the Forschungsinstitut Edelmetalle und Metallchemie (FEM).

Despite the more severe fouling situation on the surface of the membrane, the EDX spectrum of the permeate side is quite similar to the test bench results. It proves that the scaling or fouling layer does not form on the permeate side, or at least not after one year of operation. However, the SEM image shows some deformation in the membrane pores. Actually, scaling on the surface and physical degradation are the main issues of the membranes (see fig. 73). To have better insights and more details about the layer formation on the surface of the membrane, metallographic electronic microscope images are taken from the cross-section of all investigated membranes, i.e., the first and the last (4th) membrane of the test bench and the first membrane from the pilot project.
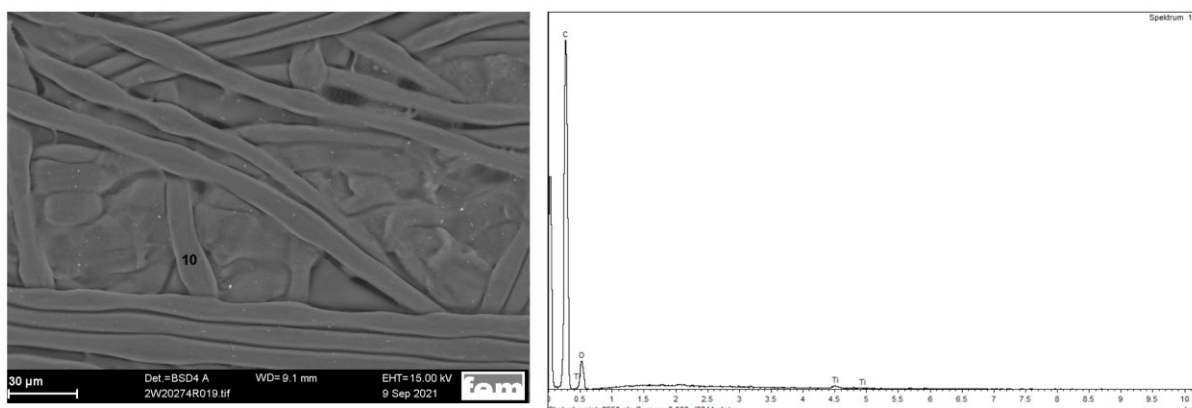
Figure 73. SEM and EDX images from the permeate side of the last membrane of the pilot project. The images are taken at the Forschungsinstitut Edelmetalle und Metallchemie (FEM).

Metallographic electronic microscope images are common for investigating the performance of the membranes[197]. However, a few studies have investigated the cross-section, while these images can provide better insights into the kinetics and mechanisms of fouling. In fact, the combination of surface imaging and cross-section investigation provides a comprehensive and, to some extent, a 3D understanding of scaling development on the membranes.

Fig. 74 shows the microscope images of the first membrane from the test bench. A skinny layer (less than 10 µm) of amorphous material is formed on the top of the membrane. Furthermore, some physical deformation in the pores structure is visible. The first membrane faces the highest pressure and mainly exposes to pressure fluctuations as the first element.
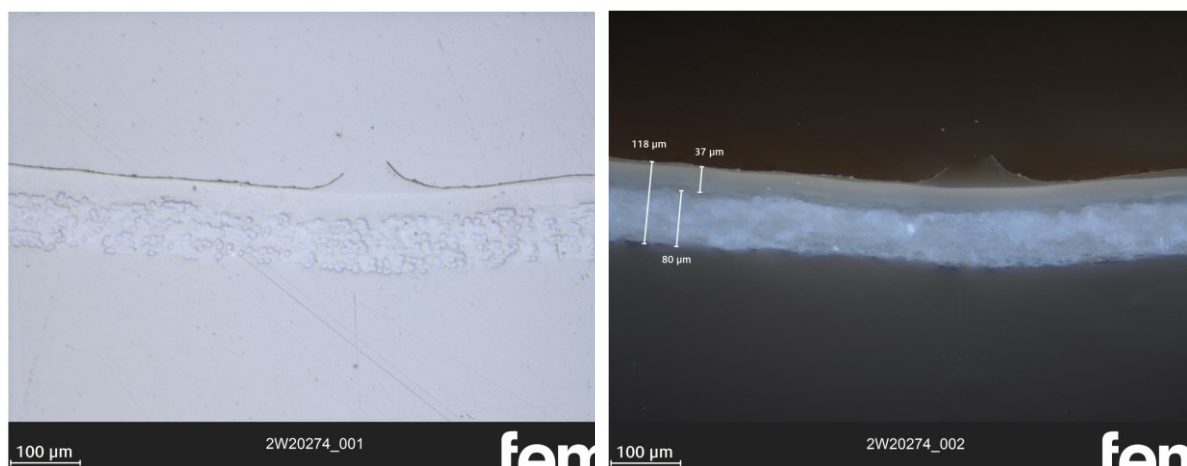
Figure 74 metallographic electronic microscope images of the first membrane of the accelerated test bench. Left: brightfield image, right: darkfield image. The images are taken at the Forschungsinstitut Edelmetalle und Metallchemie (FEM).

The images of the last membranes (see fig. 75) are more interesting as they clearly prove the interpretations of SEM and EDX investigations. A relatively thick layer of the crystallized particle is formed on the top of the membrane. The average height of crystals is about 22 µm, and more giant crystals with about 137 µm are also visible in the image. It seems that layers

are not mixed. Therefore, it can be concluded that the first layer formed earlier, and then the second layer occurred on the top. In addition, the membrane pores are more uniform, and there are fewer gaps, assumably due to the less physical burden on the last membrane.
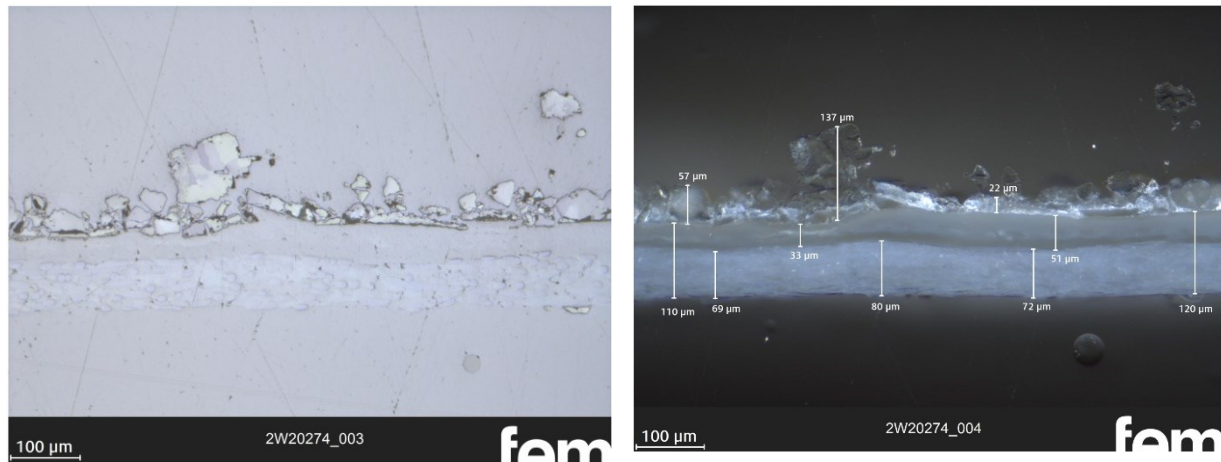
Figure 75 metallographic electronic microscope images of the last membrane of the accelerated test bench. Left: brightfield image, right: darkfield image. The images are taken at the Forschungsinstitut Edelmetalle und Metallchemie (FEM).

The images from the membrane of the pilot project are shown in fig. 76. These images also agree with the SEM and EDX results. There is a thin coating layer directly on the membrane surface, and on the top, there is a very compact crystallised layer of different components. According to EDX spectra, this layer includes iron, oxygen, aluminium, manganese, and silicon.
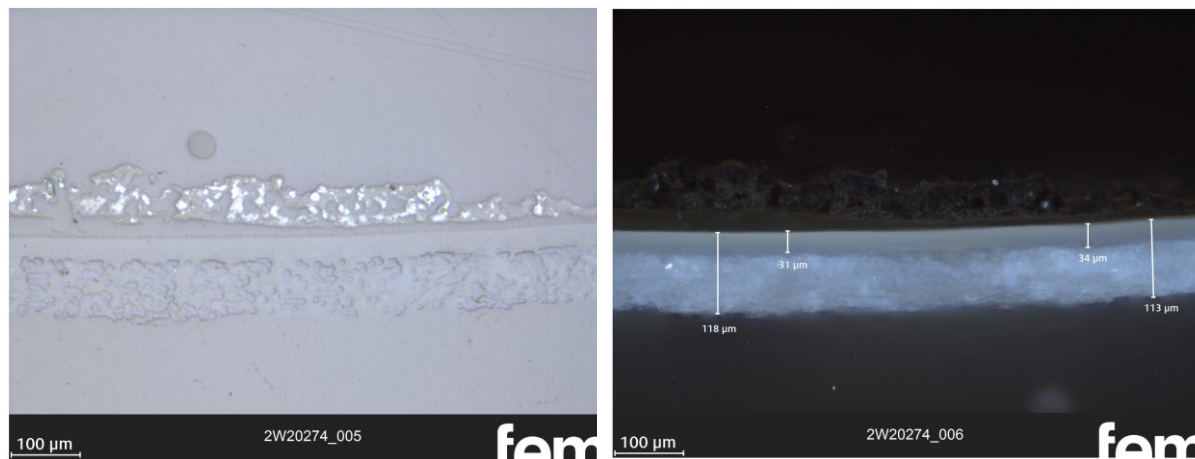
Figure 76 metallographic electronic microscope images of the last membrane of the pilot project in Ghana. Top: brightfield image, bottom: darkfield image. The images are taken at the Forschungsinstitut Edelmetalle und Metallchemie (FEM).

5.3.2. Improving the system

As shown in fig. 50, the TDS of permeate stream is increased from 75 microS/cm to 242 microS/cm, especially the increment is more remarkable in the first cycles. Although this increment is negligible and the TDS value is still far below the WHO guidelines for drinking water, the idea was to find a potential solution to improve the system. Results of SEM images

and EDX spectra proved that this decline in water quality is mainly because of forming a remarkable coated layer of fouling and scaling on the surface of the membrane. In addition, the water analysis showed a physical degradation in the membranes after week #6. Fouling and scaling are the common drawbacks of RO systems, and dynamic operation could not necessarily be the reason for this problem. Therefore, the next step is planned to reduce the scaling and fouling by improving the pre-filtration system. This step is crucial as:

1- System performance can be enhanced by increasing the effectiveness of the pre-filtration. Therefore, it can be proved that the scaling and fouling were formed due to the pre-filtration efficiency, and actually, the dynamic operation did not cause further degradation.

2- Since the accelerated test bench operates in a closed cycle, chemical anti-scaling cannot be dosed to the feed water. The concentration of anti-scalant will double with each cycle as the brine returns to the tank. Furthermore, anti-scalant, in most cases, contains a high amount of phosphate, which leads to faster growth of the microorganisms in the tank.

Therefore, a metal catalyst would be more proper for the test conditions. In addition, this kind of pre-filtration is more environmentally friendly than conventional anti-scalant systems, as anti-scalant contains some amounts of biocides, which at the end will be released to the environment with the brine stream. In general, metal catalysts are more expensive, but they can reliably reduce biofilms and Legionella. For this study, a metal catalyst made of nickel, chromium, iron and an optimally matched mineral layer from MolKat company is used. This catalyst can be easily added to the piping system and should usually be installed before cartridge filters. Fig. 77 shows the picture of the catalyst added to the pre-filtration system of the test bench.

After improving the pre-filtration, new membranes were installed in the first and last vessels as the membranes were removed for autopsy. The second and third membranes were kept on the test bench to be operated for a longer time. Then the test bench was operated under the same working conditions (see section 5.2.2) for additional four months. System performance was monitored to compare the results, SEM images were taken, and an EDX investigation was carried out.

Figure 77 MOL®LIK SW30 is used to improve the pre-filtration system of the test bench.

Figure 78 illustrates the system performance during the fluctuation phase, i.e., when the frequency is decreased from 50 Hz to 40 and 30 Hz. In order to avoid any orderly data collection, the data were extracted randomly. The values from the second test phase showed that in dynamic circumstances, the control system could keep the water quality and just by adjusting the frequency of the pumps, the system could continuously produce drinking water without any adverse effect on the operation.
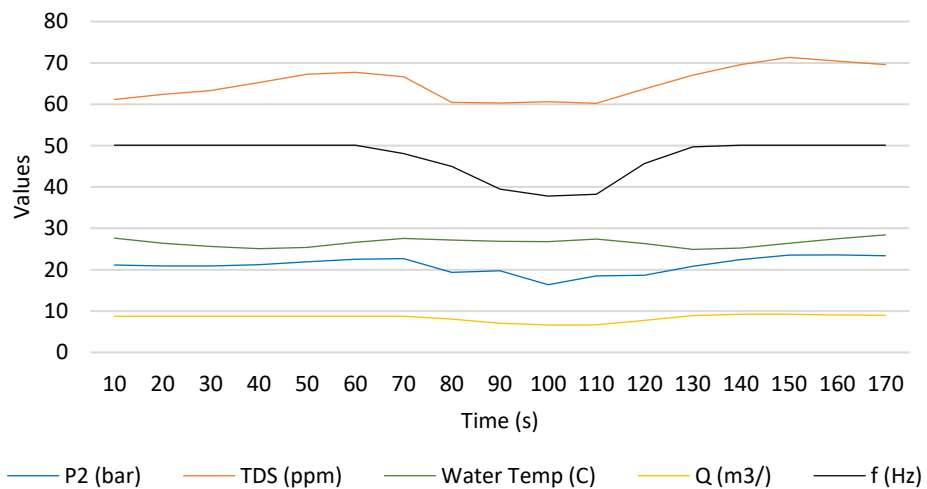
Figure 78 the average values are collected from different properties of four samples in the fluctuation phase of the second round of the test.

Figure 79 and table 14 show the system performance under dynamic operation after the second 4-month tests. The samples are taken at 50 Hz when the system is stable to neglect other variations. The initial TDS value is higher compared with the first phase, but it stays at almost the same value during the whole four months. The higher initial value is due to keeping two old membranes from the last round. However, other factors like flowrate, pressure, and temperature stay constant and prove the success of the dynamic operation.
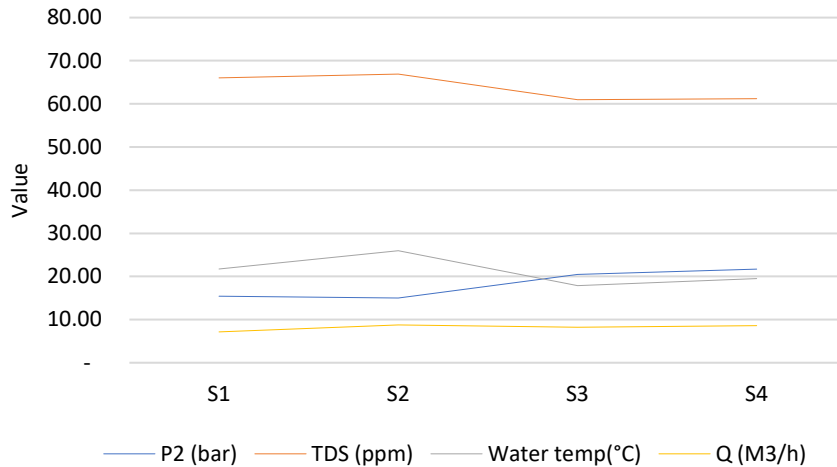
Figure 79 all properties during the second four-month operation under dynamic operation and after improving the pre-filtration system.

Table 14 The operation parameters during the second phase of the test.

	P2 (bar)	TDS (microS/cm)	Water temp(°C)	Q (M3/h)
S1	15.4	103	21.73	7.15
S2	15.0	105	26.0	8.8
S3	20.5	95.3	17.87	8.22

5.3.3. Analysis of SEM images

To identify the specific foulants and scalants on the membrane and to determine the chemical or mechanical damage that occurred during the second phase, the first and last membranes were removed to take SEM images. The same membranes are selected to compare the results with the first phase. Cutting, drying process and preparation are similar to the first phase.
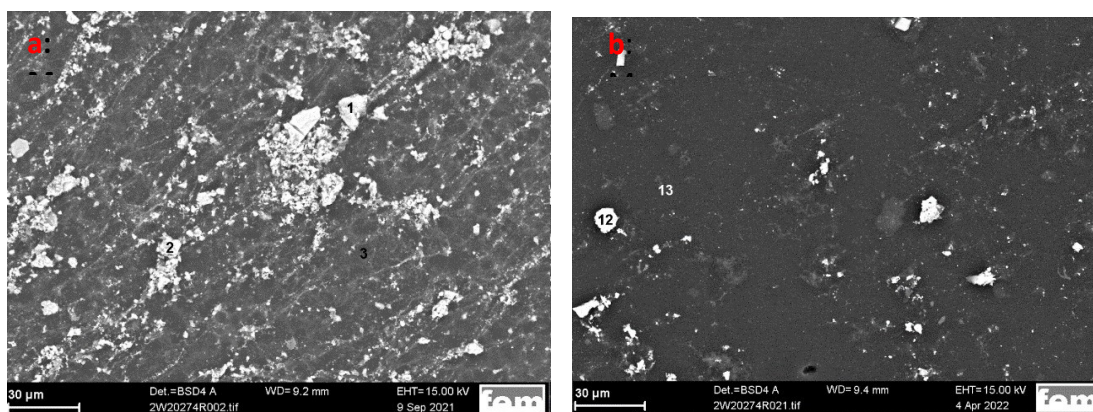
Figure 80 comparison of membranes situation using SEM images: (a) SEM image of the first membrane at the end of the first test round, (b) SEM image of the first membrane at the end of the second round.

Fig. 80 compares the SEM images of the first membranes from the first and second rounds. The SEM image of the membrane from the second round shows fewer inorganic particles on the coating layer compared to the first round. It proves that the metal catalyst can effectively

105

remove inorganic particles. Based on the results from the first round, these particles are mainly iron which is oxidised or corroded and settled on the membrane surface. EDX investigation is also carried out, and as shown in the EDX spectrum, a high value of carbon is detected on the surface of the membrane from the second round (fig. 81 right). Therefore, it proves that an organic amorphous coating layer is formed on the membrane.
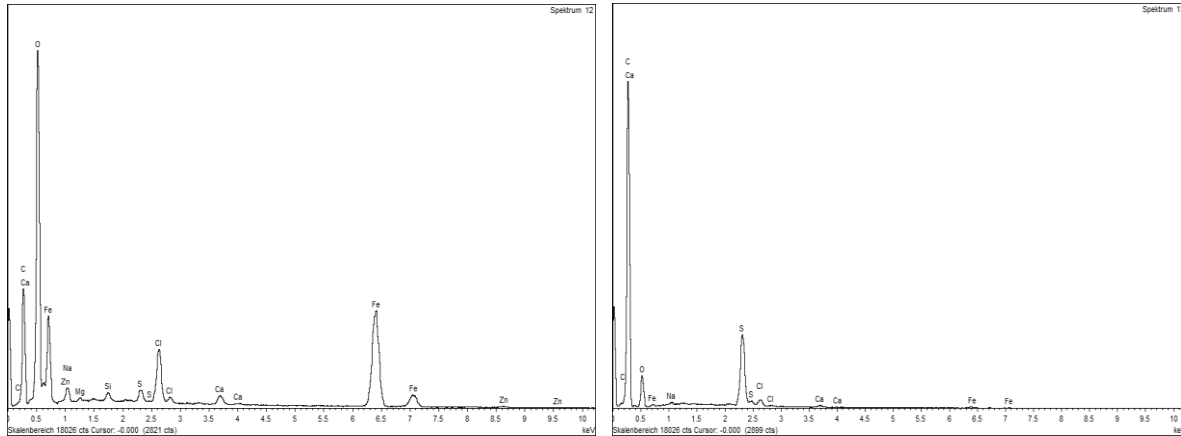
Figure 81 EDX spectra form the first membrane after the second round of the test. As it is marked in the SEM image (fig. 88 right), two points with different structures are selected to take the images, i.e., points 12 and 13.

The SEM images of the fourth membrane shows a remarkable difference. Fig. 82 compares the images from the first and second rounds. In contrast to the first round, the membrane in the second round does not show a complete coating with inorganic crystals. Instead, the coating is very similar to the image of the first membrane of the second round. A mixture of organic coating with isolated inorganic particles is visible (see fig. 82 right).
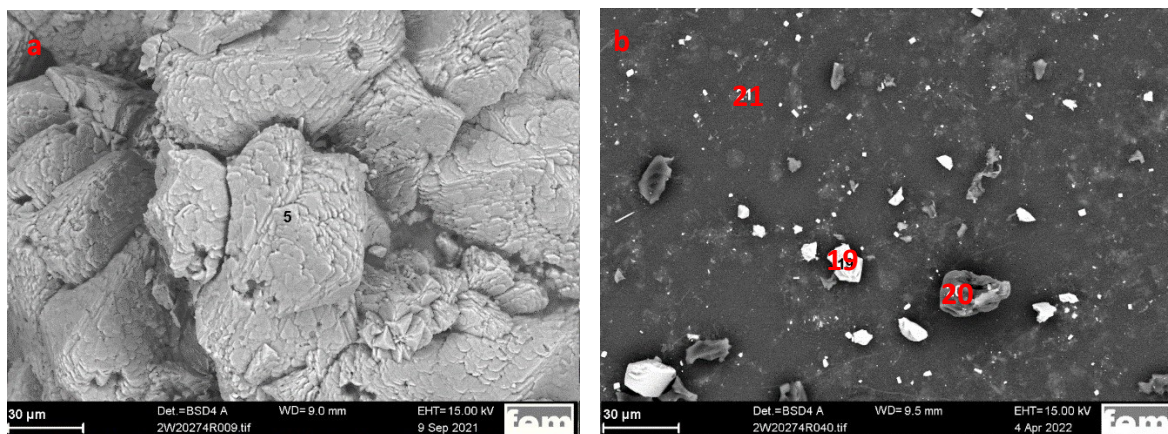
Figure 82 comparison of membranes situation using SEM images: (a) SEM image of the last membrane at the end of the first test round, (b) SEM image of the last membrane at the end of the second round.

Fig. 83 shows the EDX spectrums of three selected points, marked as points 19, 20, and 21 in fig 82. Points 19 and 20 are selected as the surface structure is different at these points and point 21 represents the specification of the coating layer, which mainly covers the membrane.

106

According to the EDX measurements, strong signals of calcium, carbon and sulphur are detected, which are not rust particles, but presumably, there are isolated lime and sand particles. Therefore, the effect of the metal catalyst was even higher on the last membrane.
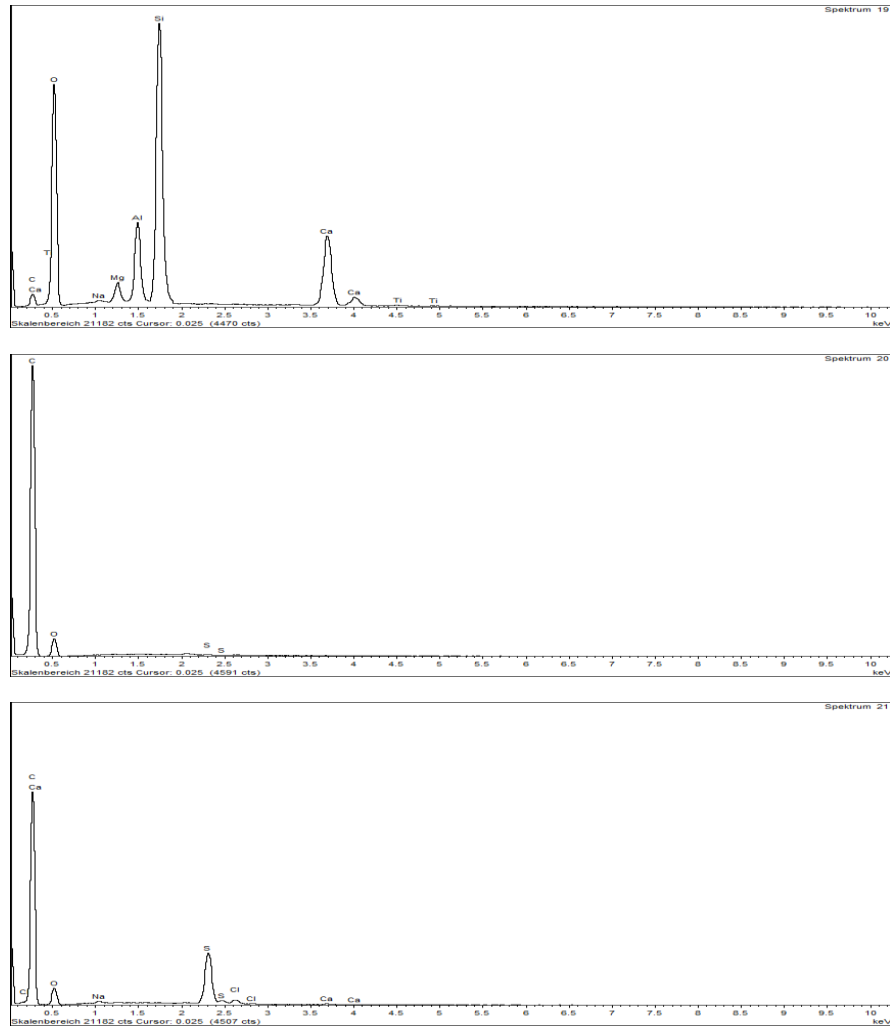
Figure 83 EDX spectra from points 19-21 belong to the fourth membrane of the test bench after the second test round.

Chapter 6

Summary and outlook

6. Summary and outlook

6.1. Summary

Small-scale PVRO systems have the highest potential to provide safe and clean water for remote areas, specifically as decentralized solutions, due to the multifaceted economic-technical advantages of this technology. Currently, the PVRO market is dominated by battery-less systems. However, the intermittent instinct of solar energy leads to frequent power fluctuations, which negatively affect the system's performance and lifetime. In this work, a new technology is developed and tested in real conditions to solve this drawback.

The whole system is also simulated using MATLAB/Simulink® to investigate the technical feasibility of the MFD technology. Results show that system performance can be increased significantly by using the developed technology. This holds especially in partial load applications, i.e., during cloudy days.

This method decreases the number of energy transformation steps and, consequently, the energy dissipation. For a PVRO system that is powered by intermittent energy sources, it is very imperative to design the system so that it can operate within a broad operational window. The simulation shows that, the working hours are extended by 4 and 5 hours, respectively, for sunny and overcast days, for the pump with a maximum pressure of 69 bar. Furthermore, main performance parameters including maximum continuous operating period, the consistent quantity of water, the maximum feed pressure, the maximum and minimum flow rate of exiting brine, and salinity of product water are improved.

Furthermore, to quantify the environmental impact, a comprehensive cradle-to-grave Life Cycle Assessment (LCA), based on ISO 1404, has been done in this work. The LCA result shows that 98.5 tons of Carbon Dioxide Equivalent (CDE) can be saved by using the MFD technology during its lifetime, even for a small system, i.e., with a capacity of 250 lit/h.

Fouling and scaling are other limiting factors in PVROs[198], particularly in small-scale and decentralized systems in remote areas, as any maintenances are more expensive[199]. In general, there are four main groups into which foulants can be classified,[200] namely sparingly soluble inorganic compounds[201], colloidal or particulate matter[202], dissolved organic substances, and microorganisms[203]. However, various feed water combinations, complicated scaling formation, and individual working conditions make it difficult to predict, recognise and

even analyse the mechanism of fouling. The findings of this thesis highlighted that the scaling is totally different between the membranes.

The first and last membranes are under more severe working conditions. Therefore, these membranes can unfold more information. Furthermore, in this study, a combination of SEM and EDX of the surface, cross-section, and permeate side of the membranes are investigated for image processing. Although the microscopic analysis of the permeate side reveals less information, the combination of facial and cross-section investigation provides a comprehensive image of the scaling structure.

6.2.   Conclusion and outlook

For the first time in this thesis, the long-term operation of a real-scale dynamic PVRO is studied by designing an accelerated test bench. A pilot project is also installed in Cape Coast, Ghana, to investigate the performance under real working conditions. Although the results show performance degradation, the water quality was still in the accepted range after an accelerated 3-year test. Based on three reasons, it can be concluded that degradation is mainly due to micro-cracks formation than scaling deposition or membrane integrity loss:

i.   Scaling happens gradually and steadily, while the results show a sharp degradation, which can be attributed to the micro-cracks.

ii.   According to the transmembrane pressure (TMP) and power consumption curves, the hydraulic resistance of the active layer is increased insignificantly. Therefore, severe scaling deposition cannot be occurred.

iii. In case of membrane integrity loss, the microbial contamination will also be drastically increased on the permeate side as it breaches the active layer[204,205].

 Furthermore, the composition, structure and evolution pattern of scaling of the first and last membranes are completely different. The main reason is the different composition of the feedwater between the first and last membrane. The first membrane shows a uniform amorphous layer embedded with iron particles, while the last membrane has an uneven crystallised layer on top of the amorphous scaling layer. The calcium-based crystals in different sizes are formed on the last membrane.

The structure of the scaling layer of the last membranes of the test bench and pilot project is physically very similar; however, the crystalline layer in the pilot project is very dense and consists of more elements, including an amorphous layer of iron, oxygen, aluminium,

manganese, and silicon. This crystalline substrate can facilitate the growth and deposition of other fouling layers like biofilms and polymeric (polysaccharides) particles.

The pre-filtration unit was improved by adding a metal catalyst in the second phase of accelerated test. The SEM and EDX images show fewer inorganic particles on the membranes, as these particles are filtered by the metal catalyst. Furthermore, as the permeate conductivity is stable during the whole test, it proves that no physical degradation happened in the second round.

As mentioned earlier, conventional PVROs use batteries to compensate for solar energy fluctuations. Based on the LCA results, by removing the battery, i.e., using MFD technology, all battery-related environmental impacts can be removed, including more than 170 kg SO_2 equivalents, which causes Acidification potential (AP), about 5 kg phosphate equivalent, which leads to a high eutrophication potential, and about 2000 kg 1,4-DCB equivalents that have a direct impact on the Human Toxicity Potential. Not least, the scarce materials used are expensive, and the mining process is harmful to the environment. Resource depletion is mainly caused by batteries, and the charging/discharging unit of the battery, contribute to more than 60% of the overall abiotic resource depletion, equal to 3.5 kg antimony (kg Sb-eq). In addition, ionizing radiation can be emitted from the ground by extracting raw materials from mines and excavation sites. Ionizing bedrock is brought to the surface, where the radiation can affect the biosphere more easily. Radiation is caused by the emissions of radionuclides such as α-, β-, γ- and x-rays. The battery unit, with a 20% share, is the largest contributor to this indicator.

In this work, a new PVRO technology is developed and tested to improve the lifetime, energy efficiency, and performance of the PVROs. In addition, for the first time, the long-term effect of the dynamic operation on the performance of the PVRO systems is investigated. However, still, there is space for further investigations:

- Effect of dynamic operation on concentration polarization:

Due to the fast water transport on the membranes, the salute concentration increases at the upstream, i.e., in the vicinity of the membrane surface[206]. Sutzkover et al. introduced a widely used model[207] to estimate concentration polarization. However, this model is based on steady-state operation. Therefore, all parameters involving standard state chemical potential, the partial molar volume of salt, and hydrostatic pressure are considered as constant

values[208]. Nonetheless, crossflow velocity and salt flux will frequently change under dynamic operating conditions. Therefore, the salt activity gradient, concentration gradient, electrostatic interactions, and even thermodynamic properties of the feed solution are altering during the whole operation[209]. As the concentration polarization negatively affects the membrane performance, the dynamic operation can reduce or even remove this issue. It is hard to calculate the concentration polarization factor and salt transport coefficients or to model the concentration polarization under dynamic operation. However, it could be possible to investigate the effect of the intermittent operation on concentration polarization and, subsequently, on permeate flux. A comparison with the normal condition would reveal valuable insights.

In addition, biofilm-related concentration polarization, specifically in the membrane's spacer-filled channel, can significantly influence the system's performance[210]. Biofouling initiates in the feed spacer's vicinity, degrading the whole membrane at the end[211]. The dynamic operation can reduce this effect as well. Furthermore, concentration polarization can accelerate the scaling because surface crystallization depends on the difference between the saturation concentration and salinity of the feed water on the membrane surface[212].

- Anti-scalant for long standstill periods

Anti-saclants can effectively delay the fouling formation[213,214], even selectively for specific mineral scales[215,216]. Anti-scalants mainly reduce the scaling ratio of the minerals and enhance the crystal structures to postpone ions clustering on the membrane surface. However, the effectiveness or drawback of using anti-scalants for intermittent operation, particularly during long overnight standstill periods, still needs to be investigated. Specifically, the van der Waals interaction should be studied and prevented, as the foulant has enough time to get closer to the membrane surface[217].

It should also be considered that a natural backwash (Osmotic Backwash – OB) can occur overnight due to the forward osmosis phenomenon in the pressure vessel[218,219]. Therefore, the solute concentration on the feed side can be reduced as permeate can be diffused back. Subsequently, anti-scalant will be significantly diluted overnight due to the high accumulated backwash volume, and long effective backwash time[220,221]. Sagiv et al. studied this mechanism and developed a convection-diffusion model to investigate the dilution/removal algorithm of

solute concentration and the detachment of the concentration polarization layer[222]. However, the influence on the anti-scalant has yet to be studied.

Furthermore, the influence of anti-scalant on the LCA could be calculated. Recently, biodegradable and phosphorus-free anti-scalants such as Polyaspartic acid (PASA), Polyepoxysuccinic Acid (PESA), polyacrylic acid sodium salt (PAAS), and copolymers of maleic and acrylic acid (MA/AA), are introduced to the market[223]. The comparison between the technical and environmental effects of using environmentally friendly anti-scalants could also be insightful.

- More comprehensive Life Cycle Assessment

Investigation of the economic and social aspects of implication of MFD technology can incorporate LCA. Further LCA research may take into account utilizing cutting-edge LCA approaches, like EIO-LCA (the economic input-output life-cycle analysis), S-LCA (social life cycle analysis), and life cycle sustainability assessment (LCSA) to connect environmental and economic or social consequences. Although EIO-LCA has recently been conducted for some conventional PVRO systems[224,225,226], S-LCA and LCSA have yet to be applied for this technology as they are the most recent additions to the LCA. In general, S-LCA and LCSA can evaluate the sustainability issues of a product or service and the possible social and economic effects on workers, users, local communities, and value-chain contributors[227,228]. These new LCA techniques might help assess the sustainability of the developed system more accurately and provide more comparative parameters for policymakers and stakeholders.

Appendix 1 – Water analysis data from Ghana

Parameter	Unit	Value	Ghana standard	WHO Guideline
Turbidity	-	32.3	5	5
Colour	Hz	22.5	5	15
pH	-	7.31	6.5-8.5	6.5-8.5
Conductivity	µS/cm	5880	-	-
Tot. Susp. Solids	mg/l	33.0	0	-
Tot. Dis. Solids (TDS)	mg/l	3528	1000	1000
Sodium	mg/l	380	200	200
Potassium	mg/l	30.4	30	30
Calcium	mg/l	292	200	200
Magnesium	mg/l	280	150	150
Total Iron	mg/l	1.98	0.3	0.3
Ammonia (NH_4-N)	mg/l	0.04	0.00-1.5	0.00-1.5
Chloride	mg/l	1643	250	250
Sulphate (SO_4)	mg/l	80	250	250
Phosphate (PO_4-P)	mg/l	0.39	-	-
Manganese	mg/l	6.19	0.4	0.4
Nitrite (NO_2-N)	mg/l	0.032	1.0	1.0
Nitrite (NO_3-N)	mg/l	0.035	10	10
Total Hardness ($CaCO_3$)	mg/l	1880	500	500
Total Alkalinity ($CaCO_3$)	mg/l	86.0	-	-
Calcium Hardness $CaCO_3$	mg/l	729	-	-
Mag. Hardness $CaCO_3$	mg/l	1151	-	-
Fluoride	mg/l	0.74	1.5	1.5
Bicarbonate $CaCO_3$	mg/l	105	-	-
Carbonate	mg/l	0	-	-

Appendix 2 – developed software

Fig. 83 depicts the flowchart and simplified code of the Standby Case. In this Case, MFD measures the open-circuit voltage of solar modules at regular intervals (S01). If the open-circuit voltage exceeds the predetermined threshold value (V_{PV_min}), the software switches to the Start-up Case (P10). Otherwise, it stays at the Standby Case (P03). All pumps should be off during this case.

```
case 10:  //'Standby Case'
      data->appV.fHP_Vorgabe = 0.0;
      data->appV.fFP_Vorgabe = 0.0;
      data->appV.Flushventil = 0;

      if(data->appV.V_DC > data->appV.VPV_min)
      {
      data->appV.operator = 20;   //'startup Case'
      data->appV.Offtimer = data->appV.Offtime;
      data->appV.Flushventil = 1;
      }

      else
      {|
            data->appV.System_ready = 0;
      }
break;
```
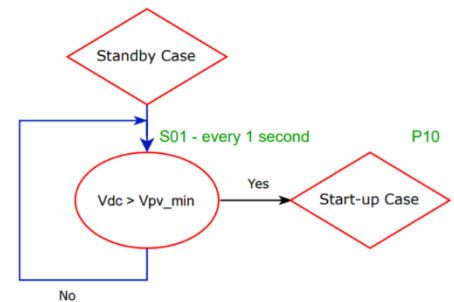

Figure 84 left: simplified code, right: flowchart of the Standby Case. In this syntax, MFD measures the DC voltage every one second and as soon as energy is enough to start the system, the software switches to the start-up case.

In the start-up case, the first sequence is to start the feed pump with minimum frequency. Therefore first, the software checks whether the feed pump is already off (S02), and then it changes the feed pump set point to f_{fp_min} (P11). It takes a few seconds until the feed pump reaches the minimum frequency, and then the high-pressure pump should be started at the minimum frequency. Before starting the high-pressure pump, the voltage of the DC bus should be checked because running the feed pump decreases the voltage, and the software should check whether there is still enough energy to start the high-pressure pump. Furthermore, according to the installation schema, the feed pump is connected to the feed water tank. To avoid dry running of the pump, the water level in the tank should be checked by the level switch (LSSW). Therefore, if the DC voltage is below the minimum threshold or if the feed tank is empty (S03), instead of starting the high-pressure pump, the whole system should be shut down (P12).

116

If S03 does not occur, the high-pressure pump can be started. In this case, the software checks the feed pump status and the voltage of the DC bus first (S04), then changes the frequency of the high-pressure pump from 0 to the f_{HP_min} (P13). The minimum frequency of each pump is different and, in no case, is lower than the permissible minimum working frequency of the pumps. In addition, to avoid cavitation on the high-pressure pump, the pressure behind the pump (P1) should be checked first (S05). P1 depends on the frequency of the feed pump and the ageing level of the pre-filters as they are installed between the feed pump and the high-pressure pump. Pre-filters should be changed every three months because particles can block the pores and increase the pressure drop of the filter. The feed pump should compensate for this pressure drop and reach the minimum input pressure of the high-pressure pump. If this pressure is not reached by the minimum frequency of the feed pump, the frequency will be increased until this condition is fulfilled (P14).

The last step in the start-up case is generating the minimum pressure for the RO system. Therefore, the software checks if the high-pressure pump has already reached the minimum frequency, and then the software will switch from the start-up case to the operation case (P13). The simplified code and the flowchart are shown in fig 84.

```
case 20: //'startup':

if (data->appV.fFP_Vorgabe < 1.0)
{
data->appV.fFP_Vorgabe = data->appV.fFPmin;
}

if (data->appV.V_DC < data->appV.VDCmin) || data->appV.LSSWempty_on == 0)
{
data->appV.operator = 10; //'switch to shutdown case';
}

//      Starting the high-pressure pump

if (data->appV.V_DC > data->appV.VDClow && data->appV.fFP > data->appV.fFPmin - 1.0) //every 2 seconds
{

        if (data->appV.P1 < data->appV.P1min && data->appV.fFP_Vorgabe < data->appV.fFPmax)
        {
              data->appV.fFP_Vorgabe++;
        }
        else if (data->appV.fHP_Vorgabe < 1.0 && data->appV.P1 > data->appV.P1min)
        {
              data->appV.fHP_Vorgabe = data->appV.fHPmin;
        }
        else if (data->appV.fHP > data->appV.fHPmin -1)
        {

              data->appV.operator = 30; //'Switch to the Operation case';
        }
             }
        else
}

 break;
```
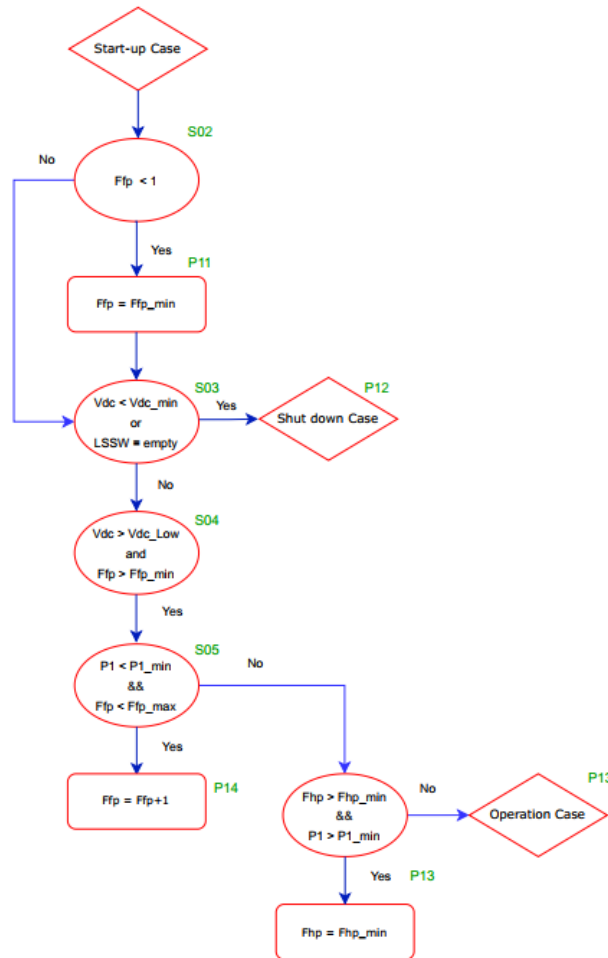
Figure 85 Top: simplified code, Down: flowchart of the Start-up Case. In this Syntax, the pumps will be started and kept at the minimum speed, which is appropriate and enough to desalinate water.

In the operation case, every 1 ms, the control system checks the system's parameters, including High-Pressure pump frequency, fresh water, and feed water tank level (S22). If the frequency of the high-pressure pump is less than the minimum permissible value, or the feed water tank is empty, or the freshwater tank is full system switches to the "shut-down case" (S22). Otherwise, mainly two tasks should be fulfilled in the operation case:

   a. the frequency of pumps must be adjusted based on the available solar energy while optimum working conditions are considered and provided for membranes

   b. the ratio of the pressure change on the membranes should be controlled and kept below 1 bar/sec.

Therefore, in the operation case, every 2 seconds control system checks whether the voltage of the DC bus is within the normal operating range of the system, i.e., 550 to 650 V DC. If this

is the case, there is no need to change the working parameters, especially the frequency of the pumps. However, as osmotic pressure depends on the feed water salinity, P2 should be regularly measured and controlled. Although feedwater chemistry rarely changes, to guarantee the optimum working conditions for membranes, software checks P2 every 1 ms.

In case the DC voltage (V_{DC}) is above 650 V or below 550 V, working parameters should be adjusted. As shown in fig 85, S21 and S31 check the voltage range. If V_{DC} falls below the normal operation range, i.e., 550V, it means that RO is consuming more energy than the available solar power. To bring the DC voltage to the normal operation range, the energy consumption of the system should be reduced by adjusting the frequency of the pumps. Therefore, the software first closes the proportional valve to keep constant pressure on the membrane. Then the frequency of the high-pressure pump should be reduced in a defined step, i.e., 0.1 Hz in each cycle (P22). Reducing the high-pressure pump frequency leads to less flux in the high-pressure line; consequently, the pressure in the low-pressure line (P1) will increase. Therefore, as the next step, if P1 is higher than the minimum threshold and the frequency of the feed pump is higher than the minimum value (S24), the frequency of the feed pump can be reduced in a defined step, i.e., 0.1 Hz in each cycle (P23). This loop will be repeated several times till The DC voltage reaches higher than the minimum threshold (550 V).

As described above, when solar energy is reducing, the software tries to reduce the frequency of the high-pressure pump feed pump in small steps and continuously adjusts the P1 and P2 to have smooth pressure changes on the membranes. On the other side, when the energy consumption of the system is lower than the available solar energy, it leads to a rise in the DC voltage (V_{DC}). When the voltage is higher than the upper limit of the normal operation range, i.e., 650 V (S31), it means that there is enough energy to increase the speed of the high-pressure pump. However, to avoid cavitation problems, the control system again checks the low-pressure line (P1) and the frequency of the feed pump (S32), and then the system increases the frequency of the feed pump to the maximum value (P31) in small steps. Afterwards, the software increases the high-pressure pump's frequency, but first, it should be checked if the high-pressure pump is already below the maximum frequency and P1 is in the permissible range (S33). Raising the high-pressure frequency leads to an increment of the flux in the high-pressure line, and consequently, P1 will be decreased. If P1 decreases below the minimum working threshold, which is 1 bar, there is a high possibility of cavitation in the

high-pressure pump. Therefore, P1 will be checked after each frequency increment, and the feed pump frequency will be adjusted accordingly. The control system repeats this cycle till the energy consumption of the system and energy production of the solar system are balanced, and in parallel, P1 is higher than the minimum threshold. The software checks the DC bus voltage every 2 seconds, and the speed increment ratio of the pumps is 0.1 Hz in each cycle. Besides, after every cycle, the software makes a 10 s delay to provide enough time for the pump to reach the new set point.

Parallel to the frequency control loops, in the operation case, the pressure (P2) and permeate flux (Q_{perm}) of the membrane will be measured every 1 ms. Any changes in the frequency of the pumps, especially the high-pressure pump, lead to pressure and flow rate changes on the membranes. To avoid pressure fluctuation and any overflow on the membranes and to keep the pressure in a defined range, the controllable proportional valve adjusts the brine flux. P2 and Q_{perm} will be measured in S41 and S51, if values are higher than the predetermined range, the valve will be opened (P41), and if the values are below the lower thresholds, the valve will be closed (P51). The flowchart and code of the operation case are shown in fig. 85 and fig. 86.
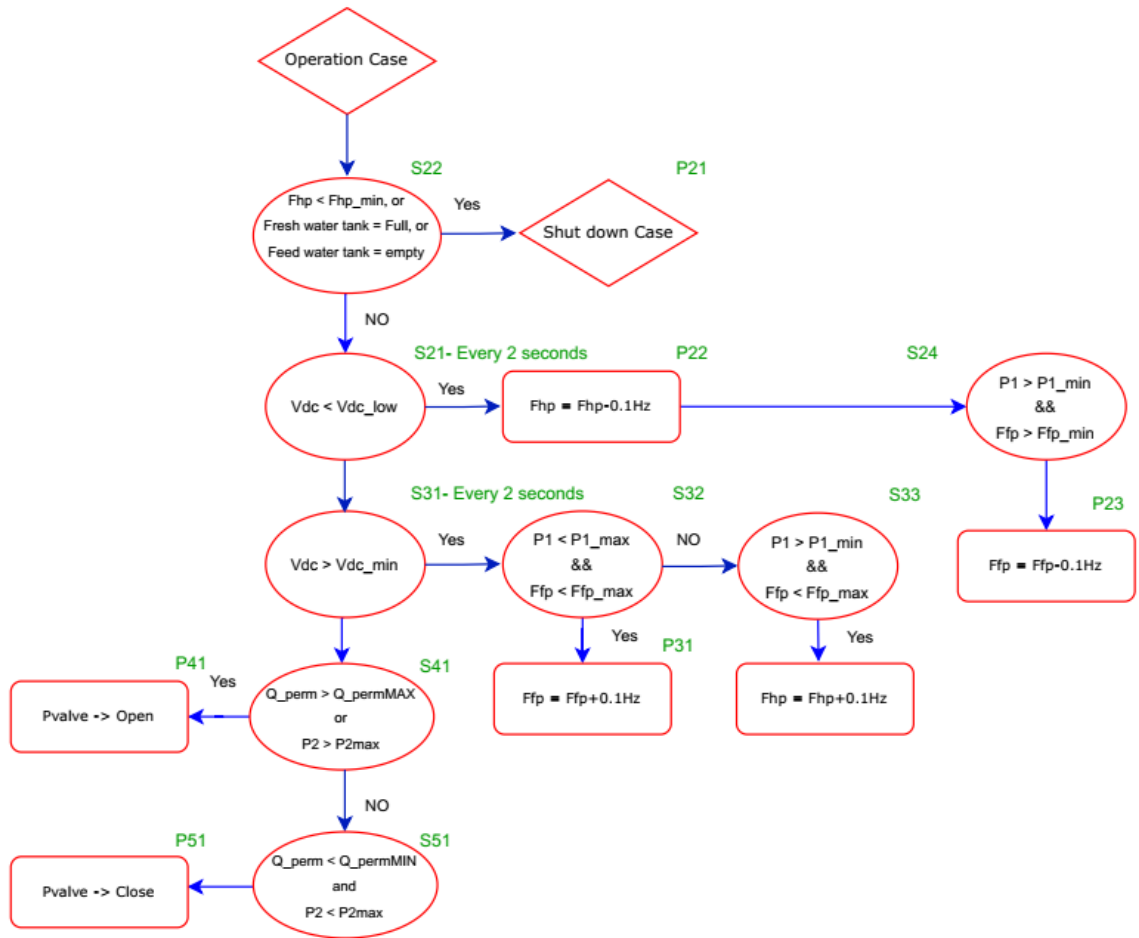
Figure 86 Operation case adjusts the frequency of the pump based on the available solar energy to smoothen the pressure fluctuations on the membranes.

```
case 30: //'Operation':


if(data->appV.fHP_Vorgabe < data->appV.fHPminlimit) || data->appV.LSFW >= data->appV.LSFWfull || data-
>appV.LSSWempty_on == 0)
        {
                data->appV.Zaehler_up = 0;
                data->appV.Zaehler_down = 0;
                data->appV.operator = 40; //'shutdown';
        }


        if(data->appV.V_DC < data->appV.VDClow) //every 2 seconds
        {
                if(data->appV.Zaehler_down > data->appV.VDC_cycles_down)
                {
                        data->appV.Zaehler_down = 0;
                        data->appV.Zaehler_up = 0;
                        data->appV.Pvalve_close = 1;
                        data->appV.Pvalve_open = 0;
                        data->appV.Zaehler_Pvalve = 0;

                        data->appV.fHP_Vorgabe = data->appV.fHP_Vorgabe - data->appV.f_red_HP;

                        if (data->appV.P1 > data->appV.P1min && data->appV.fFP_Vorgabe > data->appV.fFPmin)
                        {
                                data->appV.fFP_Vorgabe = data->appV.fFP_Vorgabe - data->appV.f_red_FP;
                        }
                }
                else
                {
                        data->appV.Zaehler_down ++;
                }
        }
        else if(data->appV.V_DC > data->appV.VDCmax) //every 2 seconds
        {
                if(data->appV.Zaehler_up > data->appV.VDC_cycles_up)
                {
                        data->appV.Zaehler_up = 0;
                        data->appV.Zaehler_down = 0;

                        if (data->appV.P1 < data->appV.P1max && data->appV.fFP_Vorgabe < data->appV.fFPmax)
                        {
                                data->appV.fFP_Vorgabe = data->appV.fFP_Vorgabe + data->appV.f_boost_FP;
                        }

                        else if (data->appV.fHP_Vorgabe < data->appV.fHPmax && data->appV.P1 > data-
                        >appV.P1min)
                        {
                                data->appV.fHP_Vorgabe = data->appV.fHP_Vorgabe + data->appV.f_boost_HP;
                        }
                }
                else
                {
                        data->appV.Zaehler_up ++;
                }
        }
        if((data->appV.Qperm > data->appV.Qpermmax || data->appV.P2 > data->appV.P2max))
        {
                data->appV.Pvalve_open = 1;
                data->appV.Pvalve_close = 0;
        }
        else if((data->appV.Qperm < data->appV.Qpermmin && data->appV.P2 < data->appV.P2max - 3.0))
        {
                data->appV.Pvalve_open = 0;
                data->appV.Pvalve_close = 1;
        }

break;
```

Figure 87 simplified code of the operation case.

The next case is shutdown, which is depicted in fig. 87. For a safe shutdown, first, the proportional valve should be opened very gently to avoid pressure shock on the membranes. Therefore, the control system first checks whether the high-pressure pump is running (S61). If so, the valve will be opened slowly (P61). After this step, the high-pressure pump can be

122

shut down. However, if the solar energy is dropping fast (S62), for example, if the shutdown is because of heavy clouds, the software reduces the frequency of the high-pressure and feed pumps slowly at the simultaneously (S62) by opening the valve. This loop will be repeated until the DC voltage exceeds the shutdown threshold, i.e., 560V. Otherwise, pumps will be switched off after 50 seconds (P63) to ensure a smooth pressure drop on the membranes. P62 and P63 have different procedures because, under P62, the frequency reduction should be made step by step. Otherwise, the membrane will be damaged. While in P63, as the proportional valve is already completely open and there is no pressure on the membranes anymore, the high-pressure pump can be shut down fast. After the complete shutdown, the system should be flushed with drinking water (see Case Flush) to eliminate the salty water (P67). The shutdown case is illustrated in fig. 87 and 88.
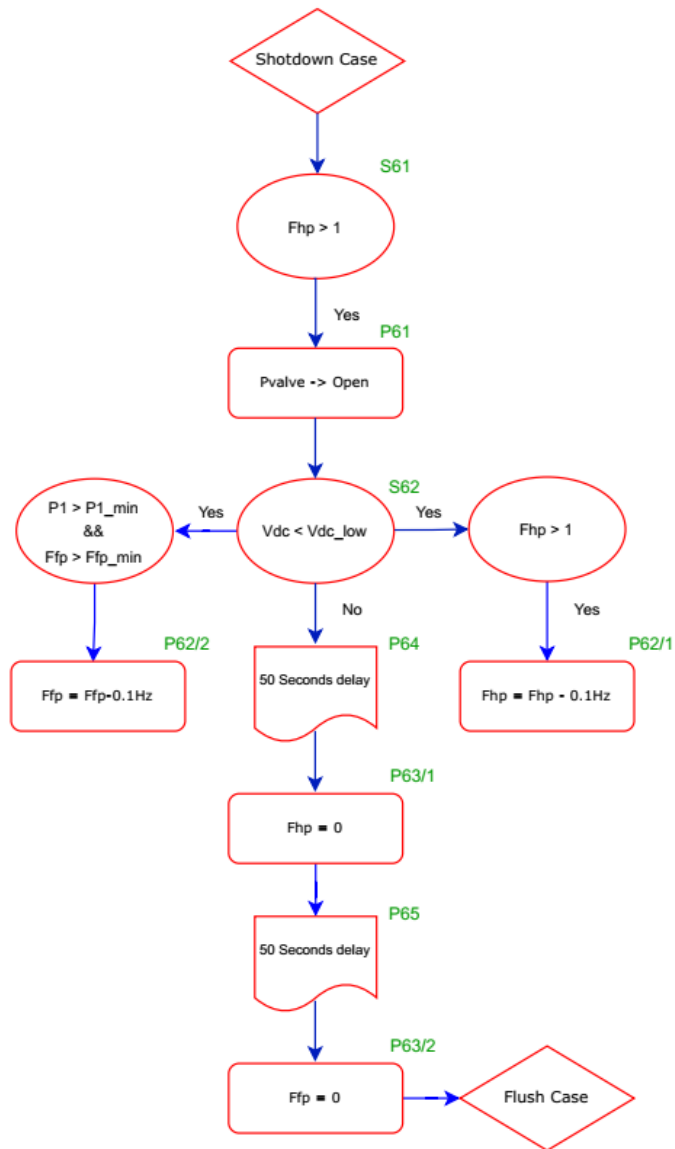
Figure 88 flowchart of shutdown case, which provides a safe and, in case, a fast shutdown for the system.

```
case 40:        //shutdown

        if (data->appV.fHP_Vorgabe > 1.0)
        {
                data->appV.Pvalve_open = 1;
                data->appV.Pvalve_close = 0;
                data->appV.Zaehler_Pvalve = 60000;
        }
        if(data->appV.V_DC < data->appV.VDClow)
        {
                if(data->appV.Zaehler_down > data->appV.VDC_cycles_down)
                {
                        data->appV.Zaehler_down = 0;
                        data->appV.Zaehler_up = 0;
                        if (data->appV.fHP_Vorgabe > 1.0)
                        {
                                data->appV.fHP_Vorgabe = data->appV.fHP_Vorgabe - data->appV.f_red_HP;
                        }
                        if ((data->appV.P1 > data->appV.P1min &&data->appV.fFP_Vorgabe > data->appV.fFPmin))
                        {
                                data->appV.fFP_Vorgabe = data->appV.fFP_Vorgabe - data->appV.f_red_FP;
                        }
                }
                else
                {
                        data->appV.Zaehler_down ++;
                }
        }
        if (data->appV.fHP_Vorgabe > 1.0 && data->appV.Zaehler_up > 50000)
        {
                data->appV.fHP_Vorgabe = 0.0;
                 data->appV.Zaehler_up = 0;
        }
        else if (data->appV.fHP < 1.0 && data->appV.Zaehler_up > 50000)
        {
                data->appV.fFP_Vorgabe = 0.0;
                data->appV.Zaehler_up = 0;
        }
        else
        {
                data->appV.Zaehler_up ++;
        }
        if (data->appV.fHP < 2 && data->appV.fFP < 2)
        {
                data->appV.operator = 50; //flush
                data->appV.Zaehler_down = 0;
                data->appV.Zaehler_up = 0;
        }

    break;
```

Figure 89 simplified code of the shutdown case, which adds enough delay for the system to open the brine valve gently. Subsequently, high-pressure and feed pumps will be shut down.

To flush the system, the feed pump will be started for a short period (4 minutes) at a low frequency (30 Hz) to flush the salty water out by using minimum drinking water and consuming very low power. As the first step in the flush case, the inlet of the feed pump should be changed from salty water to drinking water. The electric 3/2-way valve (see section 2.2.1) should be activated (P71), and then the feed pump should be set to the predetermined flush frequency (P72). In parallel, the system regularly checks the DC voltage (S72), and in case the voltage drops below the minimum value, the flushing procedure will be stopped immediately to avoid any damage due to the low voltage of the control system and software switches to Standby Case (P73). Otherwise, the flush case continues for the defined time (P74) and at the end of this time, the feed pump will be turned off (P75), and the system will go to standby mode (P76) and regularly checks the available solar power, and as soon as energy is

125

sufficient again to start the system, the software starts the Start-up Case. The procedure and the code are explained in fig. 89 and fig. 90.
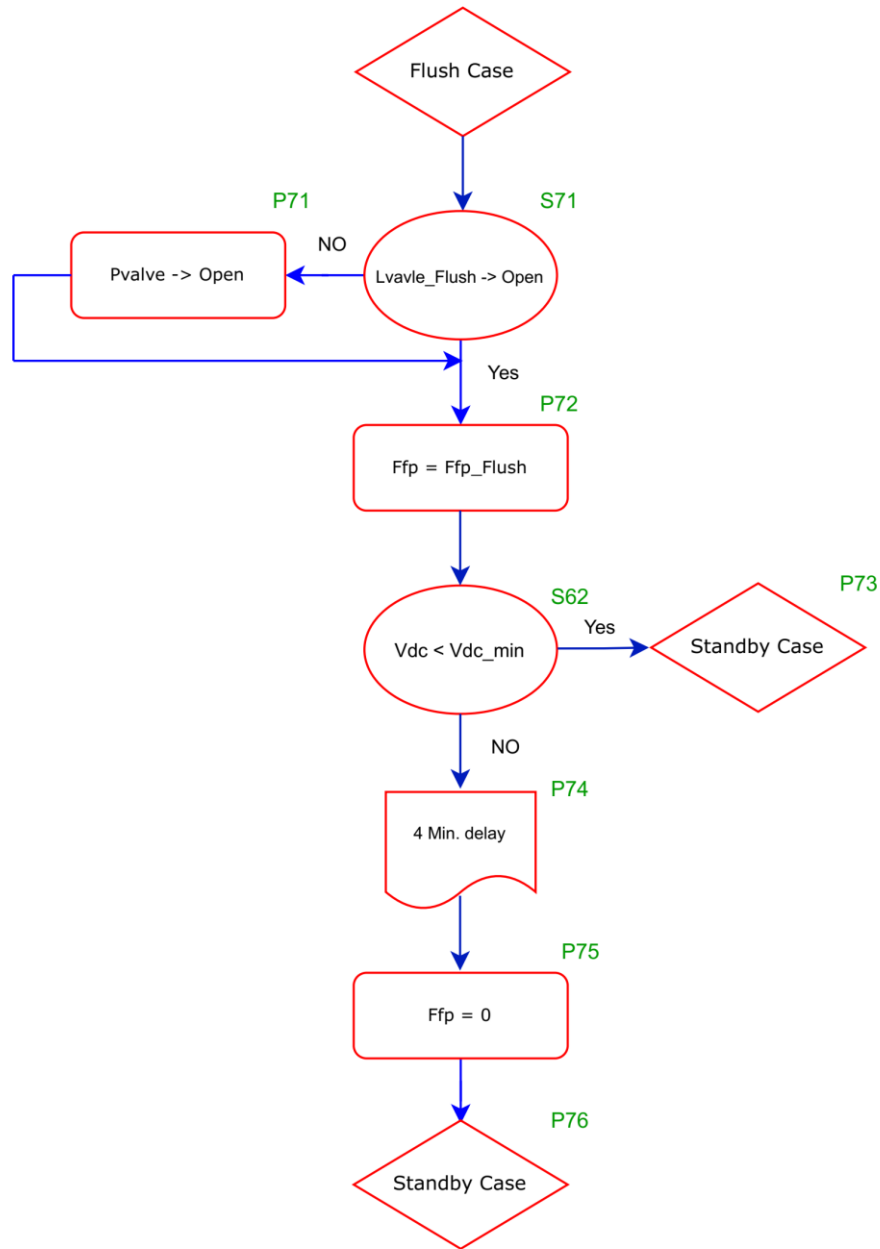
Figure 90 Flush case is crucial for the system to avoid corrosion overnight. The flowchart is illustrated in this figure.

```
case 50: //'flush':

        if (data->appV.fHP_Vorgabe > 1.0 && data->appV.Zaehler_Flush == 0)
        {
        data->appV.fHP_Vorgabe = 0.0;

        if (data->appV.LValve_Flush == 1)
        {
              if(data->appV.fFP <= 1.0)
              {
                    data->appV.fFP_Vorgabe = data->appV.fFP_flush;
              }
        }

        if (data->appV.Zaehler_Sec == 9999)
        {
              data->appV.Zaehler_Flush ++;
        }

        if(data->appV.V_DC < data->appV.VDCmin)
        {
              if (data->appV.Zaehler_down > 1000)
              {
              data->appV.Zaehler_down = 0;
              data->appV.Zaehler_Flush = data->appV.flushtime;
              }
              else
              {
                    data->appV.Zaehler_down++;
              }
        }
        if(data->appV.Zaehler_Flush >= data->appV.flushtime)
        {
              data->appV.fFP_Vorgabe = 0.0;
        }
        if(data->appV.Zaehler_Flush >= data->appV.flushtime && data->appV.fFP < 1.0)
        {
                    data->appV.operator = 10; //'Standby';
                    data->appV.Zaehler_Flush = 0;
                    data->appV.Zaehler_down = 0;
                    data->appV.Zaehler_up = 0;
                    data->appV.Flushventil = 0;
        }
 break;
```

Figure 91 Flush Case provides enough delay to remove all salty water from the system while regularly checking the available power to avoid low voltage damages.

Appendix 3 – Remote monitoring system

a) developed Phyton code for the AWS platform (Elastic Container)

```
import argparse, logging, sys, os,random,time,json,datetime,requests,socket,traceback,struct

NETWORK_SEND_STRUCT_SIZE = 696
NETWORK_SEND_FIELD_SIZE = 15
delaySecond = 5
WebAPI="https://i5zp4qtqoj.execute-api.eu-central-1.amazonaws.com/dev/save"
deviceID=102

Metrics = {
    "0": "zerovalue",
    "1": "secondssincesystemstart",
    "2": "operator",
    "3": "solarsensor",
    "4": "frequency_feedpump",
    "5": "frequency_ro-pump",
    "6": "frequency_bh-pump",
    "7": "loggertime",
    "8": "status_valve",
    "9": "qperm",
    "10": "pressure1",
    "11": "pressure2",
    "12": "tds",
    "13": "amountbadwater",
    "14": "levelsensor_seawater",
    "15": "levelsensor_freshwater",
    "16": "recovery",
    "17": "not_aus",
    "18": "fehler_pumpen",
    "19": "pressurerror",
    "20": "sensorerror",
    "21": "not_aus_extern",
    "22": "fehler_pv",
    "23": "temp_fehler",
    "24": "extra"
}

def parse_args():
    parser = argparse.ArgumentParser()
    parser.add_argument("--tiaddr", help="host:port of the TI" ,required=True)
    # parser.add_argument("--jsonfile", help="filename where to write json")
    parser.add_argument("--quiet", help="do not print log on output console" ,default=False)
    parser.add_argument("--simulated", help="activate simulation mode")
    return parser.parse_args()

def init_logging(disable_logging):
    if not disable_logging:
        logger = logging.getLogger()
        logger.setLevel(logging.INFO)
        logHandler = logging.StreamHandler(sys.stdout)
        logHandler.setFormatter(logging.Formatter("%(asctime)s | %(levelname)s | %(message)s"))
        logger.addHandler(logHandler)
        logger.info("=============================================================")
        logger.info(f"bin : {os.path.basename(sys.argv[0])} ")
        logger.info(f"args: {sys.argv[1:]} ")
        logger.info(f"cwd : {os.getcwd()} ")
        logger.info(f"pid : {os.getpid()} ")
        logger.info(f"ppid: {os.getppid()} ")
        logger.info("=============================================================")
```

128

```python
def webapi_ready():
    response = requests.get(WebAPI.replace('/save','/status'))
    return response.ok


def get_slowDataID(data, i):
    offset = 4 + (4 * NETWORK_SEND_FIELD_SIZE) + (20 * 2 * NETWORK_SEND_FIELD_SIZE) + (2 * i)
    return struct.unpack("h", data[offset: offset + 2])[0]


def get_slowDataContent(data, i):
    offset = 4 + (4 * i)
    return struct.unpack("f", data[offset: offset + 4])[0]


def send_real_data(deviceID,delay_second,metrics,webAPI,tiaddr,quiet):
    try:
        zero_command = bytes(4)
        logging.info("IoT Hub device is going to send real data")
        ti_host, ti_port = tiaddr.split(":")
        with socket.socket(socket.AF_INET, socket.SOCK_STREAM) as ti_socket:
            logging.info(f"connecting... to ti_socket on {ti_host}:{ti_port}")
            ti_socket.connect((ti_host, int(ti_port)))
            while True:
                data = ti_socket.recv(NETWORK_SEND_STRUCT_SIZE)
                if len(data) != NETWORK_SEND_STRUCT_SIZE:
                    raise Exception("recived incomplete data from TI")
                logging.info(f"recived {len(data)} new data from TI")
                # real_data = f'-1;{datetime.datetime.now().time()},'
                real_data_dict = dict()
                for i in range(0, NETWORK_SEND_FIELD_SIZE):
                    real_data_dict.update({str(get_slowDataID(data, i)): get_slowDataContent(data, i)})
                    # real_data_dict.update({Metrics[str(get_slowDataID(data, i))]: get_slowDataContent(data, i)})
                    # real_data += f'{get_slowDataID(data, i)};{round(get_slowDataContent(data, i),2)},'

                real_data = f'-1;{datetime.datetime.now().time()},'
                # sample_data = f'-1;{datetime.datetime.now().time()},'
                for metric in metrics.keys():
                    if metric in real_data_dict:
                        real_data += f'{metric};{round(real_data_dict[metric],2)},'
                    else:
                        real_data += f'{metric};0,'


                real_data=real_data.strip(',')
                if not quiet:
                    logging.info(f'\n  [last real data got from ti] >> {real_data}')
                response = requests.post(f"{webAPI}/{deviceID}", data=real_data,headers={'Content-Type': 'text/plain'})
                if not response.ok:
                    logging.info('Grino Web API does not respond')
                else:
                    logging.info(response.json())
                time.sleep(delay_second)
                # ti_socket.sendall(zero_command)
                current_time = datetime.datetime.now().time()
                if current_time > datetime.time(12, 50) and current_time < datetime.time(12, 51):
                    ti_socket.sendall(bytes([1, 0, 0, 0]))
                    logging.info(f'bytes sended to ti socket at {current_time}')
                else:
                    ti_socket.sendall(zero_command)
    except KeyboardInterrupt:
        logging.info("keyboard interrupt... IoT Hub device is stoping...")
        ti_socket.shutdown(socket.SHUT_RD)
        # send message the TI will identify as a close; we want the TI to initiate socket close
        ti_socket.sendall(bytes([255, 255, 255, 255]))
        logging.info("waiting 5 second for TI to catch up")
        time.sleep(5)
```

```python
            logging.info("closing TI Socket...")
            ti_socket.close()
        except Exception:
            logging.error('●  in sending real data, the device will try again after 15 second...')
            traceback.print_exc(file=sys.stderr)
            time.sleep(15)
            send_real_data(deviceID,delay_second,metrics,webAPI,tiaddr,quiet)


# def send_simulated_data(deviceID,delay_second,metrics:dict,webAPI,quiet):
#     try:
#         logging.info("IoT Hub device simulator started")
#         while True:
#             sample_data = dict()
#             for metric in metrics.values():
#                 sample_data.update({metric: round(random.random() * 20,2) })
#             sample_data.update({"time": str(datetime.datetime.now().time())})
#             logging.info("Sending sample simulated data to Grino Web API..., press Ctrl-C to exit")
#             if not quiet:
#                 logging.info(f'\n{sample_data}\n')
#             response = requests.post(f"{webAPI}/{deviceID}", data=sample_data)
#             if not response.ok:
#                 logging.info('Grino Web API does not respond')
#             time.sleep(delay_second)
#     except KeyboardInterrupt:
#         logging.info("IoT Hub device simulator stopped")

def send_simulated_data(deviceID,delay_second,metrics:dict,webAPI,quiet):
    try:
        logging.info("IoT Hub device simulator started")
        while True:
            sample_data = f'-1;{datetime.datetime.now().time()},'
            for metric in metrics.keys():
                sample_data += f'{metric};{round(random.random() * 20,2)},'
                # sample_data.update({metric: round(random.random() * 20,2) })
            # sample_data.update({"time": str(datetime.datetime.now().time())})
            sample_data=sample_data.strip(',')
            logging.info(f"Device {deviceID} Sending sample simulated data to Grino Web API..., press Ctrl-C to exit")
            if not quiet:
                logging.info(f'\n{sample_data}')
            response = requests.post(f"{webAPI}/{deviceID}", data=sample_data,headers={'Content-Type': 'text/plain'})
            if not response.ok:
                logging.info('Grino Web API does not respond')
            else:
                logging.info(f'{response.json()}\n')
            time.sleep(delay_second)
    except KeyboardInterrupt:
        logging.info("IoT Hub device simulator stopped")

def main():
    args = parse_args()
    init_logging(args.quiet == True)
    if sys.version_info[0] == 2:
        print("error, requires Python 3.x; tying calling script using python3")
        sys.exit(1)
    if not webapi_ready():
        print(f"Grino Web API does not respond, please check the Web API address:\n{ WebAPI.replace('/save','/status') }")
        sys.exit(1)
    if args.simulated:
        send_simulated_data(deviceID,delaySecond,Metrics,WebAPI,args.quiet)
    else:
        send_real_data(deviceID,delaySecond,Metrics,WebAPI,args.tiaddr,args.quiet)
```

```
if __name__ == "__main__":
   main()
```

b) 23 parameters which are sent by remote monitoring as a JSON file to the AWS platform.

	Monitoring Parameter	Symbol	Unit	Data range
1.	System On/Off signal	Z_Value	-	0-1
2.	System Running Time	SS	Seconds	0-40000
3.	Controller Running time	CS	Seconds	0-400000
4.	Proportional Valve Position	PVP	%	0-100%
5.	System Operating Mode	OM	-	0-10
6.	Feed Pump Frequency	f_{fp}	Hz	0-60
7.	High-pressure Pump Frequency	f_{hp}	Hz	0-60
8.	Borehole pump frequency	f_{bp}	Hz	0-60
9.	Battery Voltage	V	Volt	0-28
10.	Permeate flux	Q_{perm}	l/min	0-250
11.	Low-Pressure Line	P_{LP}	Bar	0-6
12.	High-Pressure Line	P_{HP}	Bar	0-65
13.	Permeate salinity	C_{perm}	ppm	0-1000
14.	Water level in drinking water tank	LSFW	M	0-5
15.	Water level in feed water tank	LSSW	M	0-10
16.	Solar irradiance power	P_PV	W/m^2	0-1250
17.	Pump error	P_{err}	-	0-1
18.	Pressure error	Pre_{err}	-	0-1
19.	Borehole pump error	PBH_{err}	-	0-1
20.	Temperature error	$Temp_{err}$	-	0-1
21.	Amount of Water > 1000 ppm	BW	Lit	0-50
22.	Recovery ratio	R	%	0-100
23.	Emergency Shut Down Situation	Not-Aus	-	0-1

Appendix 4 – theoretical background of the simulation

PV array (mask) (link)

Implements a PV array built of strings of PV modules connected in parallel. Each string consists of modules connected in series.
Allows modeling of a variety of preset PV modules available from NREL System Advisor Model (Jan. 2014) as well as user-defined PV module.

Input 1 = Sun irradiance, in W/m2, and input 2 = Cell temperature, in deg.C.

Parameters | Advanced

Array data

Parallel strings 1

Series-connected modules per string 18

Module data

Module: User-defined

Maximum Power (W) 250.205

Cells per module (Ncell) 60

Open circuit voltage Voc (V) 37.3

Short-circuit current Isc (A) 8.66

Voltage at maximum power point Vmp (V) 30.7

Current at maximum power point Imp (A) 8.15

Temperature coefficient of Voc (%/deg.C) -0.36901

Temperature coefficient of Isc (%/deg.C) 0.086998

Display I-V and P-V characteristics of ...

array @ 25 deg.C & specified irradiances

Irradiances (W/m2) [1000 700 100]

Plot

Model parameters

Light-generated current IL (A) 8.7062

Diode saturation current I0 (A) 4.1579e-10

Diode ideality factor 1.0189

Shunt resistance Rsh (ohms) 240.6015

Series resistance Rs (ohms) 0.23732

Figure 92 to simulate the PV array, standard model from the Simulink library is used, and parameters are adjusted based on the developed PVRO.
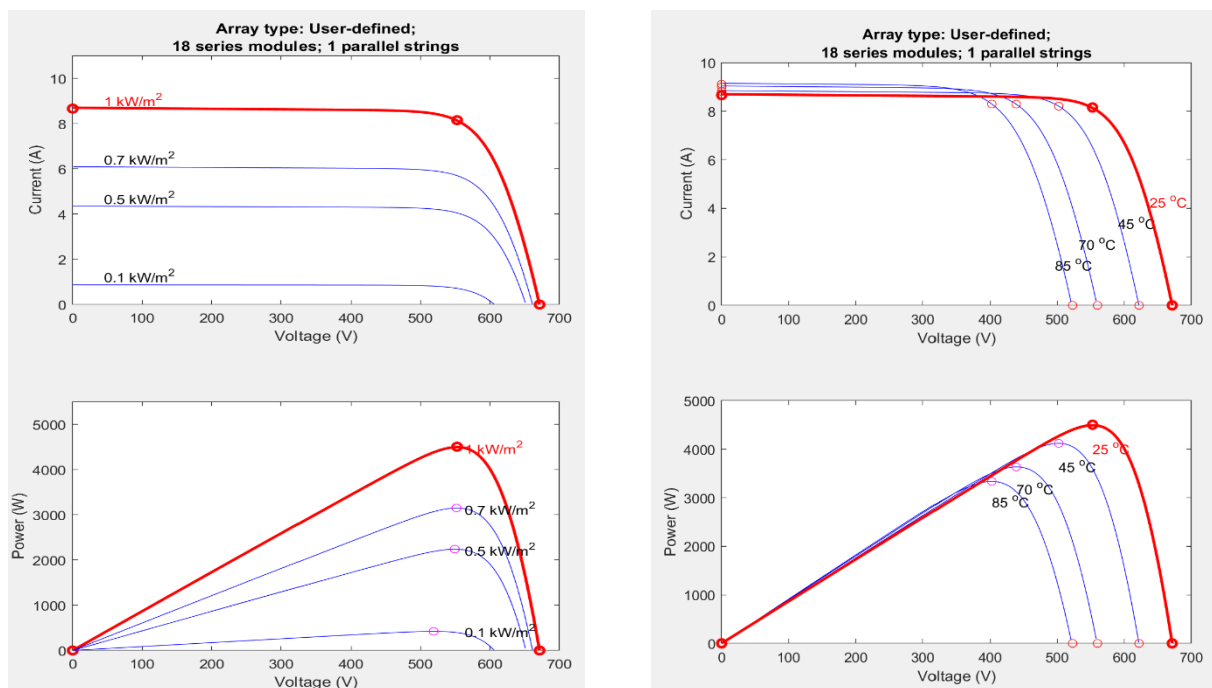
Figure 93 climate conditions, especially solar irradiance, and ambient temperature, can significantly influence the generated power of PV panels[229].

132
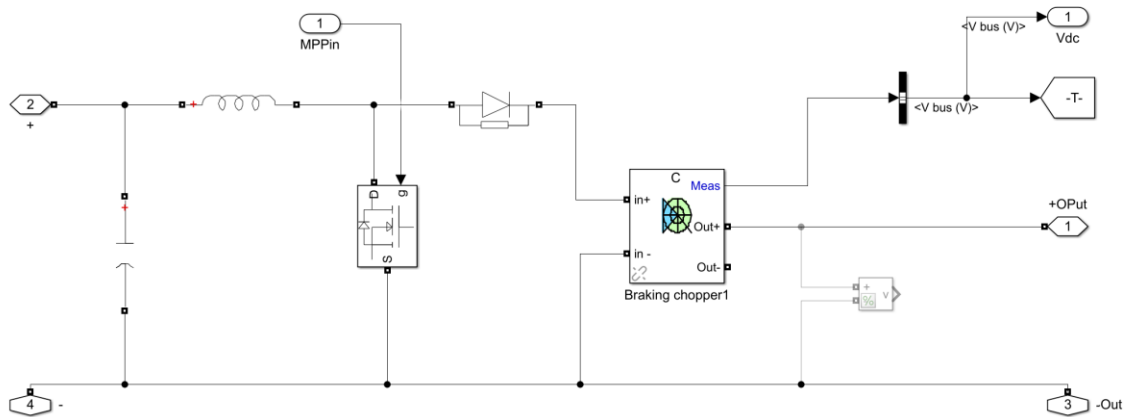
Figure 94 Simulated block of the MPP tracker. Duty-cycle is a Boolean value calculated in another block. To calculate the optimum duty-cycle value and generate the Boolean-value, a "perturb and observe algorithm" is used, which is illustrated in fig. 94.
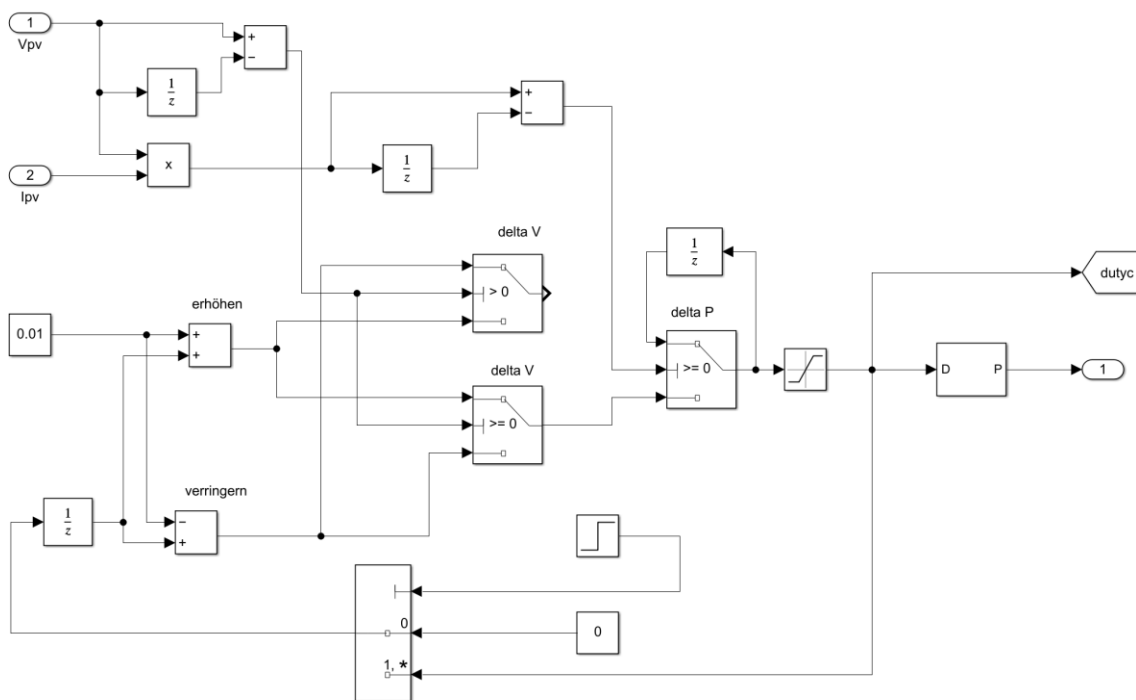
Figure 95 equivalent model based on the "perturb and observe algorithm" to generate the appropriate Boolean values for the duty cycle.

Asynchronous Machine (mask) (link)

Implements a three-phase asynchronous machine (wound rotor, squirrel cage or double squirrel cage) modeled in a selectable dq reference frame (rotor, stator, or synchronous). Stator and rotor windings are connected in wye to an internal neutral point.

| Configuration | Parameters | Advanced | Load Flow |

Nominal power, voltage (line-line), and frequency [Pn(VA),Vn(Vrms),fn(Hz)]: [4000 400 50]

Stator resistance and inductance[Rs(ohm) Lls(H)]: [0.25205 0.002539]

Rotor resistance and inductance [Rr'(ohm) Llr'(H)]: [0.50255 0.002539]

Mutual inductance Lm (H): 0.1222

Inertia, friction factor, pole pairs [J(kg.m^2) F(N.m.s) p()]: [0.0001 0.0 1]

Initial conditions

[slip, th(deg), ia,ib,ic(A), pha,phb,phc(deg)]:

[0, 0, 0, 0, 0, 0,0,0]

Figure 96 to create a precise model and have minimum errors, resistance and inductance values should be defined exactly in Simulink. For this work, a 4 kW motor is simulated[230].
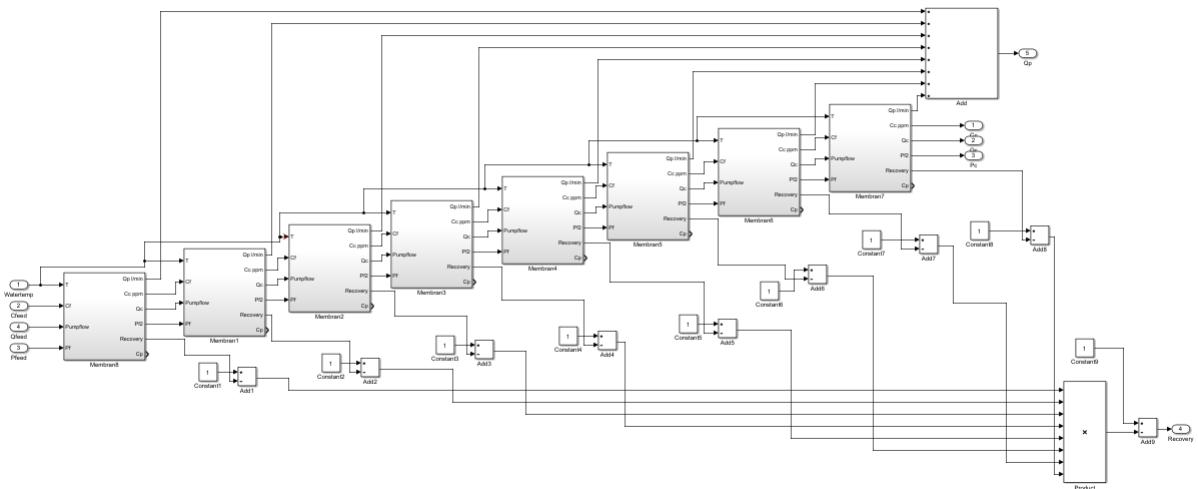
Figure 97 membrane subsystem including eight membranes in series. Feed water information is used as the input of the subsystem, and permeate data, recovery ratio, as well as brine water are the outputs of the subsystem.

134

Appendix 5 – Sample of logging data

	P1	P2	TDS	Water temp.	Qperm	f1	f2
14:24:49	3.06	2.75	39.77	21.09	0.30	40	15
14:24:59	2.86	12.27	38.78	21.68	0.02	40	32
14:25:09	2.96	20.84	268.97	22.03	7.76	41	42
14:25:19	3.42	23.18	82.66	22.06	8.43	45	48
14:25:29	3.60	23.88	53.26	22.46	8.76	46	50
14:25:39	3.59	23.79	51.50	22.43	8.79	46	50
14:25:49	3.60	23.56	49.81	22.61	8.87	46	50
14:25:59	3.62	23.30	50.26	22.57	8.92	46	50
14:26:09	3.62	22.49	50.08	22.64	8.78	46	50
14:26:19	3.61	22.26	49.95	22.63	8.73	46	50
14:26:29	3.60	22.18	50.66	22.40	8.75	46	50
14:26:39	3.61	22.10	50.61	22.49	8.77	46	50
14:26:49	3.62	22.06	50.59	22.33	8.77	46	50
14:26:59	3.61	22.02	51.56	22.04	8.80	46	50
14:27:09	3.61	22.03	51.55	21.81	8.79	46	50
14:27:19	3.61	22.01	51.81	21.61	8.81	46	50
14:27:29	3.63	21.97	52.14	21.24	8.80	46	50
14:27:39	3.60	21.88	51.03	21.46	8.85	46	50
14:27:49	3.22	21.09	51.60	21.10	8.52	43	47
14:27:59	2.73	18.86	51.01	20.81	7.47	39	41
14:28:09	2.75	17.85	50.89	20.59	7.02	39	39
14:28:19	3.02	18.76	52.16	20.23	7.41	41	43
14:28:29	3.51	21.48	52.61	20.00	8.77	45	49
14:28:39	3.61	21.50	51.52	19.90	8.95	45	50
14:28:49	3.63	21.37	51.60	19.79	8.96	45	50
14:28:59	3.61	21.23	50.54	19.59	8.96	45	50
14:29:09	3.60	21.12	49.68	19.67	8.95	45	50
14:27:07	3.61	2.00	48.12	22.66	8.90	45	50
14:27:17	3.61	21.47	48.12	22.66	8.90	45	50
14:27:27	3.61	21.47	48.12	22.66	8.90	45	50
14:27:37	3.61	21.47	48.12	22.66	8.90	45	50
14:27:47	3.61	21.47	48.12	22.66	8.90	45	50
14:27:57	3.61	21.47	48.12	22.66	8.90	45	50
14:28:07	3.61	21.47	48.12	22.66	8.90	45	50
14:28:17	3.61	21.47	48.12	22.66	8.90	45	50
14:28:27	3.61	21.47	48.12	22.66	8.90	45	50
14:28:37	3.61	21.47	48.12	22.66	8.90	45	50
14:28:47	3.61	21.47	48.12	22.66	8.90	45	50
14:28:57	3.61	21.47	48.12	22.66	8.90	45	50
14:29:07	3.61	21.47	48.12	22.66	8.90	45	50

Bibliography

[1] Kartalidis A, Kampragkou E, Assimacopoulos D, Tzen E, Responding to water challenges in Greece through desalination: energy considerations, Journal of Water Resources and Rural Development, 2015, pp. 14.

[2] http://www.un.org/waterforlifedecade/scarcity.shtml

[3] Tataru L, Nedeff V, Barsan N, Panainte-Lehadus M, Mosnegutu E F, Efficiency studies of hollow fiber organic membranes in restraining yeast from wastewater subjected to ultrafiltration, Proceeding of the International Multidisciplinary Scientific GeoConference Surveying Geology and Mining Ecology Management (SGEM), 2018, pp. 235-242.

[4] https://www.worldwildlife.org/threats/water-scarcity

[5] Ritchie H, Roser M, "Clean Water", Published online at ourworldindata.org., 2019, https://ourworldindata.org/water-access, accessed on 28.12.2020.

[6] Gude V G, Desalination and water reuse to address global water scarcity, Journal of Reviews in Environmental Science and Bio/Technology, Volume 16, 2017, pp. 591-609.

[7] Tularam G A, Ilahee M, Environmental concerns of desalinating seawater using reverse osmosis, Journal of environmental monitoring, JEM, Volume 9, 2007, pp. 805-813.

[8] Kharraz J A, Richards B S, Schäfer A I, Autonomous solar-powered desalination systems for remote communities, 2017, pp. 75-125

[9] Desalination & Water Reuse, Global Water Intelligence, 2017.

[10] Cherif H, Champenois G, Belhadj J, Environmental life cycle analysis of a water pumping and desalination process powered by intermittent renewable energy sources, Journal of Renewable and Sustainable Energy Reviews, volume 59, 2016, pp. 1504–1513.

[11] Kalogirou SA (2018) Introduction to renewable energy powered desalination. Renewable energy powered desalination handbook. Elsevier, Amsterdam, pp. 3–46.

[12] Lafond F, Bailey A G, Bakker J D, Rebois D, Zadourian R, McSharry P, Farmer J D, How well do experience curves predict technological progress? A method for making distributional forecasts, Journal of Technological Forecasting and Social Change, Volume 128, 2018, 104-117.

[13] K. Jijakli et al., How green solar desalination really is? Environmental assessment using life-cycle analysis (LCA) approach, Desalination Journal, Volume 287, 2012, pp. 123- 131.

[14] Yuting w, Optimization of Integrated Seawater Desalination & Salt Production, Environmental Engineering Project, 2014.

[15] Darre N C, Toor G S, Desalination of water: a review. Current Pollution Reports Journal, Volume 4, 2018, pp. 104–111.

[16] Hernandez A, Muñoz R, Ventura S, Büscher W, Christoph R, Study of low cost materials for the enhancement of solar seawater desalination, Journal of Periodico Tche Quimica, Volume 15, 2018, pp. 300–308.

[17] Jones E, Qadir M, van Vliet MTH, Smakhtin V, Kang S, The state of desalination and brine production: a global outlook, Journal of Science of the Total Environment, Volume 657, 2019, pp. 1343–1356.

[18] Wetterau G, Desalination of seawater, American Water Works Association, Volume 61, 2011, Denver.

[19] Esmaeilion F, Hybrid renewable energy systems for desalination, Journal of Applied Water Science, 2020, pp. 10-84.

[20] American Water Works Association (AWWA), Reverse Osmosis and Nanofiltration, Manual of Water Supply Practices, Second Edition.

[21] Gomez J D, Hill C, Huehmer R P, Assessment of Osmotic Mechanisms Pairing Desalination Concentrate and Wastewater Treatment, Austin, Texas: Texas Water Development Board; 2011.

[22] Lee K P, Arnot T C, Mattia D, A review of reverse osmosis membrane materials for desalination—Development to date and future potential, Journal of membrane Science, Volume 370, 2011, pp. 1-22.

[23] Widiasa IN, Paramita V, Kusumayanti H (2009) BWRO Desalination for potable water supply enhancement in coastal regions, Coast Development Journal, Volume 12, pp. 81–88.

[24] Kadaj E, Bosleman R, Energy recovery devices in membrane desalination processes, Renewable energy powered desalination handbook, Elsevier, New York, 2018, pp. 415–444.

[25] Yang Z, Zhou Y, Feng Z, Rui X, Zhang T, Zhang Z, A Review on Reverse Osmosis and Nanofiltration Membranes for Water Purification, Polymers Journal, 2019.

[26] Thabit, M.S., Hawari, A.H., Ammar, M.H., Zaidi, S.; Zaragoza, G., Altaee, A. Evaluation of forward osmosis as a pre-treatment process for multi-stage flash seawater desalination, Desalination Journal, Volume 461, 2019, pp. 22–29.

[27] Jiang S, Li Y, Ladewig B P, A review of reverse osmosis membrane fouling and control strategies, Journal of Science of the Total Environment, Volume 595, 2017, pp. 567-583.

[28] Gur-Reznik S, Katz I, Dosoretz C G, Removal of dissolved organic matter by granular activated carbon adsorption as a pre-treatment to reverse osmosis of membrane bioreactor effluents, Water Research Journal, Volume 42, 2008, pp. 1595-1605.

[29] Jiang S, Li Y, Ladewig B P, A review of reverse osmosis membrane fouling and control strategies, Science of the Total Environment Journal, Volume, 595, 2017, pp. 567-583.

[30] Kavithaa J, Rajalakshmia M, Phanib A R, Padaki M, Pre-treatment processes for seawater reverse osmosis desalination systems—A review, Journal of Water Process Engineering, Volume 23, 2019.

[31] Lipp P, Witte M, Baldauf G, Povorov A A, Treatment of reservoir water with a backwashable MF/UF spiral wound membrane, Desalination Journal, Volume 179, 2005, pp. 83-94.

[32] Lee A, Elam J W, Darling S B, Membrane materials for water purification: design, development, and application, Environmental Science: Water Research & Technology journal, Volume 2, 2016, pp. 17-42.

[33] Doornbusch G, Wal M, Tedesco M, Post J, Nijmeijer K, Borneman Z, Multistage electrodialysis for desalination of natural seawater, Desalination Journal, 2021.

[34] Krishna HJ. Introduction to Desalination Technologies. Austin, Texas: Texas Water Development Board, 2004, pp. 7.

[35] Buros O K, The ABC's of Desalting. Topsfield, Massachusetts: International Desalination Association, 1990.

[36] Chandrashekara M, Yadav A, Water desalination system using solar heat: a review. Journal of Renew Sustain Energy. Volume 67, 2017, pp. 1308–1330.

[37] Ghaffour N, Lattemann S, Missimer T, Ng KC, Sinha S, Amy G, Renewable energy-driven innovative energy-efficient desalination technologies. Applied Energy Journal, Volume 136, 2014, pp. 1155–1165

[38] Hassanean M H M, Nafey A S, El-Maghraby R M, Ayyad F M, Simulation of Multi-Stage Flash with Brine Circulating Desalination Plant, Journal of Petroleum and Mining Engineering Volume 21,2019, pp. 34-42

[39] Hanshik, C, Jeong, H, Jeong, K Water, Choi S H, Improved productivity of the MSF (multi-stage flashing) desalination plant by increasing the TBT (top brine temperature), Energy Journal, Volume 107, 2016, pp. 683–692.

[40] Kim B, Purification of high salinity brine by multi-stage ion concentration polarization desalination. Scientific Reports Journal, Volume 6, 2016.

[41] Micale G, Rizzuti L, Cipollina A, Seawater desalination: conventional and renewable energy processes. Springer, 2009, Berlin.

[42] Bennett A, Developments in desalination and water reuse, Filtration Separation Journal, Volume 52, 2015, pp.28–33.

[43] El-Ghonemy, A.M.K. Performance test of a sea water multi-stage flash distillation plant: Case study. Alexandria Engineering Journal, Volume 57, 2018, pp. 2401–2413.

[44] El-Ghonemy A M K, Future sustainable water desalination technologies for the Saudi Arabia: a review. Journal of Renewable and Sustainable Energy, Volume 16, 2012.

[45] Al-Othman A, Tawalbeh M, Assad MEH, Alkayyali T, Eisa A, Novel multi-stage flash (MSF) desalination plant driven by parabolic trough collectors and a solar pond: a simulation study in UAE, Desalination Journal, Volume 443, 2018, pp. 237–244.

[46] Aliku O, Desalination: A Means of Increasing Irrigation Water Sources for Sustainable Crop Production, 2017.

[47] Ortega-Delgado B, Garcia-Rodriguez L, Alarcón-Padilla D C, Opportunities of improvement of the MED seawater desalination process by pre-treatments allowing high-temperature operation, Journal of Desalination and Water Treatment, Volume 97, 2017, pp. 94–98

[48] Miller J E, Review of water resources and desalination technologies, Sandia national labs unlimited release report, 2003.

[49] Voutchkov N, Desalination engineering: planning and design, McGraw Hill Professional, New York, 2012.

[50] Metcalf and Eddy. Wastewater Engineering: Treatment and Reuse. 4th edition, New York: McGraw-Hill, 2003.

[51] Hasan E, Desalination Integration with Renewable Energy for Climate Change Abatement in the MENA Region, Recent Progress in Desalination, Environmental and Marine Outfall Systems, Volume 1, 2015, pp. 159-173.

[52] Ahmadi E, McLellan B, Mohammadi-Ivatloo B, Tezuka T, The role of renewable energy resources in sustainability of water desalination as a potential fresh-water source: An updated review, Sustainability Journal, Volume 12, 2020, pp. 5233.

[53] Shatat M, Worall M, Riffat S, Opportunities for solar water desalination worldwide: Review, Journal of Sustainable Cities and Society, Volume 9, 2013, pp. 67-80.

[54] Moser M, Trieb F, Fichter T, Potential of concentrating solar power plants for the combined production of water and electricity in MENA countries, Journal of Sustainable Development of Energy, Water and Environment Systems, Volume 1, 2013, pp. 122-40.

[55] Alkaisi A, Mossad R, Sharifian-Barforoush A, A Review of the Water Desalination Systems Integrated with Renewable Energy, Energy Procedia, Volume 110, 2017, pp. 268-274.

[5656] MA Q, LU H, Wind energy technologies integrated with desalination systems: Review and state-of-the-art, Desalination Journal, Volume 277, 2011, pp. 274-80.

[57] Cheboxarov V V, Yakimovich B A, Abd Ali L M, An Offshore Wind-Power-Based Water Desalination Complex as a Response to an Emergency in Water Supply to Northern Crimea, Journal of Applied Solar Energy, Volume 55, 2019, pp. 260–264.

[58] Serrano-Tovar T, Peñate Suárez B, Musicki A, de la Fuente Bencomo J A, Cabello V, Giampietro M, Structuring an integrated water-energy-food nexus assessment of a local wind energy desalination system for irrigation, Journal of Science of The Total Environment, Volume 689, 2019, pp. 945-957.

[59] Peng W, Maleki A, Rosen M A, Azarikhah P, Optimization of a hybrid system for solar-wind-based water desalination by reverse osmosis: Comparison of approaches, Desalination Journal, Volume 442, 2018, pp. 16-31.

[60] Koklas P A, Papathanassiou S A, Component sizing for an autonomous wind-driven desalination plant, Journal of Renewable Energy, Volume 31, 2006, pp. 2122–2139.

[61] Dorn J G, World Geothermal Power Generation Nearing Eruption, 2008.

[62] Sarbatly R, Chiam C K, Evaluation of geothermal energy in desalination by vacuum membrane distillation, Journal of Applied Energy, Volume 112, 2013, pp. 737–46.

[63] Colmenar-Santos A, Palomo-Torrejón E, Mur-Pérez F, Rosales-Asensio E, Thermal desalination potential with parabolic trough collectors and geothermal energy in the Spanish southeast, Journal of Applied Energy, Volume 262, 2020.

[64] Hoseinzadeh S, Yargholi R, Kariman H, Heyns P S, Exergoeconomic analysis and optimization of reverse osmosis desalination integrated with geothermal energy, Journal of environmental Progress & Sustainable Energy, Volume 39, 2020, pp. 1944-7442

[65] Mohammadi M H, Abbasi H R, Ghodrat M, Optimal design of a hybrid thermal- and membrane-based desalination unit based on renewable geothermal energy, Journal of Energy Conversion and Management, Volume 12, 2021.

[66] Ahmadi E, McLellan B, Mohammadi-Ivatloo B, Tezuka T, The Role of Renewable Energy Resources in Sustainability of Water Desalination as a Potential Fresh-Water Source: An Updated Review. Sustainability 2020, Volume 12.

[67] Richards B S, Capao D P, Schafer A I, Renewable energy powered membrane technology, 2. The effect of energy fluctuations on performance of a photovoltaic hybrid membrane system, Environmental science & technology, Volume 42, 2008, pp. 4563-4569.

[68] Gocht W, Sommerfeld A, Rautenbach R, Melin T, Eilers L, Neskakis A, Herold D, Horstmann V, Kabariti, Muhaidat A, Decentralized desalination of brackish water by a directly coupled reverse-osmosis-photovoltaic-system - a pilot plant study in Jordan, Renewable Energy, Volume 14, 1998, pp. 287-292.

[69] de la Nuez Pestana I, Javier García Latorre F, Argudo Espinoza C, Gómez Gotor A, Optimization of RO desalination systems powered by renewable energies. Part I: Wind energy, Desalination Journal, Volume 160, 2004, pp. 293-299.

[70] Thomson M, Infield D, Laboratory demonstration of a photovoltaic-powered seawater reverse-osmosis system without batteries, Desalination Journal, Volume 183, 2005, pp. 105-111.

[71] Thomson M, Infield D, A photovoltaic-powered seawater reverse-osmosis system without batteries, Desalination Journal, Volume 153, 2003, pp. 1-8.

[72] Bilton A M, Kelley L C, Dubowsky S, Photovoltaic reverse osmosis - Feasibility and a pathway to develop technology, Journal of Desalination and Water Treatment, Volume 31, 2011, pp. 24-34.

[73] Mascara Now Tech, Method For Controlling A Desalination Plant Fed By A Source Of Renewable Energy And Associated Plant, 2016, international patent WO2017002022A1, 2017.

[74] Saleem M W, Abbas A, Asim M, Uddin GM, Chaudhary T N, Ullah A, Design and cost estimation of solar-powered reverse osmosis desalination system, Journal of Advances in Mechanical Engineering, Volume 13, 2021.

[75] Boesch W, World's first solar-powered reverse osmosis desalination plant, Desalination Journal, Volume 41, 1982, pp. 233-237.

[76] Fiorenza G, Sharma V K, Braccio G, Techno-economic evaluation of a solar-powered water desalination plant, Journal of Energy Conversion and Management, Volume 44, Issue 14, 2003, pp. 2217-2240.

[77] Borge-Diez D, García-Moya F J, Cabrera-Santana P, Rosales-Asensio E, Feasibility analysis of wind and solar powered desalination plants: An application to islands, Journal of Science of The Total Environment, Volume 764, 2021.

[78] Voutchkov N, Desalination engineering: planning and design. McGraw Hill Professional, 2012.

[79] Al-Karaghouli A, Renne D, Kazmerski L L, Solar and wind opportunities for water desalination in the Arab regions, Journal of Renewable and Sustainable Energy Reviews, Volume 13, Issue 9, 2009, pp. 2397-2407.

[80] Ghermandi A, Messalem R, Solar-driven desalination with reverse osmosis the state of the art, Journal of Desalination and Water Treatment, Volume 7, 2009, pp. 285–296.

[81] Thomson M, Miranda M, Gwillim J, Rowbottom A, Draisey I, Batteryless photovoltaic reverse-osmosis desalination system, 2001.

[82] Forstmeier M, Feichter W, Mayer O, Photovoltaic powered water purification - challenges and opportunities, Desalination Journal, Volume 221, 2008, pp. 23-28.

[83] Elasaad H, Bilton A., Kelley L, Duayhe O, Dubowsky S, Field evaluation of a community scale solar powered water purification technology: a case study of a remote Mexican community application, Desalination Journal, Volume 375, 2015, pp. 71–80.

[84] Kumarasamy S, Narasimhan S, Narasimhan S, Optimal operation of battery-less solar powered reverse osmosis plant for desalination, Desalination Journal, Volume 375, 2015, pp. 89–99.

[85] Shivashankar S, Mekhilef S, Mokhlis H, Karimi M, Mitigating methods of power fluctuation of photovoltaic (PV) sources - A review, Renewable and Sustainable Energy Reviews, Volume 15, 2016, 1170-1184.

[86] Xie M, Tang C Y, Gray S R, Spacer-induced forward osmosis membrane integrity loss during gypsum scaling, Desalination Journal, Volume 392, 2016, pp. 85-90.

[87] http://www.vfds.com

[88] European Commission, "The future role and challenges of Energy Storage," Directorate-General for Energy working paper, 2013.

[89] Charles J P, Bordure G, Khoury A, Mialhe P, Consistency of the double exponential model with physical mechanisms of conduction for a solar cell under illumination, Applied Physics Journal, Volume 18, 1985.

[90] Ahmad T, Sobhan S, Nayan F, Comparative Analysis between Single Diode and Double Diode Model of PV Cell: Concentrate Different Parameters Effect on Its Efficiency, 2016.

[91] Ahmad M.J, Tiwari G N, Solar radiation models—A review, International Journal of Energy Research, Volume 35, 2011, pp. 271-290.

[92] Lonsdale H, Merten U, Riley R, Transport properties of cellulose acetate osmotic membranes, Journal of Applied Polymer Science, Volume 9, 1965, pp. 1341-1362.

[93] Merten U, Flow Relationships in Reverse Osmosis, Journal of Industrial & Engineering Chemistry Fundamentals, Volume 2, 1963, pp. 229-232.

[94] Robinson R A, Stokes R H, Electrolyte solutions, Courier Dover Publications, 2002.

[95] Mickols W, Substantial Changes in the Transport Model of Reverse Osmosis and Nanofiltration by Incorporating Accurate Activity Data of Electrolytes, Journal of Industrial & Engineering Chemistry Research, Volume 55, 2016, pp. 11139-11149.

[96] van't Hoff J H, Die Rolle des osmotischen Druckes in der Analogie zwischen Lösungen und Gasen, Zeitschrift für physikalische Chemie, Volume 1, 1887, pp. 481-508.

[97] Feher J, 2.7 - Osmosis and Osmotic Pressure, in: Quantitative Human Physiology, Academic Press, Boston, 2012, pp. 141-152.

[98] ASTM, D4516-85 Standard Practice for Standardizing Reverse Osmosis Performance Data.

[99] Marcel M, Basic principles of membrane technology Second ed., Kluwer Academic Publishers, 1996.

[100] Guidelines for drinking-water quality, ISBN: 978-92-4-154995-0, World Health Organization, 4th edition, 2017.

[101] Morton A J, Callister I K, Wade N M, Environmental impacts of seawater distillation and reverse osmosis processes, Desalination Journal, Volume 108, 1997, pp. 1-10,

[102] Zhou J, Chang V W C, Fane A G, An improved life cycle impact assessment (LCIA) approach for assessing aquatic eco-toxic impact of brine disposal from seawater desalination plants, Desalination Journal, Volume 308, 2013, pp. 233-241.

[103] Mezher T, Fath H, Abbas Z, Khaled A,Techno-economic assessment and environmental impacts of desalination technologies, Desalination Journal, Volume 266, 2011, pp. 263-273.

[104] Do Thi H T, Pasztor Tank, Fozer D, Manenti Feed, Toth A J, Comparison of Desalination Technologies Using Renewable Energy Sources with Life Cycle, PESTLE, and Multi-Criteria Decision Analyses, Water Journal, Volume 13, 2021, pp. 3023.

[105] Raluy G, Serra L, Uche J, Life cycle assessment of MSF, MED and RO desalination technologies, Energy Journal, Volume 31, 2006, pp. 2025–2036.

[106] Chen Z, Ngo H H, Guo W, A critical review on sustainability assessment of recycled water schemes, Science of the Total Environment Journal, Volume 426, 2012, pp. 13-31.

[107] Mannan M, Alhaj M, Mabrouk A N, Al-Ghamdi S G, Examining the life-cycle environmental impacts of desalination: A case study in the State of Qatar, Desalination Journal, Volume 452, 2019, pp. 238-246.

[108] Aziz N I H A, Hanafiah M M, Life cycle analysis of biogas production from anaerobic digestion of palm oil mill effluent, Renewable Energy Journal, Volume 145, 2020, pp. 847-857.

[109] ISO 14 044 (2006): Environmental management – Life cycle assessment – requirements and guidelines.

[110] Beery M, Repke J U, Sustainability analysis of different SWRO pre-treatment alternatives. Desalination and Water Treatment Journal, Volume 16, 2010, pp. 218-228.

[111] Guinee J B et al., Handbook on Life Cycle Assessment: Operational Guide to the ISO Standards, Springer Science, 2002.

[112] Munoz, I, Fernandez-Alba A R, Reducing the environmental impacts of reverse osmosis desalination by using brackish groundwater resources, Water Research Journal, Volume 42, 2008, pp. 801-811.

[113] Zhou J, Chang V W-C, Fane A G, Environmental life cycle assessment of brackish water reverse osmosis desalination for different electricity production models, Energy & Environmental Science, Volume 4, 2011, pp. 2267–2278.

[114] Tarnacki K, Meneses M, Melin T, Medevoort J V, Jansen A E, Environmental assessment of desalination processes: Reverse osmosis and Memstill®, Desalination Journal, Volume 296, 2012, pp. 69–80.

[115] Hancock N T, Black N D, Cath T Y, A comparative life cycle assessment of hybrid osmotic dilution desalination and established seawater desalination and wastewater reclamation processes, Water Research Journal, Volume 46, 2012, pp. 1145–1154.

[116] Stokes J R, Horvath A, Energy and air emission effects of water supply, Environmental Science & Technology Journal, Volume 43, 2009, pp. 2680–2687.

[117] Al-Sarkal T, Arafat H A, Ultrafiltration versus sedimentation-based pretreatment in Fujairah-1 RO plant: environmental impact study, Desalination Journal, Volume 317, 2013, pp. 55–66.

[118] Beery M, Repke J U, Sustainability analysis of different SWRO pre-treatment alternatives, Desalination and Water Treatment Journal, Volume 16, 2010, pp. 218–228.

[119] Amores, M J, Meneses M, Pasqualino J, Anton A, Castells F, Environmental assessment of urban water cycle on Mediterranean conditions by LCA approach, Journal of Cleaner Production, Volume 43, 2013, 84-92.

[120] Abuhabib A A, Ghasemi M, Mohammad A W, Rahman R A, El-Shafie A H, Desalination of brackish water using nanofiltration: performance comparison of different membranes, Arabian Journal for Science and Engineering, Volume 38, 2013, pp. 2929-2939.

[121] Rodman K E, Cervania A A, Budig-Markin V, Schermesser C F, Rogers O W, Martinez J M, King J, Hasset P, Burns J, Gonzales M S, Folkerts A, Duin P, Virgil A S, Aldrete M, Lagasca A, Infanzon-Marin A, Aitchison J R, White D, Boutros B C, Ortega S, Davis B, Tran V N, Achili A,. Coastal California wastewater effluent as a resource for seawater desalination brine commingling, Water Journal, Volume 10, 2018, pp. 322.

[122] Dreyer L C, Niemann A L, Hauschild M Z, Comparison of three different LCIA methods: EDIP97, CML2001 and Eco-indicator 99, International Journal of Life Cycle Assessment, Volume 8, 2003, pp. 191-200.

[123] Hauschild M Z, Huijbregts M A J, Life cycle impact assessment. In: Klopffer W, Curran M, LCA Compendium e the Complete World of Life Cycle Assessment, Springer, Dordrecht, 2015, p. 339 (Eds.).

[124] Luo L, Yang L L, Hanafiah M M, Construction of renewable energy supply chain model based on LCA, Journal of Open Physics, Volume 16, 2018, pp. 1118-1126.

[125] Kägi T, Dinkel F, Frischknecht R, Humbert S, Lindberg J, De Mester S, Ponsioen T, Sala S, X Schenker U W, Session "Midpoint, endpoint or single score for decision-making, International Journal of Life Cycle Assessment, SETAC Europe 25th Annual Meeting, 2015.

[126] Gabathuler H, The CML Story How Environmental Sciences Entered the Debate on LCA. International Journal of Life Cycle Assessment, Volume 4, 1997, pp. 187–194.

[127] Klinglmair M, Sala S, Brandão M. Assessing resource depletion in LCA: a review of methods and methodological issues, International Journal of Life Cycle Assess, Volume 19, 2014, pp. 580–592.

[128] Guinée J B, Gorrée M, Heijungs R, Huppes G, Kleijn R, De Koning A, Van Oers L, Wegener Sleeswijk A, Suh S, Udo de Haes H, de Bruijn G, Handbook on LCA, operational guide to the ISO standards, 2002.

[129] Hischier R, Weidema B, Althaus H J, Bauer C, Doka G, Dones R, Frischknecht R, Hellweg S, Humbert S, Jungbluth N, Implementation of Life Cycle Impact Assessment Methods; Swiss Centre for Life Cycle Inventories: St. Gallen, Switzerland, 2010.

[130] Benini L, Mancini L, Sala S, Manfredi S, Schau E, Pant R, Normalisation Method and Data for Environmental Footprints; Publications Office of the European Union: Luxembourg, 2014.

[131] Jiménez-González C, Kim S, Overcash M.R., Methodology for developing gate-to-gate Life cycle inventory information, The International Journal of Life Cycle Assessment, Volume 5, 2000, pp. 153–159.

[132] Ismail H, Hanafiah M M, A review of sustainable e-waste generation and management: present and future perspectives, Journal of Environmental Management, Volume 264, 2020.

[133] Martins A A, Caetano N S, Mata T M, LCA for Membrane Processes. In: Sustainable Membrane Technology for Water and Wastewater Treatment, Green Chemistry and Sustainable Technology, Springer, Singapore, 2017.

[134] Balioti V, Tzimopoulos C, Evangelides C, Multi-Criteria Decision Making Using TOPSIS Method Under Fuzzy Environment, Application in Spillway Selection, Proceedings 2018.

[135] Torcellini P, Deru M, Hofstetter P, Keoleian G, Sullivan J, Weitz K, U.S.LCI database project development guidelines, National Renewable Energy Laboratory, Colorado, U.S., 2004.

[136] Goga T, Friedrich E, Buckley C A, Environmental life cycle assessment for potable water production–a case study of seawater desalination and mine-water reclamation in South Africa. Water SA Journal, Volume 45, 2019, pp. 700–709.

[137] Raluy R G, Serra L, Uche J, Valero A, Life-cycle assessment of desalination technologies integrated with energy production systems, Desalination Journal, Volume 167, 2004, pp. 445-458.

[138] Meneses M, Pasqualino J C, C´espedes-Sanchez R, Castells F, Alternatives for reducing the environmental impact of the main residue from a desalination plant, Journal of Industrial Ecology, Volume 14, 2010, pp. 512–527.

[139] Li Y, Xiong W, Zhang W, Wang C, Wang P, Life cycle assessment of water supply alternatives in water-receiving areas of the South-to-North Water Diversion Project in China, water research Journal, Volume 89, 2016, pp. 9–19.

[140] Shahabi M P, McHugh A, Anda M, Ho G, Environmental life cycle assessment of seawater reverse osmosis desalination plant powered by renewable energy, Renewable Energy Journal, Volume 67, 2014, pp. 53–58.

[141] Palanov N, Life-cycle assessment of Photovoltaic systems - Analysis of environmental impact from the production of PV system including solar panels produced by Gaia Solar, 2014, Lund University.

[142] Oers L V, CML-IA database, characterisation and normalisation factors for midpoint impact category indicators, 2016.

[143] Oers L V, Koning A D, Guinee J B, Huppes G, Abiotic resource depletion in LCA, 2002, Road and Hydraulic Engineering Institute.

[144] Cusenza M A, Bobba S, Ardente F, Cellura M, X Di Persio F, Energy and environmental assessment of a traction lithium-ion battery pack for plug-in hybrid electric vehicles, Journal of Cleaner Production, Volume 215, 2019, pp. 634-649.

[145] Cherif H, Champenois G, Belhadj J, Environmental life cycle analysis of a water pumping and desalination process powered by intermittent renewable energy sources, Renewable and Sustainable Energy Reviews, Volume 59, 2016, pp. 1504–1513.

[146] Milne G, Embodied energy. Retrieved July 7, 2019, from http://www.yourhome.gov.au/materials/embodied-energy.

[147] Tan H, Pillai K M, Blast Protection of Civil Infrastructures and Vehicles Using Composites, Woodhead Publishing Series in Civil and Structural Engineering, 2010, pp. 54-87

[148] Acero A P, Rodríguez C, Ciroth A, Impact assessment methods in Life Cycle Assessment and their impact categories, 2016.

[149] Tang C Y, Kwon Y N, Leckie J O, Fouling of reverse osmosis and nanofiltration membranes by humic acid—Effects of solution composition and hydrodynamic conditions, Journal of Membrane Science, Volume 290, 2007, pp. 86-94.

[150] Jiang S, Li Y, Ladewig B P, A review of reverse osmosis membrane fouling and control strategies, Science of the Total Environment Journal, Volume 595, 2017, pp. 567-583.

[151] Schäfer A I, Broeckmann A, Richards B S, Renewable energy powered membrane technology. 1. Development and characterization of a photovoltaic hybrid membrane system, Journal of Environmental Science and Technology, Volume 41, 2007, pp. 998–1003.

[152] Richards B S, Capao D Pump S, Schäfer A I, Renewable energy powered membrane technology. 2. The effect of energy fluctuations on performance of a photovoltaic hybrid membrane system, Journal of Environmental Science and Technology, Volume 42, 2008, pp. 4563–4569.

[153] Freire-Gormaly M, Bilton A.M., Experimental quantification of the effect of intermittent operation on membrane performance of solar powered reverse osmosis desalination systems, Desalination Journal, Volume 435, 2018, pp. 188-197.

[154] Williams M E, Hestekin J A, Smothers C N, Bhattacharyya D, Separation of organic pollutants by reverse osmosis and nanofiltration membranes: Mathematical models and experimental verification, Industrial & Engineering Chemistry Research Journal, Volume 38 1999, pp. 3683-3695.

[155] K.W. Allen, "At forty cometh understanding" A review of some basics of adhesion over the past four decades, International Journal of Adhesion and Adhesives, Volume 23, 2003, pp. 87-93.

[156] Gloede M, Melin T, Physical aspects of membrane scaling, Desalination Journal, Volume 224, 2008, pp. 71- 75.

[157] Boerlage S F E, Kennedy M D, Witkamp G J, van der Hoek J P, Schippers J C, BaSO4 solubility prediction in reverse osmosis systems, Journal of Membrane Science, Volume 159, 1999, pp. 47- 59.

[158] Gabelich C J, Yun T I, Coffey B M, Suffet I H, Effects of aluminium sulfate and ferric chloride coagulant residuals on polyamide membrane performance, Desalination Journal, Volume 159, 2002, pp. 15-30.

[159] Dalvi A G, Al-Rasheed, R, Javeed, M A, Studies on organic foulants in the seawater feed of reverse osmosis plants of SWCC. Proceedings of the Conference on Membranes in Drinking and Industrial Water Production, Paris, France, 2000, pp. 459-474.

[160] Yu Y, Lee S, Hong S, Effect of solution chemistry on organic fouling of reverse osmosis membranes in seawater desalination, Journal of Membrane Science, Volume 351, 2010, pp. 205-213.

[161] Ang W S, Lee S, Elimelech M, Chemical and physical aspects of cleaning of organic fouled reverse osmosis membranes, Journal of Membrane Science, Volume 272, 2006., pp. 198-210.

[162] Gutierrez L, Aubry C, Valladares Linares R, Croue J-P, Natural organic matter interactions with polyamide and polysulfone membranes: Formation of conditioning film, Journal of Colloids and Surfaces A: Physicochemical and Engineering Aspects, Volume 477, 2015, pp. 1-8.

[163] Ivnitskya H, Katza I, Minzc D, Shimonid E, Chene Y, Tarchitzkye J, Semiatb R, Dosoretza C G, Characterization of membrane biofouling in nanofiltration processes of wastewater treatment, Desalination Journal, Volume 185, 2005, pp. 255–268.

[164] Li H, Xia H, Mei Y, Modelling organic fouling of reverse osmosis membrane: From adsorption to fouling layer formation, Desalination Journal, Volume 386, 2016, pp. 25-31.

[165] Herzberg M, Elimelech M, Biofouling of reverse osmosis membranes: Role of biofilm-enhanced osmotic pressure, Journal of Membrane Science, Volume 295, 2007, pp. 11–20.

[166] Hoek E M V, Elimelech M, Cake-enhanced concentration polarization: a new fouling mechanism for salt-rejecting membranes, Journal of Environmental Science and Technology, Volume 37, 2003, pp. 5581–5588.

[167] Park J, Jeong W, Nam J, Kim J, Kim J, Chon K, Lee E, Kim H, Jang A, An analysis of the effects of osmotic backwashing on the seawater reverse osmosis process, Journal of Environmental Technology, Volume 35, 2014, pp. 1455-1461.

[168] DIN EN 50530 VDE 0126-12, 2013,12 Overall efficiency of grid connected photovoltaic inverters, VDE Art. No.: 0100188.

[169] Yiantsios S G, Sioutopoulos D, Karabelas A J, Colloidal fouling of RO membranes: an overview of key issues and efforts to develop improved prediction techniques. Desalination Journal, Volume 183, 2005, pp. 257–272.

[170] Li Q, Elimelech M, Organic fouling and chemical cleaning of nanofiltration membranes: measurements and mechanisms. Journal of Environmental Science and Technology, Volume 38, 2004, pp. 4683-4693.

[171] Lee S, Ang W S, Elimelech M, Fouling of reverse osmosis membranes by hydrophilic organic matter: implications for water reuse, Desalination Journal, Volume 187,2006, pp. 313-321.

[172] Hong S, Elimelech M, Chemical and physical aspects of natural organic matter (NOM) fouling of nanofiltration membranes, Journal of Membrane Science, Volume 132, 1997, pp. 159-181.

[173] Amy G, Fundamental understanding of organic matter fouling of membranes, Desalination Journal, Volume 231, 2008, pp. 44-51.

[174] Ouatmane A, Hafidi M, EL Gharous M, Revel J C, Complexation of calcium ions by humic and fulvic acids, Analusis Journal, Volume 27, 1999, pp. 428-431.

[175] Liu Q, Xu G R, Das R, Inorganic scaling in reverse osmosis (RO) desalination: Mechanisms, monitoring, and inhibition strategies, Desalination Journal, Volume 468, 2019, pp. 114065.

[176] Cai Y H, Burkhardt C J, Schäfer A I, Renewable energy powered membrane technology: Impact of osmotic backwash on scaling during solar irradiance fluctuation, Journal of Membrane Science, Volume 619, 2021, pp. 118799.

[177] Tzotzi C, Pahiadaki T, Yiantsios S, Karabelas A, Andritsos N, A study of CaCO3 scale formation and inhibition in RO and NF membrane processes, Journal of Membrane Science, Volume 296, 2007, pp. 171-184.

[178] Ansari A, Peña-Bahamonde J, Fanourakis S K, Hu Y, Rodrigues D F, Microbially-induced mineral scaling in desalination conditions: Mechanisms and effects of commercial antiscalants, Water Research Journal, Volume 179, 2020.

[179] Chon K, Cho J, Fouling behavior of dissolved organic matter in nanofiltration membranes from a pilot-scale drinking water treatment plant: An autopsy study, Chemical Engineering Journal, Volume 295, 2016, pp. 268-277.

[180] A. Antony, G. Leslie, Degradation of polymeric membranes in water and wastewater treatment, in: A. Basile, S.P. Nunes, Advanced Membrane Science and Technology for Sustainable Energy and Environmental Applications, Woodhead Publishing, 2011, pp. 718-745.

[181] Assessing Microbial Safety of Drinking Water: Improving Approaches and Methods, Organisation for Economic Co-operation and Development (OECD) and World Health Organization (WHO), 2003.

[182] Komlenic R, Rethinking the causes of membrane biofouling, Filtration and Separation Journal, Volume 47, 2010, pp. 26-28.

[183] Creber S A, Vrouwenvelder J S, van Loosdrecht M C M , Johns M L , Chemical cleaning of biofouling in reverse osmosis membranes evaluated using magnetic resonance imaging, Journal of Membrane Science, Volume 362, 2010, pp. 202-210.

[184] Chang C W, Grinshpun S A, Willeke K, Macher J M, Donnelly J, Clark S, Juozaitis A, Factors Affecting Microbiological Colony Count Accuracy for Bioaerosol Sampling and Analysis, American Industrial Hygiene Association Journal, Volume 56, Issue 10, 1995, pp. 979-986.

[185] Tran T, Bolto B, Gray S, Hoang M, Ostarcevic E, An autopsy study of a fouled reverse osmosis membrane element used in a brackish water treatment plant, Journal of Water Research, Volume 41, Issue 17, 2007, pp. 3915-3923.

[186] Tay K G, Song L, A more effective method for fouling characterization in a full-scale reverse osmosis process. Journal of Desalination, 2005, Volume 177, pp. 95-107.

[187] Butt F H, Rahman F, Baduruthamal U, Characterization of foulants by autopsy of RO desalination membranes, Journal of Desalination, 1997, Volume 114, pp. 51-64.

[188] Gwona E M, Yu M J, Oh H K, Ylee Y H, Fouling characteristics of NF and RO operated for removal of dissolved matter from groundwater. Journal of Water Research, Volume 37, 2003, pp. 2989–2997.

[189] Yang H L, Huang C, Pan J R, Characteristics of RO foulants in a brackish water desalination plant, Desalination Journal, Volume 220, 2008, pp. 353-358.

[190] Lee S, Ang W S, Elimelech M, Fouling of reverse osmosis membranes by hydrophilic organic matter: implications for water reuse, Desalination Journal, Volume 187, 2006, pp. 313-321.

[191] Belfort G, Guter G A, An experimental study of electrodialysis hydrodynamics, Desalination journal, Volume 10, 1972, pp. 221-262.

[192] Gimmelshtein M, Semiat R, Investigation of flow next to membrane walls, Journal of Membrane Science, Volume 264, 2005, pp. 137–150.

[193] Antony A, Low J H, Gray S, Childress A E, Le-Clech P, Leslie G, Scale formation and control in high pressure membrane water treatment systems: A review, Journal of Membrane Science, Volume 383, 2011, pp. 1-16.

[194] Matin A, Rahman F, Shafi H Z, Zubair S M, Scaling of reverse osmosis membranes used in water desalination: Phenomena, impact, and control; future directions, Desalination Journal, Volume 455, 2019, pp. 135-157.

[195] Myat D T, Stewart M B, Mergen M, Zhao O, Orbell J D, Gray S, Experimental and computational investigations of the interactions between model organic compounds and subsequent membrane fouling, Water Research Journal, Volume 48, 2014, pp. 108-118.

[196] Gwona E M, Yu M J, Oh H K, Ylee Y H, Fouling characteristics of NF and RO operated for removal of dissolved matter from groundwater, Water Research Journal, 37, Volume 2003, pp. 2989–2997.

[197] Chen Y, Zhang T, Chai D, Ye H, Tang S, Wang P, Sun H, Ge B, Niu Q J, Enhancing the NaCl/Na2SO4 separation selectivity and chlorine resistance of nanofiltration membranes by incorporating novel designed starch nanoparticles, Journal of Applied Surface Science, Volume 604, 2022.

[198] Koros W J. Ma Y H, Shimidzu T, Terminology for membranes and membrane processes (IUPAC Recommendations 1996), Journal of Pure and Applied Chemistry, Volume 68, 1996, pp. 1479-1489.

[199] Li S, Cai Y H, Schäfer A I, Richards B S, Renewable energy powered membrane technology: A review of the reliability of photovoltaic-powered membrane system components for brackish water desalination, Applied Energy Journal, Volume 253, 2019, pp. 113524.

[200] Speth T F, Gusses A M, Summers R S, Evaluation of nanofiltration pre-treatments for flux loss control, Desalination Journal, Volume 130, 2000, pp. 31-44.

[201] Tong T, Wallace A F, Zhao S, Wang Z, Mineral scaling in membrane desalination: Mechanisms, mitigation strategies, and feasibility of scaling-resistant membranes, J Journal of Membrane Science, Volume 579, 2019, pp. 52-69.

[202] Zhu X, Elimelech M, Colloidal fouling of reverse osmosis membranes: Measurements and fouling mechanisms, Journal of Environmental Science & Technology, Volume 31, 1997, pp. 3654-3662.

[203] Herzberg M, Elimelech M, Biofouling of reverse osmosis membranes: Role of biofilmenhanced osmotic pressure, Journal of Membrane Science, Volume 295, 2007, pp. 11-20.

[204] Frenkel V S, Cohen Y, New techniques for real-time monitoring of reverse osmosis membrane integrity for virus removal, Journal of Water Practice and Technology, Volume 13, 2018, pp. 947-957.

[205] Torii S, Hashimoto T, Do A T, Furumai H, Katayama H, Impact of repeated pressurization on virus removal by reverse osmosis membranes for household water treatment, Journal of Environmental Science: Water Research & Technology, Volume 5, 2019, pp. 910-919.

[206] Wijmans H, Concentration polarization, Encyclopaedia of Separation Sciences, Academic Press, San Diego, 2000, pp. 1682.

[207] Sutzkover I, Hasson D, Semiat R, Simple technique for measuring the concentration polarization level in a reverse osmosis system, Desalination Journal, Volume 131, 2000, pp. 117-127.

[208] Mickols W, Substantial Changes in the Transport Model of Reverse Osmosis and Nanofiltration by Incorporating Accurate Activity Data of Electrolytes, Journal of Industrial & Engineering Chemistry Research, Volume 55, 2016, pp. 11139-11149.

[209] Hemond H F, Fechner E J, Chapter 1 - Basic Concepts, in: Chemical fate and transport in the environment (Third Edition), Academic Press, Boston, 2015, pp. 1-73.

[210] Radu A I, Vrouwenvelder J S, van Loosdrecht M C M, Picioreanu C, Modeling the effect of biofilm formation on reverse osmosis performance: Flux, feed channel pressure drop and solute passage, Journal of Membrane Science, Volume 365, 2010, pp. 1–15.

[211] Lin W, Zhang Y, Li D, Wang X, Huang X, Roles and performance enhancement of feed spacer in spiral wound membrane modules for water treatment: A 20-year review on research evolvement, Journal of Water Research, Volume 198, 2021.

[212] Oh H J, Choung Y K, Lee S, Choi J S, Hwang Tank M, Kim J H, Scale formation in reverse osmosis desalination model development, Desalination Journal, Volume 238, 2009.

[213] Hu Z, Antony A, Leslie G, Le-Clech P, Real-time monitoring of scale formation in reverse osmosis using electrical impedance spectroscopy, Journal of Membrane Science, Volume 453, 2014, pp. 320–327.

[214] Chen T, Neville A, Yuan M, Calcium carbonate scale formation - assessing the initial stages of precipitation and deposition, Journal of Petroleum Science and Engineering, Volume 46, 2005, pp. 185–194.

[215] Pramanik B K, Gao Y, Fan L, Roddick F A, Liu Z, Antiscaling effect of polyaspartic acid and its derivative for RO membranes used for saline wastewater and brackish water desalination, Desalination Journal, Volume 404, 2017, pp. 224–229.

[216] Wang H, Liu G, Huang J, Zhou Y, Yao Q, Ma S, Cao K, Liu Y, Wu W, Sun W, Hu Z, Performance of an environmentally friendly anti-scalant in CaSO4 scale inhibition, Journal of Desalination Water Treatment, Volume 53, 2015, pp. 8–14.

[217] Allen K W, Adhesion and adhesives – some fundamentals, Studies in Conservation Journal, Volume 29, 1984, pp. 5-12.

[218] Richards B S, Capão D P S, W G Früh, Schäfer A I, Renewable energy powered membrane technology: Impact of solar irradiance fluctuations on performance of a brackish water reverse osmosis system, Journal of Separation and Purification Technology, Volume 156, 2015, pp. 379-390.

[219] Freire-Gormaly M, Bilton A M, Impact of intermittent operation on reverse osmosis membrane fouling for brackish groundwater desalination systems, Journal of Membrane Science, Volume 583, 2019, pp. 220-230.

[220] A. Sagiv, R. Semiat, Modeling of backwash cleaning methods for RO membranes, Desalination Journal, Volume 261, 2010, pp. 338-346.

[221] Labban O, Goon G, Foo Z H, Zhao X, V J H L, Osmotically-induced cleaning of fouled reverse osmosis membranes in desalination, The International Desalination Association World Congress on Desalination and Water Reuse, 2019.

[222] Sagiv A, N. Avraham, Dosoretz C G, Semiat R, Osmotic backwash mechanism of reverse osmosis membranes, Journal of Membrane Science, Volume 322, 2008, pp. 225-233.

[223] Pervov A, Andrianov A, Rudakova G, Popov K, A comparative study of some novel "green" and traditional antiscalants efficiency for the reverse osmotic Black Sea water desalination, Journal of Desalination Water Treatment, Volume 73, 2017, pp. 11–21.

[224] Aleisa E, Al-Shayji K, Ecological–economic modelling to optimize a desalination policy: case study of an arid rentier state, Desalination Journal, Volume 430, 2018, pp. 64–73.

[225] Kim J E, Phuntsho S, Chekli L, Choi J Y, Shon H K, Environmental and economic assessment of hybrid FO-RO/NF system with selected inorganic draw solutes for the treatment of mine impaired water, Desalination Journal, Volume 429, 2018, pp. 96–104.

[226] Kim J E, Phuntsho S, Chekli L, Hong S, Ghaffour N, Leiknes T, Choi J Y, Shon H K, Environmental and economic impacts of fertilizer drawn forward osmosis and nanofiltration hybrid system, Desalination Journal, Volume 416, 2017, pp. 76-85.

[227] Holger S, Jan K, Petra Z, Andrea S, Jürgen-Friedrich H, The social footprint of hydrogen production—a Social Life Cycle Assessment (S-LCA) of alkaline water electrolysis, Energy Procedia Journal, Volume 105, 2017, pp. 3038–3044.

[228] Zamagni A, Life cycle sustainability assessment, International Journal of Life Cycle Assessment, Volume 17, 2012, pp. 373–376.

[229] Bellia H, Youcef R, Fatima M, A detailed modelling photovoltaic module using MATLAB". NRIAG Journal of Astronomy and Geophysics, Volume 3, 2014, 53-61.

[230] Hagl, R.; "Elektrische Antriebstechnik", Hanser, 2. Auflage, 2015.

List of Figures

160

List of tables